國立臺灣大學生命科學院生化科技學系

碩士論文

Department of Biochemical Science and Technology

College of Life Science

National Taiwan University

Master Thesis

以電子自旋共振光譜分析敘利亞倉鼠普立昂胜肽序列

108-144 類澱粉纖維之結構特性

Structural Analysis of the Amyloid Fibrils Formed of

Syrian Hamster Prion Peptide (108-144) by Using

Electron Spin Resonance Spectroscopy

林煜晟

Yu-Sheng Lin

指導教授：楊健志 博士、陳佩燁 博士

Advisor: Chien-Chih Yang, Ph.D., Rita Pei-Yeh Chen, Ph.D.

中華民國 107 年 8 月

August, 2018

國立臺灣大學碩士學位論文
口試委員會審定書

以電子自旋共振光譜分析敘利亞倉鼠普立昂胜肽序列
108-144 類澱粉纖維之結構特性
Structural Analysis of the Amyloid Fibrils Formed of
Syrian Hamster Prion Peptide (108-144) by Using Electron
Spin Resonance Spectroscopy

本論文係 林煜晟君（學號 R05B22061）在國立臺灣大學生化科技學系完成之碩士學位論文，於民國 107 年 08 月 03 日承下列考試委員審查通過及口試及格，特此證明。

口試委員：

楊健志　　　陳佩燁（簽名）

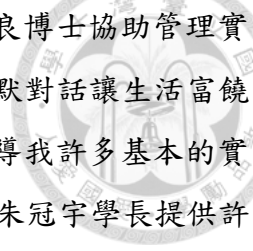（指導教授）

江明澈　　　陳振中

系主任、所長　　　王愛玉　　　（簽名）

謝辭

　　碩一剛搬入學術活動中心宿舍的那個晚上，我凝視著窗外稀疏而斑駁的燈光點綴著南港的靜謐夜色，心中感念這宛若新生的時刻。在這學術的搖籃，我暗自許下願望，期望在一年的軍旅生涯結束後，能在自己選擇的航道上繼續前行。

　　選擇，一直都不是件容易的事情，而我也曾經是因表現不佳而被淘汰的一員。大學因陷入語言學、中英翻譯與生化本科之間的生涯抉擇而疏於系上專題研究，過少的研究成果加上歷年成績不佳，導致入學口試與尋找指導教授時皆遭遇不少困難，也曾幾度讓我灰心與自我懷疑，不斷質疑自己是否該另尋出路。一路的顛簸與晦暗，直到與系上的楊健志老師晤談以及遇見陳佩燁老師後，才開始褪去。

　　首先非常感謝兩位老師一開始並沒有放棄我，還記得第一次來中研院與陳老師面談，老師優雅地拿著英式風格的咖啡杯，談及自己的研究主題的時候眼中閃著熱情的光芒，讓我體會到熱忱這件事對於科學研究的重要性，也開啟了我進入結構生物學領域的奇幻旅程。研究過程絕非一帆風順，舉凡胜肽合成、自旋標記、類澱粉纖維生成乃至電子自旋光譜，都曾有遭遇困惑與瓶頸的時刻，真的非常感謝老師細心引導我們解析問題、給我們思考方向，讓我們逐漸養成能自己獨立進行實驗與 troubleshooting 的能力，這種能力無論日後是繼續從事學術工作或進入職場就業，都是終身受用的重要技能。除此之外，也很感謝老師給予實驗室與研究生生活極大的自由度，讓我們能在融洽且不過度緊張的實驗室氣氛下學習與工作，且能自行規劃實驗進度與運用其他時間，不致在規律平淡的研究生活中感到疲乏。我也由衷感謝楊老師願意引薦我至中研院生化所完成我的碩士研究，雖然平時除了修課並不常出現在校總區，但在每一次能與老師請教問題的機會中，老師均悉心指導，也時常關心我的研究進度，在口頭報告的技巧與準備上更給了我許多啟發，讓我能順利完成碩士生涯中兩次 Master Day 的論文進度報告。另外我也非常感謝楊健志老師、台大化學系陳振中老師與清大化學系江昀緯老師於百忙中抽空前來擔任我的口試委員，提供許多不同面向的建議與指導，除了讓我獲益良多，也讓本論文更臻完善與嚴謹，僅在此由衷感謝。

　　實驗室的研究與庶務能順利運作，合作無間的同仁夥伴絕對是不可或缺的。感謝 504 實驗室的學長姐一路辛苦經營且傳承的實驗室傳統，讓實驗室成員間形

i

同手足，共同為學術研究和人生努力奮鬥；感謝實驗室的陳信良博士協助管理實驗室大小事與幫我們解決實驗上各種疑難雜症，還有日常的幽默對話讓生活富饒趣味；感謝陳詠翰博士在我剛進實驗室時細心地帶我入門，教導我許多基本的實驗流程與研究主題背景，也解答我各種關於 ESR 的問題；感謝朱冠宇學長提供許多研究上的心得分享與化學儀器方面的背景知識，讓我對整個研究主題的輪廓更加清楚；也感謝在日本東京攻讀博士班的沈志豪學長對我們學弟妹的照顧，除了提供許多實驗上的實用建議，也樂於與我們分享博班生活中的所見所聞。

在兩年的碩士生涯中，我非常幸運能遇見兩位能力非常好且努力不懈的同學雅涵與韻婷，她們對於實驗工作的細心與責任感每每砥礪我更加認真努力，一起在假日工作培養出的革命情感至今難忘；感謝去年畢業的渝絜學姊在我碩一時給予我各種實驗上的幫助，讓我的實驗能更快上軌。感謝實驗室助理明親、學弟至璿、庭軒、奕辰、俊廷和頌邦時常在生活中提供各式各樣的協助，彼此間也樂於分享生活中的酸甜苦辣，讓生活增添不少樂趣與風味；感謝最後幾個月回歸 504團隊的張晏溥學長，讓實驗室的研究戰力更加堅強。

在此我也要感謝我大學時期系上的啟蒙老師：廖憶純老師、黃楓婷老師與王愛玉老師，分別擔任我的導師、專題研究與專題討論的指導老師，為我今日的研究成果打下穩固的學術基礎。此外也感謝我大學時期的同窗好友，雖然大部分已在職場就業，仍願意持續給我鼓勵與支持。另外我也要感謝我在實驗室以外人聲樂團的夥伴們，讓我在研究工作之外能為阿卡貝拉音樂貢獻一己之聲，在時間的縫隙中把握機會練團、表演和出國比賽，一路走來誠惶誠恐卻彌足珍貴。當然最大的感謝要獻給父母，除了養育之恩與提供不虞匱乏的經濟支柱，更重要的是培養了我良好的語文能力與科學涵養，並教給我正確且積極的人生價值觀。最後，感謝台灣這片土地提供許多資源，讓我能茁壯成熟；感謝科學，讓我們有機會藉由雙手，一窺大自然與人體各種複雜機轉背後的奧秘。

春去秋來，兩年光陰轉眼匆匆已過，如今即將前往瑞典交換將近一年，除了準備在寒冷的北國展開新生活，也必須繼續思索人生的新方向。不管下一步選擇在何方落腳，期望自己都能繼續懷抱熱忱，為這個世界貢獻一己之力。

二零一八年八月　於 臺北南港

中文摘要

　　普立昂蛋白原是位於神經細胞外膜上的醣蛋白，正常形態 (PrP^C) 的結構以 α-螺旋為主，當結構上轉變為 β 結構為主之致病形態 (PrP^{Sc}) 時，會不正常聚集而堆疊為類澱粉纖維，此種形式的普立昂蛋白會造成腦細胞死亡，產生海綿樣組織空洞，最後導致死亡。目前仍不清楚普立昂蛋白進行結構轉變時，究竟是結構中的哪一段形成分子間 β 結構，本論文即探討普立昂胜肽形成的類澱粉纖維之堆疊特性及與其胺基酸序列的關係。

　　本論文使用敘利亞倉鼠之胜肽片段（序列108-144）為實驗材料，選取七個疏水性、非極性之胺基酸為接上自旋標記的位置，於胜肽合成時以半胱胺酸替代。以高效液相層析儀純化胜肽後，在半胱胺酸支鍵接上具有自由基電子的甲烷硫磺酸基團 MTSSL 自旋標記，再利用野生型普立昂胜肽形成的類澱粉纖維為晶種，誘發帶有自旋標記的胜肽形成類澱粉纖維，最後利用電子自旋共振技術解析各標記位點之間的訊號強度推斷出相對距離，來探討普立昂胜肽形成類澱粉纖維後之結構特性。另外本論文也利用穿透式電子顯微鏡技術檢視普立昂胜肽形成之類澱粉纖維，以確認類澱粉纖維是否成功生成。

　　電子自旋共振的結果顯示，具有不同替代位點的胜肽之間其結構差異非常明顯。在自發性生長的類澱粉纖維之光譜中，其代表電子間訊號強度之線寬大致可排序為：A118R1 ≈ V121R1 > M134R1 ≈ L125R1 > A113R1 > M129R1 ≈ M138R1；而在晶種誘發生長組別的光譜中，除位點 M129R1 外，其曲線形狀均較為寬胖。以此結果我們推斷，在胜肽片段 108-144 中，可能存在兩個結構較為緊密的澱粉樣核心區，分別位於 A113 與 L125 以及 M134 與 M138 之間。在兩個澱粉樣核心區之間，縱然 M129 周圍區域的結構較為鬆散，卻可能對整體澱粉樣纖維結構產生決定性的影響。從倉鼠普立昂胜肽的實驗出發，我們希望可以解開普立昂蛋白結構上的堆疊關鍵區域，再進一步推展到人類普立昂蛋白上，以便作為未來疾病治療、預防與藥物開發之依據。

關鍵字：普立昂疾病、澱粉樣纖維、倉鼠普立昂胜肽、澱粉樣核心區、位點取向自旋標記、電子自旋共振光譜

Abstract
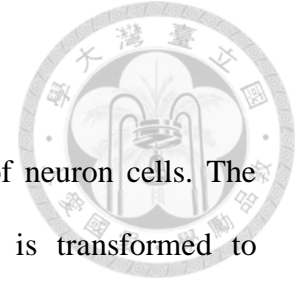
Prion protein is a glycoprotein anchored on the membrane of neuron cells. The normal, cellular form (PrP^C) is rich in α-helices. When PrP^C is transformed to disease-causing form (PrP^{Sc}), β structures appear to dominate in prion protein. PrP^{Sc} is prone to association, leading to the formation of amyloid fibrils. This aggregation form of prion protein can induce neuronal death in the brain, which results in sponge-like holes, and finally lead to fatal consequence.

Little is known about the core regions where the structural conversion takes place and form intermolecular β structure (also known as cross-β structure). Our study aims to provide an insight in the structural features of the prion amyloid fibrils and the relationship with its amino acid sequence. Prion peptide (residue 108-144) from Syrian hamster is used as our target in this study. Seven hydrophobic, non-polar amino acid residues were picked out for substitution to cysteine in each mutant peptide respectively, serving as the spin labeling sites. The wild-type and mutant peptides were synthesized by solid-phase peptide synthesis and purified by HPLC. The mutant peptides were then labeled with MTSSL, featuring its methane thiosulfonate group and radical spin, on the side chain of cysteine residues (site-directed spin labeling). The spin-labeled peptide monomers were induced to form amyloid fibrils with or without adding seeds, which were prepared from the wild-type amyloid fibrils. The spin-labeled amyloid fibrils were further analyzed by electron spin resonance (ESR) spectroscopy for obtaining the information of relative proximity between spins. The morphologies of the amyloid fibrils were also examined by TEM to confirm the presence of fibrils.

Our ESR results revealed distinct features between peptides of different mutated sites. In the spectrograms of spontaneously formed fibrils, the linewidths could be

ranked as A118R1 ≈ V121R1 > M134R1 ≈ L125R1 > A113R1 > M129R1 ≈ M138R1, and the curves of seeded fibrils were all relatively broadened except for M129R1. It is assumed that there might be two amyloid cores within the peptide 108-144, ranging from A113 to L125 and from M134 to M138 respectively. Between these two cores the residues around M129 stood out as a key region, which might be loose in structure but packed between the two cores. Our study can provide useful information to explain the location of the amyloid core in the process of prion protein propagation, and we hope to develop drugs against prion disease progression.

Abbreviations

ACN	Acetonitrile
AD	Alzheimer's disease
BSE	Bovine spongiform encephalopathy
CD	Circular dichroism
CJD	Creutzfeldt-Jakob disease
CWD	Chronic wasting disease
cw-ESR	Continuous-wave electron spin resonance
DCM	Dichloromethane
DMF	N,N-Dimethylformamide
DMSO	Dimethyl sulfoxide
EDT	1,2-ethanedithiol
fCJD	Familial CJD
FFI	Fatal familial insomnia
Fmoc	9-Fluorenylmethoxycarbonyl
FT-IR	Fourier transform infrared spectroscopy
FSE	Feline spongiform encephalopathy
GdnHCl	Guanidine hydrochloride
GSS	Gerstmann-Sträussler-Scheinker syndrome
HaPrP	Hamster prion protein
HBTU	O-(Benzotriazol-1-yl)-N,N,N',N'-tetramethyluronium hexafluorophosphate hexafluorophosphate
HOAc	Acetic acid

HPLC	High performance liquid chromatography
iCJD	Iatrogenic CJD
MALDI-TOF	Matrix-assisted laser desorption ionization-time of flight
MOPS	3-morpholinopropane -1-sulfonic acid
MS	Mass spectrometry
MTBE	Methyl tert-butyl ether
MTSSL	S-(1-oxyl-2,2,5,5-tetramethyl-2,5-dihydro-1H-pyrrol-3-yl)methyl methanesulfonothioate
NMM	N-methylmorpholine
PrP	Prion protein
PrP^C	Cellular isoform prion protein
PrP^{Sc}	Disease-causing isoform of prion protein
sCJD	Sporadic CJD
SDSL	Site-directed spin-labeling
TEM	Transmission electron microscopy
TFA	Trifluoroacetic acid
ThT	Thioflavin T
TIS	Triisopropylsilane
TSE	Transmissible spongiform encephalopathy
UV-Vis	Ultraviolet-Visible
vCJD	Variant Creutzfeldt-Jakob disease
A (Ala)	Alanine
C (Cys)	Cysteine

D (Asp)	Aspartic acid
E (Glu)	Glutamic acid
F (Phe)	Phenylalanine
G (Gly)	Glycine
H (His)	Histidine
I (Ile)	Isoleucine
K (Lys)	Lysine
L (Leu)	Leucine
M (Met)	Methionine
N (Asn)	Asparagine
P (Pro)	Proline
Q (Gln)	Glutamine
R (Arg)	Arginine
S (Ser)	Serine
T (Thr)	Threonine
V (Val)	Valine
W (Trp)	Tryptophan
Y (Tyr)	Tyrosine

Table of Contents

List of Figures

Chapter 4

Chapter 5

Chapter 6

Appendixes

List of Tables

Chapter 1　Introduction

1.1　Introduction to prion disease

Prion disease is usually known as transmissible spongiform encephalopathy (TSE), which is a collection of fatal neurodegenerative diseases that can be discovered in human and other kinds of mammalians. Some of the examples in human include kuru, Gerstmann-Sträussler-Scheinker syndrome (GSS), fatal familial insomnia (FFI), and Creutzfeldt-Jakob disease (CJD), which was defined under different circumstances. Other examples of TSEs in other mammalians include bovine spongiform encephalopathy (BSE) in cattle, scrapie in sheep and goats, chronic wasting disease (CWD) in deer and elk, and feline spongiform encephalopathy (FSE) in cats. Diseases found in other hosts can be seen in Table 1.1 (Prusiner 1998, Eichner and Radford 2011).

TSEs in human have now been defined by various neuropathological symptoms, including astrogliosis, neuronal loss, and amyloid deposition. In addition, the spongiform degeneration of neurons is highly specific to prion diseases and typically allows for a definitive diagnosis (Aguzzi, Sigurdson et al. 2008). In clinical symptoms, patients often develop progressive dementia, leading to memory loss and personality changes, and are often accompanied by involuntary movements. Ultimately, this would lead to death in an average of months to years after the symptoms came out (Collinge 2001).

Among all of the TSEs, scrapie was the earliest to be found since 1732 in Europe. The name of this disease comes from one of the most notable clinical signs that affected animals will scrape off their fleeces against rough surfaces like trees or rocks because of

1
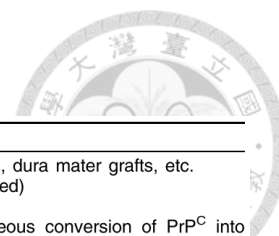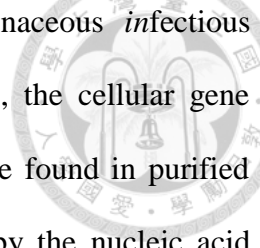
Table 1.1 Prion diseases.

Disease	Host	Mechanism of pathogenesis
iCJD	humans	infection from priorn-contaminated hGH, dura mater grafts, etc.
nvCJD	humans	infection from BSE prions (hyphothesized)
fCJD	humans	germ-line mutations in *PRNP* gene
sCJD	humans	somatic mutation resulting in spontaneous conversion of PrP^C into PrP^{Sc}?
Kuru	fore people	infection through ritualistic cannibalism
GSS	humans	germ-line mutations in *PRNP* gene
FFI	humans	germ-line mutations in *PRNP* gene
FSI	humans	somatic mutation resulting in spontaneous conversion of PrP^C into PrP^{Sc}?
Scrapie	sheep	infection in genetically susceptible sheep
BSE	cattle	infection with prion-contaminated MBM
TME	mink	infection with prions from sheep or cattle
CWD	mule, deer, elk	Unknown
FSE	cats	infection with prion-contaminated bovine tissues or MBM
Exotic ungulate encephalopathy	greater kudu, nyala, oryx	infection with prion-contaminated MBM

iCJD, iatrogenic CJD; nvCJD, new variant CJD; fCJD, familial CJD; sCJD, sporadic CJD; GSS, Gerstmann-Sträussler-Scheinker disease; FFI, fatal familial insomnia; FSI, fatal sporadic insomnia; BSE, bovine spongiform encephalopathy ('mad cow disease'); TME, transmissible mink encephalopathy; CWD, chronic wasting disease; FSE, feline spongiform encephalopathy; hGH, human growth hormone; MBM, meat and bone meal

the itching sensation caused by the disease. The cause of scrapie was in debate for years that the agent is very difficult to destroy with usual sterilizing methods like heat, radiation and disinfectants (Alper, Cramp et al. 1967). In addition, it does not induce any common immune response, has an average incubation period ranging from 18 months to 5 years, and has been known for not being transmissible to humans. Possibilities of bacteria had been excluded and the agent was thought to be a kind of unconventional virus. At the same time, it was proposed that the agent was kind of a "self-replicating" protein, which led to the generation of "protein-only hypothesis", which illustrated that prion diseases resulted from the conformational change between two alternative states of prion protein without any presence of nucleic acid (Griffith 1967, Laurent 1996).
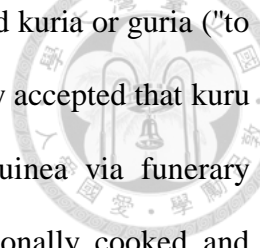
In 1982, the group of Prusiner had purified the agent from scrapie-infected hamster brain that was not found in similar fractions of the same uninfected brain. This protein had an apparent molecular size of 27-30 kDa in SDS-PAGE, and it was resistant to digestion by proteinase K, which distinguished it from other proteins of similar molecular weight found in the same brain homogenate. It was the time when this agent

2

was given the name "prion" protein, abbreviating from *pro*teinaceous *in*fectious particles (Bolton, McKinley et al. 1982, Prusiner 1982). In 1985, the cellular gene encoding PrP[27-30] was found, and no PrP-related nucleic acids were found in purified samples of scrapie prions, implying that PrP[27-30] is not encoded by the nucleic acid carried within the infectious agent (Oesch, Westaway et al. 1985).

Human prion diseases can be sporadic, inherited, or acquired by infection. Sporadic disease is the most common human prion disease which stands for around 85% of all cases; 10-15% are associated with mutations of *PRNP* gene and 1% are iatrogenic (Mackenzie and Will 2017). Sporadic diseases can be subdivided into several phenotypes including sporadic Creutzfeldt-Jakob disease (sCJD), fatal insomnia, and variably protease-sensitive prionopathy (variant CJD, vCJD) by distinct clinical and pathological characteristics. The disease was first described by German neurologist Hans Gerhard Creutzfeldt in 1921 and shortly afterward by Alfons Maria Jakob, giving it the name Creutzfeldt-Jakob. The patients of sCJD stands for more than 90% of all cases of sporadic prion disease and it is commonly categorized into five subtypes based on clinical symptoms like dementia and ataxia, histological features like spongiform tissues, and molecular traits this diseases including 14-3-3, tau, and the prion protein in the cerebral spinal fluid (CSF). Inherited type of prion diseases had been known to result from the gene mutation on the gene *prnp*, which would lead to Sträussler-Scheinker syndrome (GSS) and familial CJD (fCJD) (Puoti, Bizzi et al. 2012).

Prion diseases acquired by infection include kuru, iatrogenic CJD (iCJD), and variant CJD (vCJD). kuru was formerly common among the people of Papua New Guinea caused by the transmission of prion proteins, which led to symptoms such as

3

tremors and neurodegeneration. The term kuru derives from the word kuria or guria ("to shake") due to the classic symptom of body tremors. It is now widely accepted that kuru was transmitted among members of the tribe of Papua New Guinea via funerary cannibalism, which means deceased family members were traditionally cooked and eaten to help free the spirit of the dead. Among the victims of kuru, women and children were the majority since they usually consumed the brain and the organ in which infectious prions were most accumulated, thus allowing for transmission of kuru. This kind of diseases was also found to be able to transmit to chimpanzees from human (Gajdusek, Gibbs jun et al. 1966). The epidemic declined sharply after cannibalism was forbidden and discarded, with the last known kuru victim passing away in 2005 or 2009.
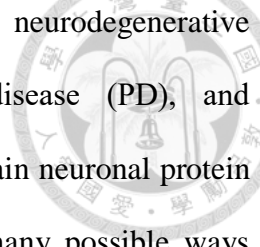
Iatrogenic CJD often arose from transmission of prion particles through neuronal surgical procedures, including contaminated equipment or growth hormone that was injected into patients. Variant CJD mainly refers to the prion disease that was first described in 1996 in the United Kingdom, which is now strongly supported that the agent responsible for the outbreak of vCJD in humans is the same agent that contributed to the outbreak of prion disease in cows, often designated bovine spongiform encephalopathy (BSE, or 'mad cow' disease). The transmission between cattle resulted from the production of fodder that was used to feed the cattle, in which the producer of fodder mixed the tissue and bone fragments of infected dead cow with other ingredients. Most of the BSEs in human then arose from chronic digestion of infected bovine neuronal tissues, while others might be infected through blood transfusion by receiving blood from potential patients that had not been found clinical symptoms yet. Several important differences had been distinguished between the vCJD and the classic CJD. On one hand, the median age at death of patients with classic CJD falls in range of 60 to 70

4

years, and very few cases occur in persons under 30 years of age. In contrast, the same statistics with vCJD in the UK is 28 years. On the other hand, in contrast to classic CJD, patients of vCJD in the UK predominantly have atypical clinical features including ataxia, dementia, myoclonus, and abnormal non-diagnostic electroencephalogram in duration of at least 6 months, which is much longer than classic CJD. The disease reached its epidemic peak in around 1992 in the UK, and later 2002 in places other than the UK, with over 30,000 cases were diagnosed as vCJD. After most of the suspected infected cattle were culled since the policy of the UK in 1996, the number of diagnosed case was decreased gradually by year. In the statistics from 2012, about 170 cases of vCJD have been recorded in the UK and other 50 cases in the rest of the world (Ironside 2012). Statistics updated to 2017 are shown in Figure 1.1, with very few cases left (Mackenzie and Will 2017).
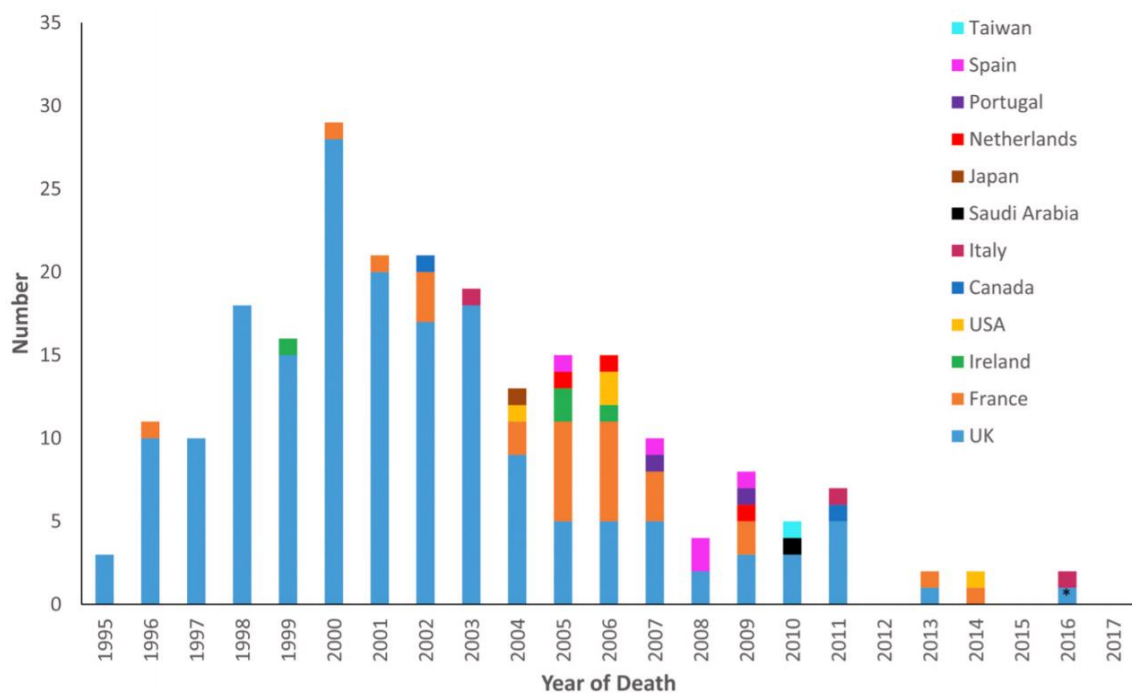
Figure 1.1 Variant Creutzfeldt-Jakob disease cases by year and country.
The polymorphism at codon 129 of the *PRNP* gene is MV, representing methionine/ valine heterozygous (Mackenzie and Will 2017).
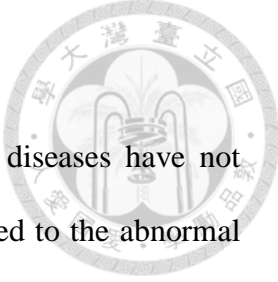
5

Although prion diseases share many similarities with other neurodegenerative disorders, such as Alzheimer's disease (AD), Parkinson's disease (PD), and Huntington's disease (HD), all of which involved generation of certain neuronal protein aggregates. Prion diseases were found to be infectious through many possible ways including sporadic and iatrogenic (Aguzzi and Polymenidou 2004). No effective therapies are available yet nowadays, but techniques of neuroimaging such as electroencephalography (EEG) and other novel biomarkers had helped for early diagnosis of prion diseases.

Recently, there had been study showing that autopsy or biopsy skin samples from patients of either sCJD or vCJD might have seeding activity after a series of amplifying procedures called real-time quaking-induced conversion (RT-QuIC) for PrP^{Sc} *in vitro*. Prion infectivity was also examined within humanized transgenic mice, and all mice inoculated with sCJD skin homogenates from sCJD patients succumbed to prion disease within 600 days after inoculation. Though the study demonstrated that the PrP^{Sc} from the skin of sCJD patients might contain both seeding activity and infectivity, which raised concerns about the possibility for iatrogenic sCJD transmission via skin, this kind of transmission was based on selective conditions such as purposeful amplification of PrP^{Sc} and inoculation into the brain tissues of animals, which would not be usual in the daily lives of the public (Orrú, Yuan et al. 2017).

6

1.2 The structure of prion protein

Though until nowadays the pathological mechanism of prion diseases have not been fully understood, it had been proved that the diseases are related to the abnormal structural conversion from cellular form PrP^C to scrapie form PrP^{Sc}, thus bringing this protein pathogenesis (Prusiner 1991). The human prion protein (huPrP) includes 208 amino acids after being cleaved and is added a glycosyl phosphoinositol (GPI) anchor. In normal condition, the protein is extracellular and attached at the outer membrane of a cell by means of the GPI anchor. It also contains two N-linked glycosylation sites at residues Asn181 and Asn197 (Rudd, Endo et al. 1999, Rudd, Wormald et al. 2001). The prion protein is highly conservative among mammals in their sequences, with 94.9% between human and sheep and 92.8% with cow (Wopfner, Weidenhöfer et al. 1999).
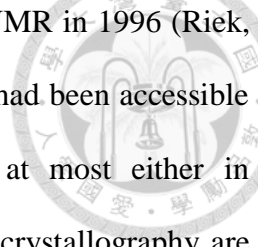
In normal conditions, the prion protein exists in the cellular form (PrP^C), which is mostly divided into two regions for further studies. The N-terminus, in mammals, includes different numbers of octapeptide PHGGSWGQ repeats, which is able to bind divalent metals such as copper (Millhauser 2007). Moreover, the N-terminal part up to residue 120 is found flexibly disordered at pH 4.5 (Donne, Viles et al. 1997), which may add to the difficulties of its structure determination. The C-terminus of PrP has been structured and exhibits a globular fold of three α-helices (H1, H2 and H3) and a short, double-stranded, antiparallel β-sheet (S1, S2) (Wuthrich and Riek 2001). A disulfide bridge links H2 and H3 between Cys179 and Cys214 (Figure 1.2).

7

(A)

(B)

(C)
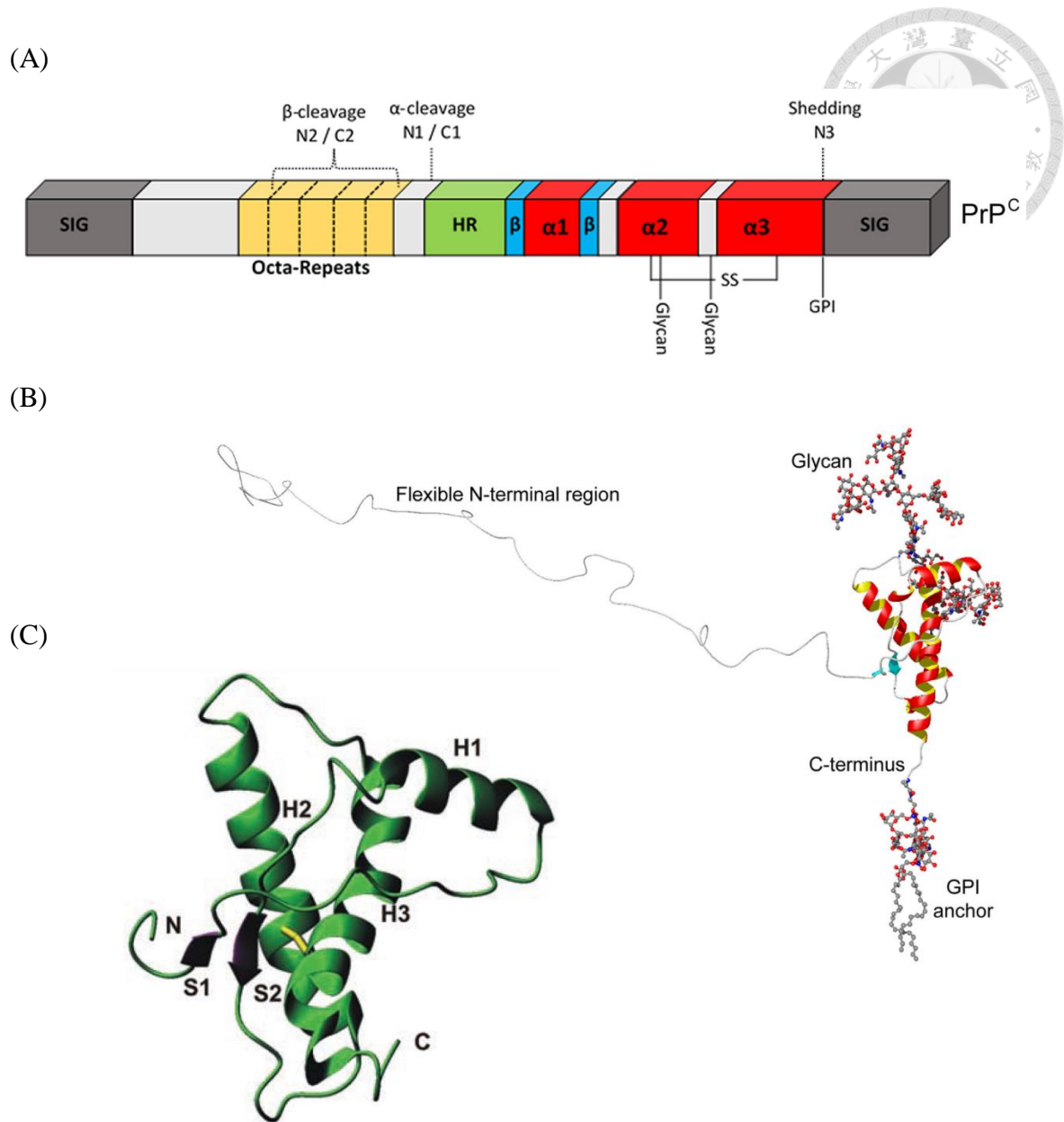
Figure 1.2 Schematic representation of PrP^C structure.

(A) Overall domain distribution of PrP^C. PrP^C possesses octa-peptide repeats in the N-terminal region, and three regions of α-helices and two regions of β-strands. SIG: N- and C-terminal signal peptides; HR: hydrophobic region (Castle and Gill 2017).

(B) Ribbon diagram of the PrP^C molecule. Three α-helices were shown in red and yellow and two β-strands shown in turquoise in the C-terminal domain. The N-terminal domain has been added a random configuration exhibiting flexible structure (Castle and Gill 2017).

(C) Ribbon representation of the C-terminal domain of mouse PrP. The disulfide bridge is labeled in yellow. This structure was graphed based on the previous NMR results (PDB ID number: 1B10) (Riek, Hornemann et al. 1996, Pastore and Zagari 2007).

8

The structure of C-terminal domain of PrP was first solved by NMR in 1996 (Riek, Hornemann et al. 1996), and since then more and more PrP entries had been accessible in the PDB database. NMR were used for structure solution at most either in determining the full-length or truncated forms of PrP, while X-ray crystallography are often restricted for use, only available in the C-terminal domains of the human and sheep PrP proteins, with the residues 119-226 for human and 119-231 for sheep (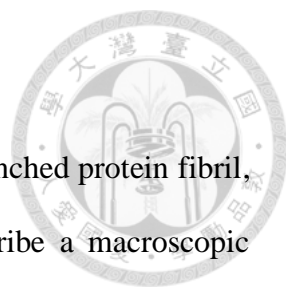Knaus, Morillas et al. 2001, Haire, Whyte et al. 2004). Part of the reason to this restriction is the intrinsic heterogeneity and local flexibility of PrP, leading to its intrinsic tendency to escape from proper crystallization. One of the important features found in the crystallization of human PrP was the occurrence of a covalent homo-dimer from domain swapping, suggesting a possible model for oligomerization in PrP propagation and amyloid generation (Knaus, Morillas et al. 2001). Furthermore, Fourier-transform infrared (FT-IR) spectroscopy had demonstrated that PrP^{C} has a high alpha-helix and little beta-sheet content, which were also confirmed by circular dichroism spectroscopy (Pan, Baldwin et al. 1993).

Distinct from the soluble nature of PrP^{C}, the disease-causing form of prion protein (PrP^{Sc}) is famous for its partially protease resistant and infectious properties. Even till nowadays, little has been known about the PrP^{Sc} structure due to its noncrystalline nature and its insolubility. The cleavage of its N-terminal 23-89 fragment has been documented and can generate a resistant core weighing around 27-30 kDa, termed PrP27-30 (Turk, Teplow et al. 1988). This fragment retains infectivity and can further polymerize to produce fibers (McKinley and Prusiner 1986). Alternative approaches such as FTIR spectroscopy has indicated that PrP^{Sc} and PrP27-30 include a higher amount of β-structure and a lower α-helical content (Kneipp, Miller et al. 2003).

Further information from either the PrP^C or PrP^{Sc} structure could be derived from solid-state NMR studies (Tycko, Savtchenko et al. 2010, Groveman, Dolan et al. 2014, Theint, Nadaud et al. 2017), hydrogen/deuterium exchange mass spectrometry (Lu, Wintrode et al. 2007), hydrogen exchange NMR spectroscopy (Kuwata, Matumoto et al. 2003, Damo, Phillips et al. 2010) and electron cryomicroscopy (cryo-EM) (Vázquez-Fernández, Vos et al. 2016). In particular, the structure of huPrP23-144 had been examined in detail by isotope labeling (Helmus, Surewicz et al. 2008, Helmus, Surewicz et al. 2010). So far, no high-resolution structure of a mammalian prion in the amyloid state has been determined.

1.3 The amyloidogenesis of prion protein

The term "amyloid" depicts a specific type of elongated, unbranched protein fibril, which was first introduced by physician Rudolf Virchow to describe a macroscopic tissue abnormality that produced a positive result in an iodine-staining reaction, bearing much of resemblance with the characteristic of starch (Sipe and Cohen 2000). The Latin word for starch is *amylum*, which then became the etymology of amyloid (Sipe, Benson et al. 2014). As defined by biophysical scientists, amyloids are viewed as denatured protein aggregates and the fibrils must display the 'cross-β' diffraction pattern caused by the cross-β-sheet motif when irradiated with X-rays (Riek and Eisenberg 2016). This kind of structure is composed of tightly interacting intermolecular β-sheets, and each β-sheet comprises thousands of identical copies of the same β-strand that connect and stack through hydrogen bonding.

Two general biochemical properties account for the biological effects of amyloid, including the fact that amyloid-forming proteins can switch from soluble monomers to insoluble fibrils (aggregation), and that the structure of amyloids is repetitive and might persist indefinitely (Riek and Eisenberg 2016). The study of amyloids over the past half century has revealed that numerous proteins form amyloid fibrils, and more than 40 proteins have been known to form pathogenic amyloid fibrils (Sipe, Benson et al. 2014). In the case of prion diseases, the infectious variant of prion protein (PrP^{Sc}) can even lead to severe neurodegenerative diseases in mammals.

Though the structure of PrP^{Sc} have not been resolved in high resolution yet, the protein aggregates caused by PrP^{Sc} had been observed and recorded since the 1980s. The morphology of PrP^{27-30} from the brain tissue of autopsy was first observed by transmission electron microscope (TEM) as rod-shaped structure, and it conformed to

11

the definition of amyloid after being stained by Congo red (Prusiner, McKinley et al. 1983). In addition, the secondary structures of PrP^{27-30} was analyzed by Fourier-transform infrared spectroscopy (FT-IR), and high percentage of β-sheet was obtained, which also resemble the feature of amyloid (Caughey, Dong et al. 1991). The amyloid plaques that were found from the brain tissues of prion diseases patients were later proved as PrP^{Sc} by immunostaining (Dearmond, McKinley et al. 1985), making amyloidogensis the main reason for prion proteins to be infectious.

The pathogenesis of prion diseases is due to the conformational rearrangement from PrP^{C} to PrP^{Sc} in the brain (Prusiner 1998, Aguzzi and Polymenidou 2004, Weissmann 2004). The amyloid PrP^{Sc} serves as an infectious seed, which recruits soluble PrP^{C} for extension. The growing amyloid can then fragment to produce further infectious seeds, which implies that prions are essentially infectious proteins (Figure 1.3). Though various amyloid-forming proteins such as amyloid-β, tau protein and α-synuclein, have different primary structures, amyloid fibrils have common characteristics and can be tested by certain means for visualization, for instance, Thioflavin T (ThT) binds specifically to amyloid fibrils and emits fluorescence at 485 nm when excited at this wavelength (Naiki, Okoshi et al. 2016). The formation of amyloid fibrils can be monitored by ThT binding assay, in which a lag phase for nucleation is usually present at the initial step in the absence of seeds, but in the presence of seeds, amyloid fibrils rapidly form without a lag phase (Figure 1.4).

12
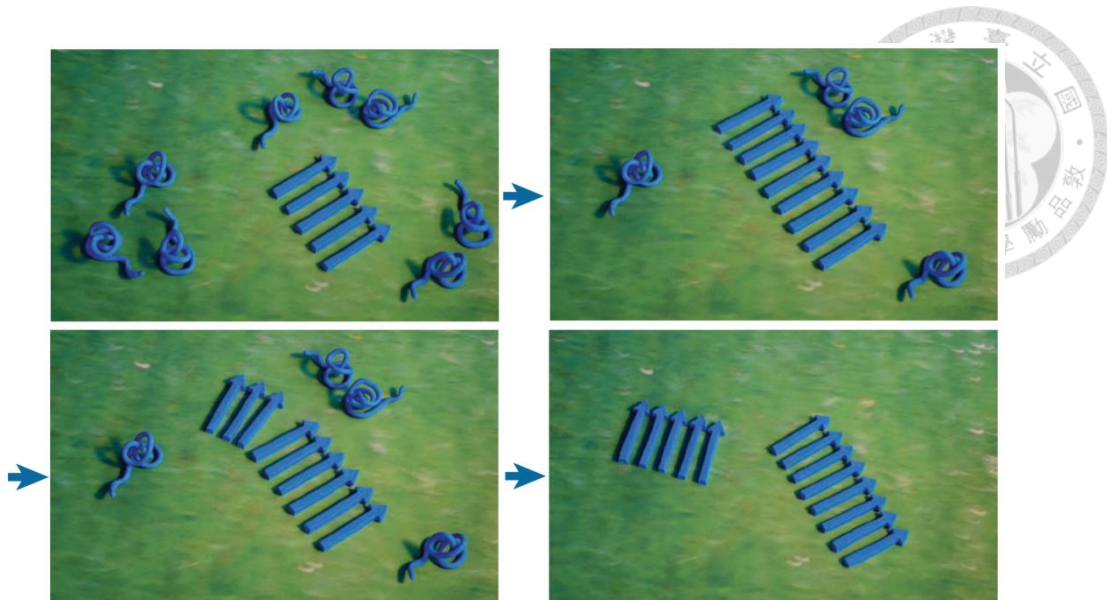
**Figure 1.3 Schematic representation of the elongation process of amyloids.**

An amyloid seed (array of five blue arrows) recruits soluble monomers (blue coils) and propagate. The growing amyloid might break into smaller pieces and recruit more monomers, therefore increasing the scale of misfolded proteins. The green background represents the environment of amyloid elongation (Riek and Eisenberg 2016).
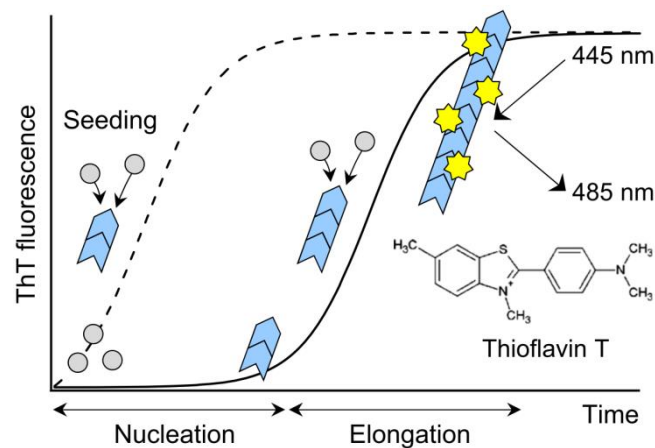
Figure 1.4 Kinetics of the formation of amyloid fibrils monitored by thioflavin T (ThT) fluorescence.

ThT emits fluorescence at 485-487 nm only when it is excited at 442-445 nm after binding specifically to the amyloid fibrils. In the absence of seeds, the kinetics of amyloid fibril formation shows a sigmoidal curve (solid line). The initial lag phase represents nucleation of amyloid fibrils, and the following growth phase represents an elongation of amyloid fibrils. In the presence of seeds, amyloid fibrils rapidly form by seeding without a lag phase (dashed line), indicating that nucleation is a rate-limiting step in amyloid fibrillation (Yamaguchi and Kuwata 2017).
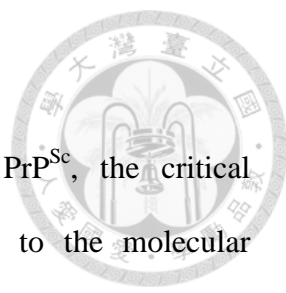
13

The hypothetic process of amyloid fibril aggregation had been proposed as a model, that is, the nucleation-dependent polymerization model (Dobson 2003, Chiti and Dobson 2006, Cohen, Linse et al. 2013), which had been described in the fibril formation of both amyloid-β (Jarrett and Lansbury 1993) and prion protein (Lee and Chen 2007). Since that the formation of nucleation seed is rate limiting, in the absence of seeds, there is a significant lag period for the formation of fibrils, which is followed by a rapid fibril elongation phase where a large percentage of the monomers is converted into fibrils. However, the lag time for fibril formation can be dramatically shortened by the addition of fibril seeds to monomer solutions (Jarrett and Lansbury 1993) (Figure 1.5). The nucleation-dependent formation of β_2-microglobulin (β_2m) amyloid fibrils had also been characterized by involving global analysis of a large number of reaction progress curves (Xue, Homans et al. 2008), revealing that this model can be applied mostly to those common amyloidogenic proteins.
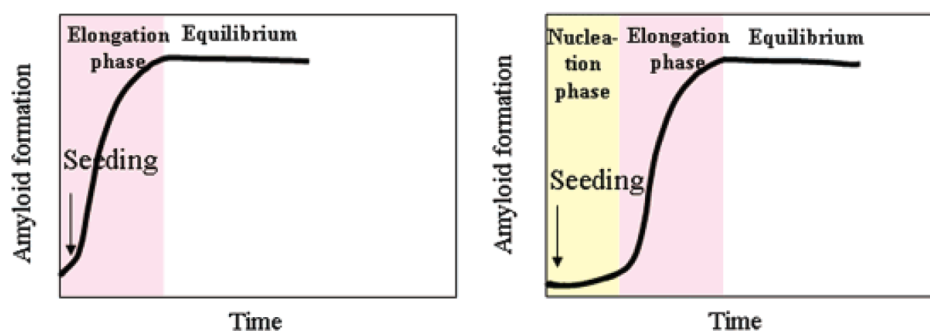
Figure 1.5 Seeding in nucleation-dependent polymerization model for amyloidogenesis.

The yellow background in the figure represents the first nucleation phase, and the pink background represents the second elongation phase, with the white background representing last phase of equilibrium. If the amount of exogenously added nuclei (seed) is equal to, or higher than, the critical seed concentration (left panel), the propagation phase starts immediately. If the acquired seed amount is lower than the critical seed concentration (right panel), the nucleation step continues until the critical concentration is reached (Lee and Chen 2007).

14

1.4 Critical regions of PrP in amyloidogenesis

To take a closer look at the conversion from PrP^C to PrP^{Sc}, the critical amyloidogenic regions of prion protein, which are key factors to the molecular pathogenesis of prion diseases, have been studied extensively by various groups. In the *in vitro* experiments of fibrillogenesis using synthetic peptides homologous to consecutive segments of Gerstmann-Sträussler-Scheinker (GSS) amyloid protein, the findings suggested that the sequence spanning residues 106-147 of PrP is central to amyloid fibril formation in GSS and related to encephalopathies (Tagliavini, Prelli et al. 1993). The most highly amyloidogenic region was also reported AGAAAAGA, which corresponds to Syrian hamster PrP residues 113−120 (Gasset, Baldwin et al. 1992), which had been characterized by NMR-detected hydrogen-deuterium exchange MS in mouse prion protein 106-126, revealing approximately 50% beta-sheet structure in the fibrils (Kuwata, Matumoto et al. 2003). For the structural elucidation of prion peptide by solid-state NMR, the molecular structure of prion amyloid fibrils had also been investigated, including fibrils formed by residues 127 to 147 of the human prion protein and hydrophobic fragment 113-127 of Syrian hamster prion protein, the latter of which was reported the formation of steric zipper structure where the residues of two neighboring β-sheet layers are tightly interdigitated (Figure 1.6) (Lin, Chao et al. 2010, Cheng, Tsai et al. 2011, Cheng, Huang William et al. 2013).

In recent reports regarding N-terminal region of prion protein, it had been stated that recombinant C-terminally truncated prion protein PrP23-144 (Y145Stop PrP variant) could spontaneously forms amyloid fibrils with a parallel in-register β-sheet architecture, and the β-sheet core was proposed to be mapped to residues 112-139. Furthermore, the amyloid fibrils generated from recombinant fragment 23-144 could both seed

15
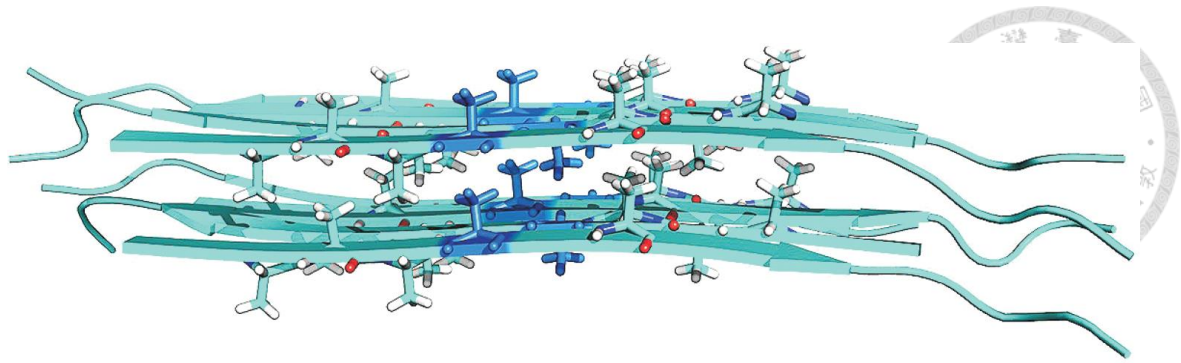
Figure 1.6 The structural model of the PrP113-127 fibrils.
The structure belongs to the class 7 steric zipper. The residues A118 are highlighted in deep blue since the distance corresponding to A118 is significantly shorter than other neighboring residues (Cheng, Huang William et al. 2013).

conversion of full-length PrP^C to a PrP^{Sc} in vitro and cause prion disease in transgenic and wild-type mice after the amplification process of protein misfolding cyclic amplification (PMCA) (Choi, Cali et al. 2016). In addition, species-dependent structural polymorphism of Y145Stop prion protein amyloid was also examined by solid-state NMR spectroscopy between species of human, mouse, and Syrian hamster, showing that structural differences are largely controlled by two amino acids at positions 112 and 139 as conformational switches, which are also key to the emergence of structurally distinct amyloid strains within the same protein sequence (Theint, Nadaud et al. 2017). Finally, molecular dynamics simulations had been used widely to investigate the structures of N-terminal prion peptides 120-144. Amino acid substitutions like I138M and I139M would retard the formation of parallel in-register β-sheet dimers during the nucleation stage, and deletion of the C-terminal residues 138-144 would prevent formation of fibrillar structures. The same sequence from different species might also aggregate via multiple nucleation-dependent pathways to form various shapes of protofilaments (Figure 1.7) (Wang, Shao et al. 2016).
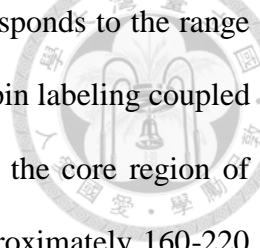
16
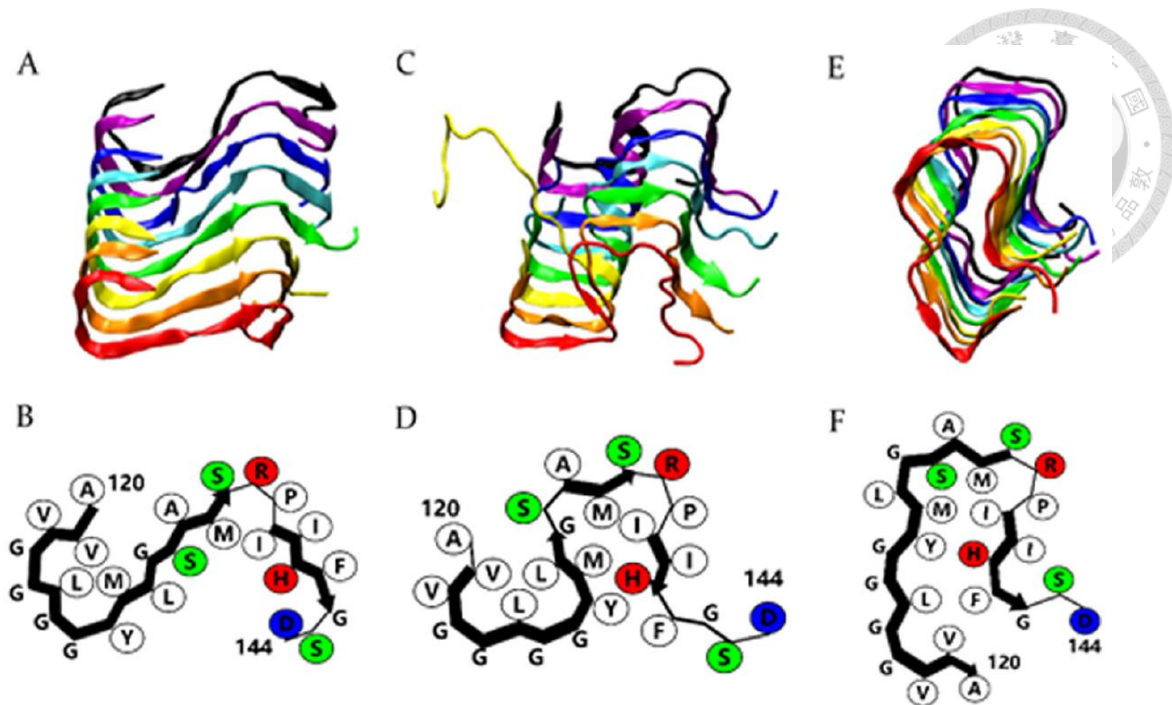
Figure 1.7 Structures of HuPrP(120-144) protofilaments by MD simulations and corresponding schematic representations.
Structures of S-shaped (A), Ω-shaped (C), and U-shaped (E) protofilaments formed by HuPrP(120-144) from certain runs are shown, and schematic representations of peptide conformations in the S-, Ω-, and U-shaped protofilaments are shown in B, D, and F. The sizes of the side chain beads do not reflect the actual radii. Hydrophobic residues (white), positively charged residues (red), negatively charged residues (blue), and polar residues (green) are shown (Wang, Shao et al. 2016).

In addition to the studies at the N-terminal regions, C-terminal parts had also been examined and mapped. A version of deletion mutant of PrP, which was deprived either in segment 23-88 or 141-176 and consisted of 106 amino acid residues, showed conversion to PrP^Sc in transgenic mice and formed β-sheet-rich aggregates, implying that the core region of PrP^Sc contains the regions of PrP^C other than these two segments (Gajdusek, Gibbs jun et al. 1966, Muramoto, Scott et al. 1996, Baskakov, Aagaard et al. 2000). The hydrogen-deuterium exchange mass spectrometry (HXMS) analysis was later used to examine the structure of amyloid fibrils of human PrP90-231 and revealed similar results (Lu, Wintrode et al. 2007). These results located the core region onto the

17

C-terminal part (starting approximately at residue 169), which corresponds to the range starting from helix 2 to the middle of helix 3 in PrP^C. Site-directed spin labeling coupled with electron spin resonance spectroscopy (ESR) also showed that the core region of human PrP amyloid fibril falls onto the C-terminal residues at approximately 160-220 (Cobb, Sönnichsen et al. 2007). To take a deeper look at this region, the structural analysis of mouse prion peptide including H2 and H3 showed that they formed quite different structures under the scope of electron microscopy. Along with different seeding efficiency exhibited in the seeding assay, the results implied that the region of H2 rather than H3 in mPrP has great potential for initiating fibril formation, and would be crucial for the nucleation-dependent replication process of the prion protein (Yamaguchi, Matsumoto et al. 2008).

Transmission barrier between species has always been another issue of study, which would affect the critical regions in the amyloidogenesis of prion protein from different species as well. In the region of prion peptide 108-144, only five residues differ among these differences and leading to high percentage of homology, but the transmissibility could vary in big extent (Figure 1.8). Previous study showed that Syrian hamster PrP(23-144) can seed the fibrillation of mouse PrP(23-144) while mouse PrP(23-144) cannot seed the fibrillation of Syrian hamster PrP(23-144), indicating that there is an asymmetric relationship of cross-seeding between mouse and Syrian hamster PrP. In addition, species-specific substitution of a single amino acid in a critical region would change the seeding specificity of prion protein fibrils. To be more specific, once the mutant I138M was present in human prion protein PrP23-144, the seeds from it could seed the proteins of mouse and human wild-type protein but not the hamster one; when the mutant I138M and I139M were present simultaneously in human prion

18

```
              108                                    144
Hamster    NMKHMAGAAAAGAVVGGLGGYMLGSAMSRPMMHFGND
Mouse      NLKHVAGAAAAGAVVGGLGGYMLGSAMSRPMIHFGND
Human      NMKHMAGAAAAGAVVGGLGGYMLGSAMSRPIIHFGSD
```

Figure 1.8 Sequences of prion peptide 108-144 among Syrian hamster, mouse and human.

Sequences 108-144 of prion peptide from three different species are aligned, showing residue variance in 109, 112, 138, 139, and 143.

protein, the seeds from it could seed the proteins of hamster and mouse wild-type protein instead of the original human one (Vanik, Surewicz et al. 2004). Another study had produced mutant M138I and M139I in hamster prion protein, and similar secondary structures and morphologies were obtained compared to the ones of human prion protein PrP23-144 (Jones and Surewicz 2005).

Recent studies suggested that not only residue 139 but also 112 was important in PrP23-144 based on which sequences were chosen, including the M/V polymorphism in residue 112 and I/M polymorphism in residue 139 (Theint, Nadaud et al. 2017) (Figure 1.9). Last but not least, in the latest study, seeding and cross-seeding efficiency were compared between different species by molecular dynamics simulations. From the cross-seeding simulation of human, bank vole (a kind of species of mice) and hamster PrP(120-144), it was found that human PrP(120-144) has a strong tendency to adopt the conformation of the bank vole seed and vice versa, suggesting that human and bank vole PrP(120-144) might have a low cross-seeding barrier. On the other hand, the hamster seed had low efficiency in seeding the monomers of human and bank vole, indicating that hamster PrP(120-144) might have a high cross-seeding barrier with the

19
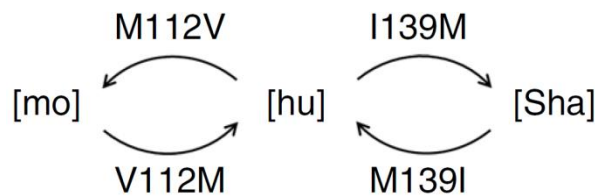
Figure 1.9 Schematic summaries of the key amino acid substitutions.
The summaries were primarily responsible for the PrP23-144 amyloid β-core adopting [hu], [mo], or [Sha]-like structures based on the solid-state NMR data in previous study. hu: human; mo: mouse; Sha: Syrian hamster (Theint, Nadaud et al. 2017).

other two. All of the results in simulation were consistent with experimental findings on the species-dependent seeding specificity of PrP(138-143), and these also fit with the hypotheses of 139 polymorphism described above (Apostol, Wiltzius et al. 2011, Wang and Hall Carol 2018).
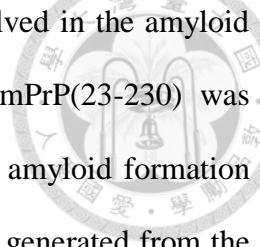
In the previous paper published by our lab, the amyloidogenic properties of peptides 108-144 from several mammalian prion proteins were compared and discussed on the basis of the chemical and structural properties of the amino acids that were varied. Substitution of V112M in the bovine PrP peptide would accelerate the rate of nucleation compared to the wild-type, and on the contrary, substitutions of I139M and N143S would bring the opposite effects (Chuang, Liao et al. 2013). In another paper regarding species barrier between hamster and mouse, seeding efficiency was evaluated by seed titration method between different combination of substituted monomer and seed. It was found that when the seed contained I139, the binding surface is in the C-terminal part and the homology of I139 between seed and monomer would determine the cross-species seeding efficiency; when the residue of 139 was methionine in seed, the binding surface would be in the N-terminal part, and the seeding efficiency would be determined by the homology of 109 and 112 between the seed and monomer. The

20

hypothesis of "convertible binding surface" was proposed and diagramed in Figure 1.10, aiming to explain how amino acid sequences could determine the efficiency of PrP transmission between different species (Lee and Chen 2007).
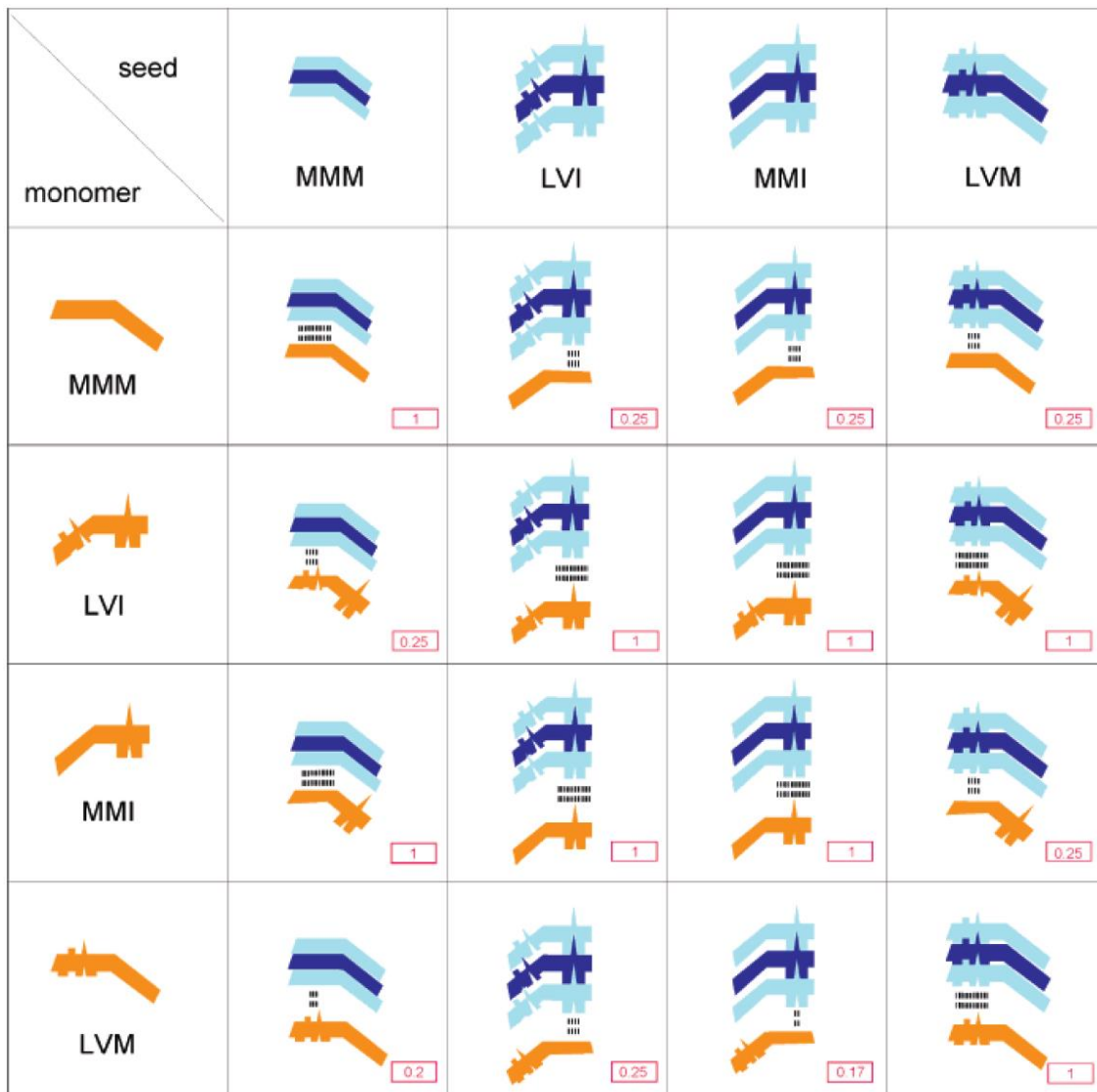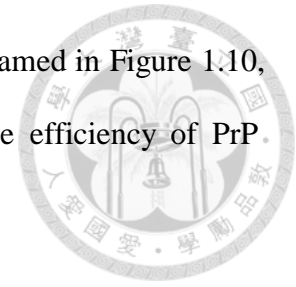
Figure 1.10 Schematic representation of "convertible binding surface" hypothesis. This hypothesis establishes the model that explains the sequence-dependent seeding efficiency. The density of the dotted lines between the seed (sky blue and navy) and monomer (orange) proportionally represents the strength of the binding affinity between them. The seeding efficiency (normalized to homologous seeding) for each seeding experiment is shown in the scarlet hollow box at the corner of each grid, with a number between 0 and 1 in it (Lee and Chen 2007).

In the most related paper published in 2013, the segment involved in the amyloid core formed from recombinant full-length mouse prion protein mPrP(23-230) was investigated with three shorter segments of peptides. Seed-induced amyloid formation from recombinant prion protein was carried out, and the seeds were generated from the peptides mPrP(107-143), mPrP(107-126), and mPrP(127-143). The results showed that the amyloid fibrils formed from mPrP(107-143) and mPrP(127-143) were able to seed the amyloidogenesis of mPrP(23-230), but those from mPrP(107-126) did not have the capacity of seeding, showing that the segment of sequence 127-143 was used to form the amyloid core in the fibrillization of mPrP(23-230) (Chatterjee, Lee et al. 2013).

The thesis written by Howard Chih-Hao Shen followed the same route of the study except that the target of interest was replaced by hamster prion protein and peptides. Interestingly, the result was the just the opposite: the amyloid fibrils from SHaPrP(108-144) and SHaPrP(108-127) were able to seed the amyloidogenesis of SHaPrP(23-231), but those from SHaPrP(128-144) did not have the capacity of seeding. In addition to exhibiting the different location of amyloid core in fibrillization, this pair of results could exactly be used to explain why species barrier exist during transmission and why different kinds of residue on 139 would make the different efficiency of seeding. By possessing the same I139 residue (as in human and mouse), the homology of I139 is more important accompanied with the amyloid core locating near the C-terminal part of the peptide (mPrP 127-143); and when the same residue of M139 was possessed (as in hamster and mutant of either human or mouse), the homology of 109 and 112 is more important accompanied with the amyloid core locating near the N-terminal part of the peptide (SHaPrP 108-127). It is only when the sequences are changed as mutants that the amyloid core would shift and become applicable for

cross-species seeding.

Though the results described above could perfectly match, it is still not clear what region of residues in the segments, whether mPrP 127-143 or SHaPrP 108-127, are the very key role that are responsible for the determination of amyloid core location. Powerful tools that can offer better resolution upon each individual residue are still required in order to take a closer look at these segments, and techniques such as solid-state NMR and ESR spectroscopy can provide information of mutual distance regarding individual residues in the amyloid fibril structure by interpreting their spectra and signals.

23
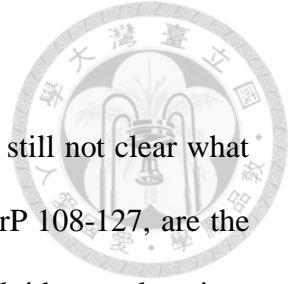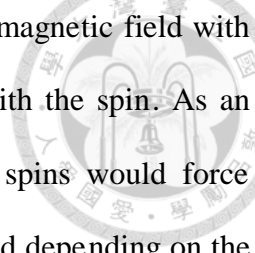
1.5   Previous studies of prion protein structure by ESR

In the field of protein structural determination, there have been powerful tools including nuclear magnetic resonance (NMR) and X-ray crystallography that can help the researchers obtain resolutions down to atomic level. However, there are still many limitations in these techniques that not all of the proteins are suitable for these two methods. For example, structures of proteins of high hydrophobicity like membrane proteins, highly dynamic or intrinsically disordered proteins and enormous protein-protein complex could not be solved since these biomolecules cannot be crystalized or are subject to aggregation or precipitation. Alternative methods including atomic force microscopy (AFM), small-angle X-ray scattering (SAXS), solid-state NMR, cryo-electron microscopy (Cryo-EM) and electron spin resonance (ESR) spectroscopy had been developed to interpret the structures of these subjects from another perspective (Koch, Vachette et al. 2003, Henderson 2004, Stopar, Štrancar et al. 2005) .

The structure of prion protein was an example for these alternative approaches since it could easily switch its conformation to insoluble state under various circumstances. ESR was an ideal tool to investigate the structure of this protein since it can detect its structural conversion on a picosecond to nanosecond timescale, and also it is applicable to soluble samples in various conditions (Grigoryants, Veselov et al. 2000). ESR spectroscopy is often coupled with site-directed spin labeling (SDSL) for it introduced a cysteine residue in the sequence of study through mutagenesis, and sulfhydryl-specific nitroxide spin labels can bind to the cysteine residue through covalent binding, serving as probes for the detection of the movement of the backbone residue. Detailed principles of ESR spectroscopy had been organized by the previous

24

thesis written by Che Yang. In brief, the interaction of an external magnetic field with an electron spin depends upon the magnetic moment associated with the spin. As an external magnetic field is applied, the magnetic moment of the spins would force themselves to align either parallel or antiparallel to the magnetic field depending on the magnetic component (m_s, either $+\frac{1}{2}$ for antiparallel or $-\frac{1}{2}$ for parallel). The application of the magnetic field then provides a magnetic potential energy which splits the spin states by an amount proportional to the magnetic field, which is described as Zeeman effect. According to this effect, photon of the appropriate frequency (and thus energy, usually microwave) can cause a transition from one spin state to the other, leading to the phenomenon of resonance, which is featured in the name of this technique (ES<u>R</u>).

In the practical situation, proteins labeled with spins are composed of collections of many paramagnetic species, and the population of the unpaired electrons follows the distribution of Maxwell-Boltzmann distribution, which means that spins of lower energy are more in number than the higher ones. This had contributed to the net absorption of energy and had facilitated the ESR signals to be detected. Since an ESR spectrum could reveal the change of state of an electron spin, it might be thought that one curve of absorption would be obtained from all ESR spectra for a single electron spin. In the practical situation, the hyperfine interaction between unpaired electron and nearby nucleus results in splitting of the two energy states into additional levels, and this would cause the ESR signal split into doublets, triplets and even more. For spins like MTSSL, the unpaired electron on MTSSL would interact with the nearby nitrogen, thus the three-lined spectra can be observed in the range of X-band frequency (~ 9.75 GHz) (Figure 1.11).

25

ESR spectroscopy had been used to investigate the structures of amyloid protein aggregates including amyloid-β, tau and prion protein (Török, Milton et al. 2002, Margittai and Langen 2004, Yang, Lo et al. 2015) since they all could not form crystallized structures. Solid-state NMR could be another useful tool for investigating the amyloid fibril structures (Lin, Chao et al. 2010, Cheng, Tsai et al. 2011, Cheng, Huang William et al. 2013), but since the isotope labeling on long sequences of peptide or protein could cost big amount of money, it had only been used in sequences up to 20 residues, which could only visualize limited regional structures compared to the full-length protein. In contrast, ESR along with site-directed spin labeling is cheaper in cost and could help us analyze structures in almost every residue on the peptide or protein, and the experimental procedures require no extra protection from radioactive substances, making it a better choice for structural elucidation of amyloid fibrils. The illustration regarding site-directed spin labeling and interpretation of ESR spectrograms can be seen at Figure 1.12.
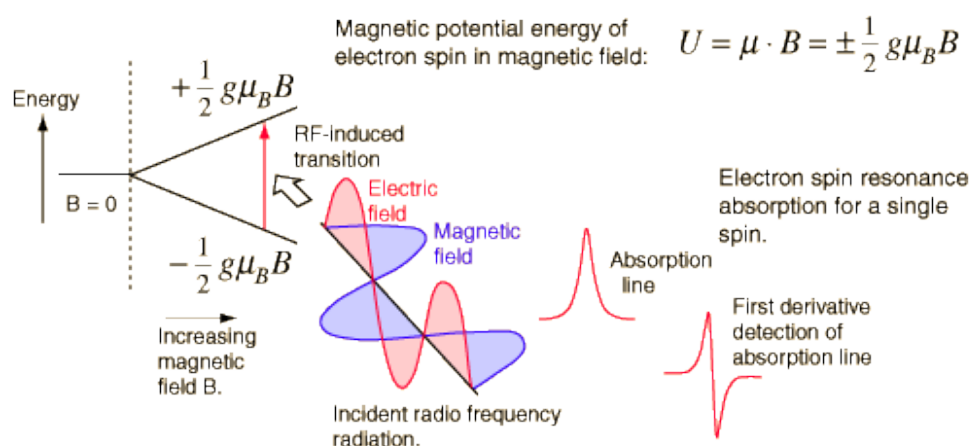
Figure 1.11 Overall principles of ESR spectroscopy.
The ESR spectra are obtained from absorption of energy when transition of electrons occurs between different states of magnetic potential energy under an applied external magnetic field. The spectra are obtained as the first derivative detection of absorption line (http://hyperphysics.phy-astr.gsu.edu/).

26

(A)   (B)
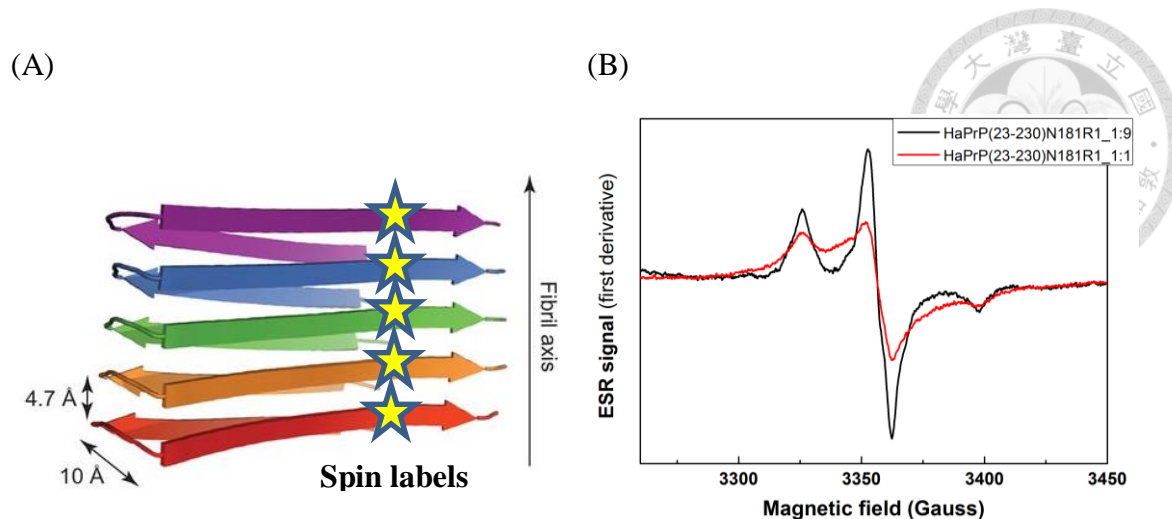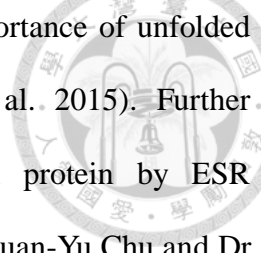
Figure 1.12 Schematic representation of site-directed spin-labeling (SDSL) and example of ESR spectrogram.

(A) Structure of the cross-β core of amyloid fibrils derived from NMR data. The star icons in the figure represent the spin labels (Sawyer, Claessen et al. 2012).

(B) An example of ESR spectrogram. The sharp shape of black curve represents no spin-spin interaction, and the broad shape of red line represents stronger spin-spin interaction. The ESR data shown here were completed and graphed by Dr. Yung-Han Chen in our lab.

In Figure 1.12, it was illustrated that different curve shapes of ESR spectrograms represent different strength of dipolar interaction between spins. The differences in linewidth were based on the fact that the signals from the spins would split if the spins were proximal to a certain extent, which is called spin exchange. The superposition of the splitting signals would cause the linewidth to be increased, making the curve shape broadened and shorter.

In the previous paper published by our lab, ESR spectroscopy was first used in the literature of 2015 investigating the transition between α-helical-dominant to β-sheet-rich conformer full-length mouse recombinant prion protein. By measuring dipolar interactions between spin probes during the transition, the ESR results allowed clear discrimination between the intra- and intermolecular distances between spin labeled

residues in helix 2, making it possible to demonstrate that the importance of unfolded helix 2 segment upon forming cross-β structure (Yang, Lo et al. 2015). Further structural elucidation of full-length mouse and hamster prion protein by ESR spectroscopy are being proceeded by other lab members including Kuan-Yu Chu and Dr. Yung-Han Chen. This thesis aims to serve as a counterpart of the study of full-length hamster prion protein.

In addition, in the thesis of Jenny Yu-Chieh Huang, spin-spin interaction between mutant H140R1 had been investigated between sequences of human, mouse and hamster prion peptide 108-144 (107-143 for mouse). The results showed that the ESR spectrum of hamster H140R1 mutant showed the sharpest curve compared to human, with the curve of mouse H140R1 the broadest. This result already gave a hint that the C-terminal part of the peptide in mouse might be near the amyloid core, thus leading to broader curve; the C-terminal part of the peptide in hamster is farther from its amyloid core and not as important as its N-terminal part, thus leading to sharper curve. Both of the results might also be consistent with previous results of Howard's thesis and Chatterjee's paper in 2013.

Based on the previously established methods of ESR spectroscopy, we now aim to continue the investigation of the hydrophobic core of N-terminal hamster prion protein by focusing only on segment 108-144 as a follow-up study of Jenny's thesis, Howard's thesis and Chatterjee's paper in 2013, expecting that ESR spectroscopy could serve a vision in higher resolution by visualizing differences between individual residues within the amyloid fibrils formed by the peptides.

1.6   Aim of this thesis

This thesis aims to gain insight into the structure of hamster prion peptide 108-144 by various methods and tools. The following are the two hypotheses in this study:
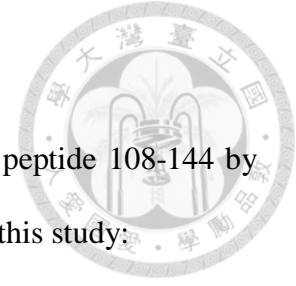
1. The spin-labeled prion peptides should exhibit similar kinetics of fibril formation by seeding assay as well as similar fibril morphology.

Site-directed spin-labeling had been used for structural elucidation on mouse prion protein in previous study (Yang, Lo et al. 2015), but investigation regarding spin-labeled hamster prion protein or peptide had not been published yet. In this study, both the kinetics of fibril formation and morphology of fibrils would be examined by ThT binding assay and TEM respectively, and finally ESR spectroscopy would be used for measuring spin-spin interaction between the fibrils. It is expected that the spin labeling would not cause big kinetic and structural changes in the resulting fibrils, and if so, seeding assay could help to offset the effects of it.

2. The curves of ESR spectrograms from spin-labeled mutants located within the hydrophobic region (~112-127) would be broadened due to the suspected location of amyloid core.

According to Howard's thesis, the segment of hamster prion peptide 108-127 has mutual seeding capacity with the full-length prion protein. Since this segment could serve as template and even amyloid core for fibril formation propagation, the distances between the fibrils in this segment must be relatively closer compared to other segments. Therefore, it is assumed that the spin-spin interaction in this region would be stronger, leading to the broadened curves of ESR spectrograms.

29

Chapter 2   Materials and Methods

2.1   Materials

2.1.1 Water

Water was distilled and deionized by Milli-RO PLUS 60 and Milli-QSP reagent water system in public instrument room, Institute of Biological Chemistry, Academia Sinica.

2.1.2 Chemicals

The following chemicals were obtained from the manufacturers listed as below and used without any further treatment.

Chemical	**Manufacturer**
1,2-Ethanedithiol (EDT)	Fluka Analytical®
4-Methylmorpholine, 99% (NMM)	Alfa Aesar
Acetic acid (glacial) 100%	Merck KGaA
Acetic anhydride	Honeywell Fluka™
Acetonitrile (HPLC Grade)	Fisher Scientific
Dichloromethane (DCM)	Honeywell Riedel-de Haën™
Dimethyl sulfoxide (DMSO)	J. T. Baker
Ethanol	J. T. Baker
Fmoc-Ala-OH	AnaSpec Inc.
Fmoc-Arg(Pbf)-OH	AnaSpec Inc.

31

Fmoc-L-Asn(Trt)-OH	CPC Scientific
Fmoc-L-Asp(OtBu)-OH	CPC Scientific
Fmoc-Cys(Trt)-OH	AnaSpec Inc.
Fmoc-Gln(Trt)-OH	AnaSpec Inc.
Fmoc-L-Glu(OtBu)-OH	CPC Scientific
Fmoc-Gly-OH	AnaSpec Inc.
Fmoc-His(Trt)-OH	AnaSpec Inc.
Fmoc-L-Ile-OH	CPC Scientific
Fmoc-L-Leu-OH	CPC Scientific
Fmoc-Lys(Boc)-OH	AnaSpec Inc.
Fmoc-Met-OH	AnaSpec Inc.
Fmoc-Phe-OH	AnaSpec Inc.
Fmoc-Pro-OH	AnaSpec Inc.
Fmoc-L-Ser(tBu)-OH	CPC Scientific
Fmoc-Thr(tBu)-OH	AnaSpec Inc.
Fmoc-Tyr(tBu)-OH	AnaSpec Inc.
Fmoc-Val-OH	AnaSpec Inc.
Glycerol	VWR Life Science
Hydrochloric acid	J. T. Baker
Methyl tert-Butyl Ether (MTBE)	Macron/Avantor

MOPS (3-(N-morpholino)propanesulfonic acid)	Sigma® Life Science
MTSSL ((1-Oxyl-2,2,5,5-tetramethylpyrroline-3-methyl methanethiosulfonate)	Enzo Life Sciences
N,N-Dimethylformamide (DMF)	Macron/Avantor
O-(1H-Benzotriazole-1-yl)-N,N,N',N'-tetramethyluronium hexafluorophosphate (HBTU)	Alfa Aesar
Phosphotungstic acid (PTA)	Electron Microscopy Sciences
Piperidine, 99%	U&I Bio-Tech, Inc.
Potassium chloride, Crystal	J.T. Baker
Rink Amide AM resin (200-400 mesh)	Novabiochem®
Sodium Azide	和光純藥工業株式会社
Sodium Chloride	VWR Life Scienc
Sodium hydroxide	Merck KGaA
Sodium phosphate dibasic dihydrate	Honeywell Fluka®
Sodium phosphate monobasic	Sigma-Aldrich
Thioflavin T (ThT)	Sigma
Trifluoroacetic acid, 99% (TFA)	Alfa Aesar
Triisopropylsilane (TIS)	Sigma-Aldrich
Uranyl acetate (UA)	Electron Microscopy Sciences
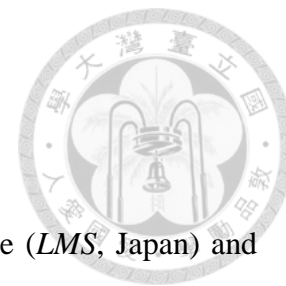
2.1.3 Laboratory instruments

(1) Centrifuge

Six different centrifuges were used. MCF-2360 Mini Centrifuge (*LMS*, Japan) and CM-600 Mini Microcentrifuge (*Hsiang Tai*, Taiwan) were used generally to spin down solutions in micro-centrifuge tube. Kubota 1710 (*Kubota*, Japan) and Kubota 3520 (*Kubota*, Japan) were used to spin down spin-labeled peptide precipitate or amyloid fibrils. Avanti^{TM} J-25 Centrifuge or Avanti$^®$ J-26 XPI Centrifuge (*Beckman Coulter, Inc.*, USA) was used to spin down the crude peptide after cleavage from resin. Allegra$^®$ X-15R Centrifuge (*Beckman Coulter, Inc.*, USA) was used to spin down amyloid fibrils in 10% glycerol to the capillaries.

(2) Peptide synthesizer

The peptides were synthesized using Rink Amide AM resin and fluorenylmethoxycarbonyl/ *tert*-butyl (Fmoc/*t*Bu)-protected amino acids on a PS3^{TM} peptide synthesizer (*Protein Technologies, Inc.*, USA).

(3) High performance liquid chromatography (HPLC)

Purification was carried out at room temperature on reversed-phase HPLC system including Agilent 1100 series and 1200 Infinity series variable wavelength (G1379A degasser, G1311A QartPump, G1329B 1260 ALS autosampler and G1365B MWD UV detector) linked to fraction collector CHF122SC (*ADVANTEC*, Japan). For peptide purification, analytical octadecylsilane (C18) column was used (25 cm×10 mm in length × internal diameter, 10 μm in particle size, 300 Å in pore size, Discovery$^®$ BIO

Wide Pore, *SUPELCO,* USA).

(4) Lyophilizer

Two instruments were used for lyophilization and to remove solvent from the samples, including FD-series freeze dryer accompanied with VO-series vacuum oven (*PANCHUM Scientific Corp.*, Taiwan) and FDM-20 Manifold Freeze Dryer (*UNISS*, Taiwan) in public instrument room, Institute of Biological Chemistry, Academia Sinica.

(5) Spectrofluorometer

The ThT fluorescence spectra were measured and recorded with a 3×3-mm path-length QS quartz cuvette on FP-750 spectrofluorometer (*Jasco*, Japan).

(6) UV-Visible spectrophotometer

The UV-Visible absorption spectra were measured on DU$^{®}$ 800 UV/Vis spectrophotometer (*Beckman Coulter, Inc.*, USA).

(7) Mass spectroscopy

Molecular mass of all peptides was identified by matrix-assisted laser desorption/ionization time-of-flight (MALDI-TOF) mass spectroscopy with Autoflex III MALDI-TOF/TOF Mass Spectrometer (*Bruker*, Germany) in Mass Spectrometer Facility at the Institute of Molecular Biology, Academia Sinica.

35

(8) Transmission electron microscope (TEM)

The amyloid fibrils and wild-type seed were observed on FEG-TEM (FEI Tecnai G2 TF20 Super TWIN, *ThermoFisher Scientific*, USA) in Core Facility of Image, Institute of Cellular and Organismic Biology, Academia Sinica.

(9) Electron Magnetic Resonance Spectrometer

The ESR samples were loaded into 0.8-mm capillaries and sent for measurement on EXEXSYS E-580 CW/Pulse electron magnetic resonance spectrometer (*Bruker*, Germany) in Instrument Center of National Tsing Hua University.

2.2 Methods

2.2.1 Solid-phase peptide synthesis

The Syrian hamster peptides (Table 2.1) used in this study were synthesized by Fmoc-polyamide solid phase synthesis method on PS3^{TM} peptide synthesizers (*Protein Technologies, Inc.*, USA). To start up the reaction, 0.4-0.5 mmole Fmoc/*t*Bu-protected amino acid derivatives and 0.3 mmole HBTU (~110 mg) were mixed in each synthesis tube, and 0.1 mmole Rink Amide AM resin (~150 mg) was added into a reaction vessel. HBTU was used as catalyst for amine nucleophilic attacking when reacting with carboxylic end of each Fmoc-protected amino acid derivatives. DMF acted as the primary solvent in all synthesis reactions. In each cycle of reaction, three steps were conducted by the machine, including deprotection, activation, and AA coupling, and the peptides are washed by DMF between different steps (Table 2.2). The deprotection reagent was 30 % (v/v) piperidine in DMF and the activation reagent was 4.45 % (v/v) NMM and 25% DMSO (v/v) in DMF. The coupling time of each Fmoc/*t*Bu-amino acid derivative depends on the sequence, ranging from 2 to 5 hours. These peptides were modified with acetylation at N-terminus and amidation at C-terminus by Rink Amide AM resin itself and coupling with acetic anhydride at the last cycle of the synthesis, in order to mimic their status in physiological condition.

After synthesis was completed, the crude peptides were washed with DMF, ethanol, and DCM sequentially in a G2 funnel in order to swell the resin and wash the internal space of the resin. The crude peptides were then dried *in vacuo* for 2 hours and weighed in a sample bottle on the electronic AB204-S Analytical Balance (*METTLER TOLEDO*, USA).

37

Table 2.1 Sequences of peptides synthesized and used in this thesis.

Mutants	Sequences
WT	CH_3CONH-NMKHMAGAAAAGAVVGGLGGYMLGSAMSRPMMHFGND-$CONH_2$
A113C	CH_3CONH-NMKHM**C**GAAAAGAVVGGLGGYMLGSAMSRPMMHFGND-$CONH_2$
A118C	CH_3CONH-NMKHMAGAAA**C**GAVVGGLGGYMLGSAMSRPMMHFGND-$CONH_2$
V121C	CH_3CONH-NMKHMAGAAAAGA**C**VGGLGGYMLGSAMSRPMMHFGND-$CONH_2$
L125C	CH_3CONH-NMKHMAGAAAAGAVVGG**C**GGYMLGSAMSRPMMHFGND-$CONH_2$
M129C	CH_3CONH-NMKHMAGAAAAGAVVGGLGGY**C**LGSAMSRPMMHFGND-$CONH_2$
M134C	CH_3CONH-NMKHMAGAAAAGAVVGGLGGYMLGSA**C**SRPMMHFGND-$CONH_2$
M138C	CH_3CONH-NMKHMAGAAAAGAVVGGLGGYMLGSAMSRP**C**MHFGND-$CONH_2$

Table 2.2 Steps in each cycle of peptide synthesis reaction.

Step	Reagent	Time	Repeat
1	SOLV	30 sec	×3
2	DEP	10-15 min	×2
3	SOLV	30 sec	×6
4	ACT	30 sec	×1
5	AA	2-5 hr	×1
6	SOLV	30 sec	×6

After the peptides were weighed, they were deprotected and cleaved from resin by stirring for 2 h at room temperature in the cleavage cocktail TFA / ddH$_2$O / EDT / TIS (94/2.5/2.5/1, v/v) (King, Fields et al. 1990). The volume of ddH$_2$O and EDT was set to be 250 μL on a basis of 500 mg crude peptide. During this process, TIS, water, and EDT served as nucleophilic reagents (scavengers) to quench highly reactive cationic species generated from the cleavage of side-chain protection groups (e.g. *tert*-butyl groups). In addition, EDT could be used to suppress acid-catalyzed methionine oxidation. The cleavage reaction was terminated by filtrating the mixture through a G3 funnel into 100 mL ice-cold methyl *tert*-butyl ether (MTBE) to remove the resin and precipitate the peptide. The white precipitate was then collected by centrifugation at 4,000 g for 20

38

minutes in 4°C, and the pellet was washed twice more with ice-cold MTBE for removing remnant TFA and other solvents. Finally the peptide was dried *in vacuo* for 4 hours.
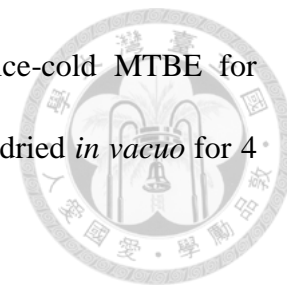
2.2.2 Peptide purification and identification

The dried peptides were dissolved in either 8-10% acetic acid or 30% acetonitrile with heating (to ~40°C) and sonication by Branson 3510-DTH Ultrasonic Cleaner for 4 hours, and filtrated through a non-pyrogenic, surfactant-free cellulose acetate Minisart® NML 0.2-μm syringe filter (*Sartorius Stedim Biotech*, Germany). The crude peptide solution was then purified by reversed-phase HPLC (*Agilent*, USA) using C18 analytical column (25 cm × 10 mm, *SUPELCO,* USA). The separation was performed by changing the mixing ratio of polar A buffer (94.9 % water / 5% acetonitrile / 0.1% TFA) and nonpolar B buffer (99.9% acetonitrile / 0.1% TFA), designated as gradient. The flow rate was kept at 3 mL/min and the column was kept in room temperature. Pure peptides were eluted out in specific solvent gradient, and the absorption was detected by UV detector at 220 and 275 nm. The detection of 275 nm was to identify the presence of tyrosine-included peptides. The molecular mass and purity of the peptides were examined by MALDI-TOF mass spectrometer (*Bruker*, Germany). After checking the identity of the purified product, the eluted peptide solutions were collected and lyophilized, and the remnant white peptide powder were stored in -30°C freezer (*SANYO*, Japan).

39

2.2.3 MTSSL spin labeling, purification, and identification of peptide
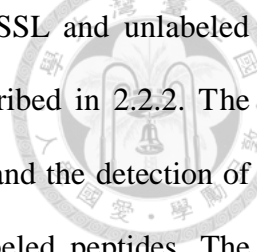
The dried peptides were dissolved in water, and the concentration was measured and adjusted to ~300 μM from absorbance at 280 nm by UV-Visible spectrophotometer. The peptide solution was then mixed with equal volume of 50 mM MOPS buffer (pH 6.5), and 126 mM 1-oxyl-2,2,5,5-tetramethyl-pyrroline-3-methyl) methanethiosulfonate (MTSSL) stock solution (in DMSO, stored in amber-colored Eppendorf tube, -30°C freezer) was added based on the mole of the peptides for spin labeling (Figure 2.1). The final molar ratio of cysteine to MTSSL was 1:4. The solution was incubated on rotator in speed of ~30 rpm for ~10 hours at room temperature in dark. After incubation, the solution was examined for the presence of white peptide precipitate. If no precipitate existed, the solution was sent for purification by reversed-phase HPLC directly. If precipitate existed, the solution would be centrifuged at 15,000 rpm for 20 minutes in 4 °C to collect the peptides, and the pellet was resuspended and dissolved in 34.5% B buffer in A buffer.
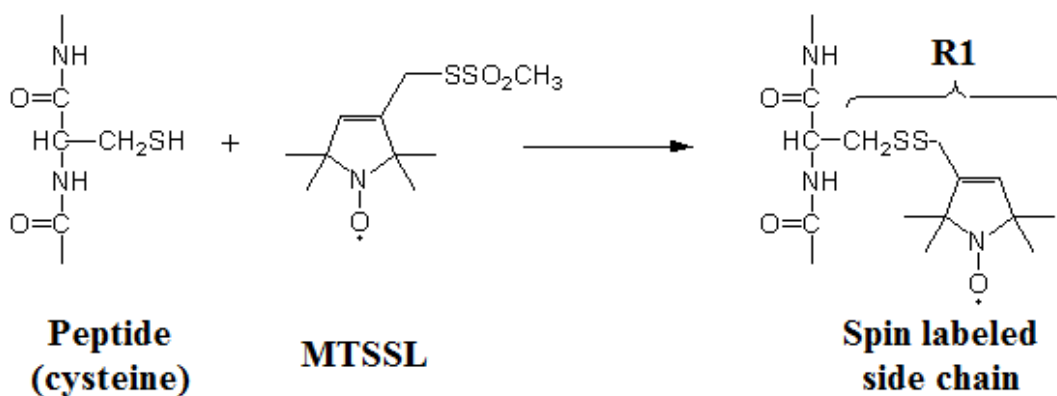
Figure 2.1 MTSSL spin labeling.
The disulfide between the thiol group of cysteine residue and MTSSL brings about the nitroxide side chain (designated R1).

40

Reversed-phase HPLC was used to remove excess free MTSSL and unlabeled peptides by using the same instruments, columns and buffer described in 2.2.2. The absorption was detected by UV detector at 220, 250, and 275 nm, and the detection of 250 nm made it possible to identify the presence of MTSSL-labeled peptides. The molecular mass and purity of the peptides were examined by the same MALDI-TOF mass spectrometer (*Bruker*, Germany). After checking the identity of the purified product, the eluted peptide solutions were collected and lyophilized, and the remnant white peptide powder was stored in -30°C freezer (*SANYO*, Japan).

2.2.4 Amyloid fibril formation

To prepare amyloid fibril formation samples, fibril formation buffer was first prepared by the mixture of 20 mM sodium phosphate buffer, 792 mM NaCl and 0.02% sodium azide (w/v). The pH value was adjusted to ~7.5 by addition of 10 N NaOH aliquots, and the solution was finally filtered through a Minisart® 0.2-μm syringe filter. The MTSSL-labeled peptides were dissolved in water, and the concentration was measured and adjusted to the desired one from absorbance at 280 nm by UV-Visible spectrophotometer. The amyloid fibril formation samples were prepared by mixing the fibril formation buffer with equal volume of the peptide solution incubated in Eppendorf tubes quiescently at 37°C (Lin, Chao et al. 2010). The incubation period was set to be ~190 hours (8 days) for measurement and recording of fluorescence intensities by ThT binding assay, and the samples were stored in 4°C refrigerator after the period was over.

41
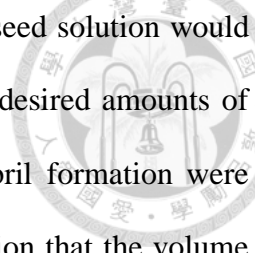
2.2.5 Seed preparation and the seeding assay

The seeds were prepared by ultrasonication of wild-type fibrils from the fibril formation of wild-type peptide monomers for the seeding assay. To calculate the quantity of the prepared seeds, the initial quantity of total peptide could be first calculated from the initial volume and peptide concentration of the fibril formation sample.

The amyloid fibril solution was first centrifuged at 15,000 rpm for 30 minutes in 4 °C, and the fibril pellet was resuspended by 400 μL water. The solution was then centrifuged and washed twice more with the same condition. The supernatants from different times of centrifugation were collected with the volume measured, and the quantity of the remnant peptide monomers was measured by UV-Visible spectrophotometer. Finally 400 μL water was added for resuspension of the fibril pellet.

To acquire nearly homogeneous seed, the fibril solution was ultrasonicated by UP200H ultrasonic processor (*Hielscher Ultrasonics*, Germany). 1-mm microtip was installed and washed by water and ethanol alternatively and wiped dry. The cycle of the ultrasonic processor was set to be 0.6, and the amplitude 20% (40 W). During the ultrasonication, the fibril solution was put on ice in order to cool down the heat generated by the vibration of the microtip. The fibril solution was ultrasonicated for 5 seconds for 20 cycles of intermittent pulses (5 pulses of 0.6 second each) with 5-second intervals between each cycle with the microtip immersed in the sample. After ultrasonication was completed, the seed was stored in 4 °C refrigerator for 1~2 hours for stabilization, and the micro-tip was washed and wiped dry again.

The amount of seeds could be finally calculated by subtracting the quantity of the remnant monomers in the supernatants from the initial quantity of total peptide. After

the concentration was determined from the volume (~400 μL), the seed solution would be diluted and added to the fibril formation samples based on the desired amounts of seed. The samples of spontaneous fibril formation and seeded fibril formation were prepared by the same procedure described in 2.2.4, with the exception that the volume of the seed should be included in the total volume of the samples in seeded fibril formation.

2.2.6 ThT binding assay in amyloidogenesis

Thioflavin T (ThT) is a highly sensitive fluorescence marker for amyloid fibrils that has been widely used for *in vitro* biomedical assays. The β sheet-rich amyloid fibrils have the ability to specifically bind to benzothiazole dyes. After binding, the benzothiazole group cannot rotate freely and would absorb energy from the excitation light due to structural torsion, emitting strong fluorescence at the wavelength of 487 nm (Figure 2.2) (Krebs, Bromley et al. 2005, Freire, de Araujo et al. 2014). Thus, ThT binding assay is a good way to monitor the process of amyloidogenesis and to distinguish the amyloid cross-β structure from amorphous aggregates (Khurana, Coleman et al. 2005).

43

A   **B**
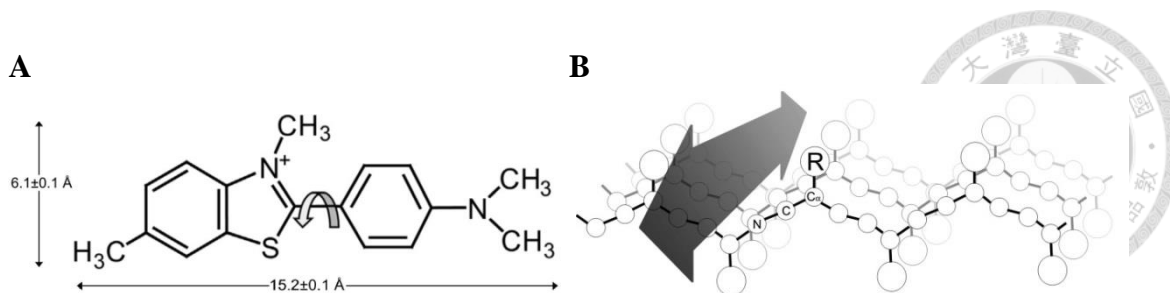
Figure 2.2 Thioflavin T and diagram of β-sheet structure.
(A) Molecular structure of thioflavin T (ThT). The torsion between the benzothiazole and the aminobenzene moieties is shown. The molecule is 4.3 ± 0.1 Å in thickness. **(B)** A schematic diagram of a β-sheet structure indicated with the backbone atoms (N, C, and C_α) and the side chain (R) for one residue. ThT is thought to bind with its long axis, which is parallel to the long axis of the arrow shown in this figure (Krebs, Bromley et al. 2005, Freire, de Araujo et al. 2014).

The 2 mM ThT stock solution was prepared by dissolving ThT in ThT dilution buffer (140 mM KCl, 100 mM sodium phosphate buffer, pH 8.5). A ThT working solution was prepared by diluting the stock to the final concentration 200 μM and filtered through a Minisart® 0.2-μm syringe filter, and finally stored in $4\,^\circ$C refrigerator.

In the process of fluorescence measurement, 30 μL aliquot of each sample was taken out at different times and mixed with equal volume of 200 μM ThT working solution in a 3×3-mm path-length QS quartz cuvette. After incubating for 1 minute in dark at room temperature, the quartz cuvette was put into the spectrofluorometer (*Jasco*, Japan), and the fluorescence spectra were measured from 450 to 600 nm with the excitation at 442 nm. The width of the excitation and emission slit was set to be 5 nm and 10 nm respectively. The scanning speed was set to be 125 nm/min, and the data pitch of 1 nm was employed. The incubation period was set to last within ~250 hrs (10 days) with the fluorescence spectra measured and recorded every 8 to 24 hours in average. After the period was over, the fluorescence spectra were plotted versus

44

measured wavelength, and the fluorescence intensities at 487 nm were plotted versus the incubation time.

2.2.7 TEM observation of fibril morphology

10 μL of fibril solution was loaded on a carbon-only coated 300-mesh copper grid for 3 minutes of adsorption, and the grid was washed with 200 μL water to remove salts in the fibril formation buffer. The sample was then negatively stained with either 2% phosphotungstic acid (PTA) or 2% uranyl acetate (UA) for 15-40 seconds. The grid was put in the AD-88s auto dry cabinet (*Eureka Dry Tech*, Taiwan) for drying overnight, and then the TEM images were taken on FEG-TEM (*ThermoFisher Scientific*, USA) in Core Facility of Image, Institute of Cellular and Organismic Biology, Academia Sinica.

2.2.8 Sample preparation for ESR spectroscopy measurement

After the process of fibril formation, the fibrils were spun down at 15,000 rpm for 30 minutes in 4 °C, and the fibril pellets were resuspended by 400 μL water repeatedly from different Eppendorf tubes and collected to the same tube. The solution was then centrifuged and washed twice more with the same condition. After removing the supernatant, the pellet was resuspended by 20 μL 10% glycerol, and the fibril solution was then spun down to a 90*0.8-mm borosilicate-glass capillary (*Kimble*, USA) in a 7-inch NMR tube (507-HP, *Norell, Inc.*, USA) in speed of ~1500 rpm by Allegra® X-15R Centrifuge (*Beckman Coulter, Inc.*, USA), with the help of 10-μL pipette tip inside the space of 50-mL Falcon tube. After centrifuging all the samples, the capillary was wrapped in alumni foil and stored in 4 °C refrigerator for follow-up ESR spectroscopy measurement.

45

2.2.9 ESR spectroscopy measurement

The ESR samples were sent for measurement on EXEXSYS E-580 CW/Pulse electron magnetic resonance spectrometer (*Bruker*, Germany) in Instrument Center of National Tsing Hua University by the aid of Dr. Yun-Wei Chiang's group. After the capillary was set into the spectrometer with an adapter, X-band continuous wave (cw)-ESR was measured at an operating frequency of ~9.42 GHz and 1.5 mW incident microwave power at the temperature of 200K. The sweep width of the measurement was 200 G, ranging from 3250 to 3450 Gauss.

2.2.10 Data analysis

For the data of fluorescence intensity at 487 nm in spontaneous fibril formation, the values of fluorescence intensity had excluded the portion from the control (water mixed with equal volume of fibril formation buffer). For the data in seeded fibril formation, the values of fluorescence intensity had excluded the portion from the control (diluted seed solution mixed with equal volume of fibril formation buffer) as well. For the data of fluorescence spectra, the spectra of the controls are shown along with the spectra of the fibril samples for comparison.

For the data of ESR spectra, the initial data were converted to 1024 data points by the aid of MATLAB (version R2015a). All spectra were normalized to the same number of spins by the aid of OriginPro (version 8.5). The number of spins was calculated from double integration of the raw data.

Chapter 3　Results (I): Sample Preparation

3.1　Synthesis, purification, and identification of peptides

3.1.1 Overview

In order to clarify the molecular mechanisms underlying the structural conversion of N-terminal prion peptide in the formation of amyloid fibril, the investigation of amyloidogenesis from chemically synthesized prion peptide have been conducted. There had been studies showing that the sequence of the N-terminal region had the determining power of seeding efficiency (Lee and Chen 2007, Chuang, Liao et al. 2013), and even different segments within this region could have different seeding capacity (Chatterjee, Lee et al. 2013) & Howard's thesis). The structure of this region was also studied by solid-state NMR, and formation of tightly interdigitated β-sheet layers was assumed (Lin, Chao et al. 2010, Cheng, Tsai et al. 2011, Cheng, Huang William et al. 2013). We thus proposed that the N-terminal region of prion protein might be the potential core region in amyloidogenesis.

In this thesis, the sequence 108-144 from Syrian hamster prion protein had been chosen as the sequence of the target peptide. From the wild-type sequence, seven hydrophobic, non-polar amino acid residues were picked out for substitution to cysteine respectively according to their positions and types of amino acids in the sequence. In the sequence, single residue of alanine, leucine, valine or methionine had been replaced for cysteine, generating seven different mutant peptides for further MTSSL spin labeling aside from the wild-type peptide itself. After the peptides were labeled with MTSSL spins, their nomenclature was altered by replacing the suffix "C" to "R1", e.g. from "A113C" to 'A113R1". Their molecular mass is listed in Table 3.1 respectively, which

47

was calculated from the freeware Protein Analysis WorkSheet (PAWS) (*ProteoMetrics*, USA). The molecular mass of the nitroxide R1 group linked to cysteine residue by disulfide was calculated to be 184.2 after MTSSL molecule released its methanesulfonic group. The values of molecular mass in the list are all monoisotopic instead of average.

Table 3.1 Synthesized peptides and their respective molecular mass.

Name	Molecular mass (Da)	Name	Molecular mass (Da)
WT	3705.676		
A113C	3737.648	**A113R1**	3921.842
A118C	3737.648	**A118R1**	3921.842
V121C	3709.616	**V121R1**	3893.810
L125C	3695.601	**L125R1**	3879.795
M129C	3677.644	**M129R1**	3861.838
M134C	3677.644	**M134R1**	3861.838
M138C	3677.644	**M138R1**	3861.838

The wild-type and mutant peptides were synthesized by solid-phase peptide synthesis method on a PS3™ peptide synthesizer. After being washed and dried *in vacuo*, the weights of the crude peptide were approximately 400-500 mg when using 0.4 mmole amino acid derivatives as synthesis materials, and 600-700 mg when 0.5 mmole amino acid derivatives were used. After the crude peptides were cleaved from the resin, dissolved in either 8-10% acetic acid or 30% acetonitrile and filtrated through a 0.2-μm syringe filter, they were purified by reversed-phase HPLC with a C18 column, and the products were collected by an autosampler based on fixed time of collection. The resulting chromatograms are shown in 3.1.2. The identity of the purified products was then checked by MALDI-TOF mass spectroscopy, with the resulting MS spectra shown in 3.1.3.

3.1.2 HPLC purification of peptides

All of the samples, including wild-type and mutants, were purified with three kinds of gradients including 24-40%, 24-42%, and 22-42% B buffer, and the products eluted out at approximately the same range of retention time (11-15 minutes), indicating that their properties inside the HPLC column were quite similar (Figure 3.1). Different kinds of solvents including 8-10% acetic acid and 30% acetonitrile had been used for solubility test on the peptides, but no significant differences were observed in either solubility or retention time in the process of purification.

(A) WT   (Elution at 28.6%)   **(B) A113C**   (Elution at 29.3%)

(C) A118C   (Elution at 28.1%)   **(D) V121C**   (Elution at 27.7%)

49

(E) L125C　　　(Elution at 26.7%)　**(F) M129C**　　　(Elution at 27.7%)

(G) M134C　　　(Elution at 27.8%)　**(H) M138C**　　　(Elution at 28.3%)
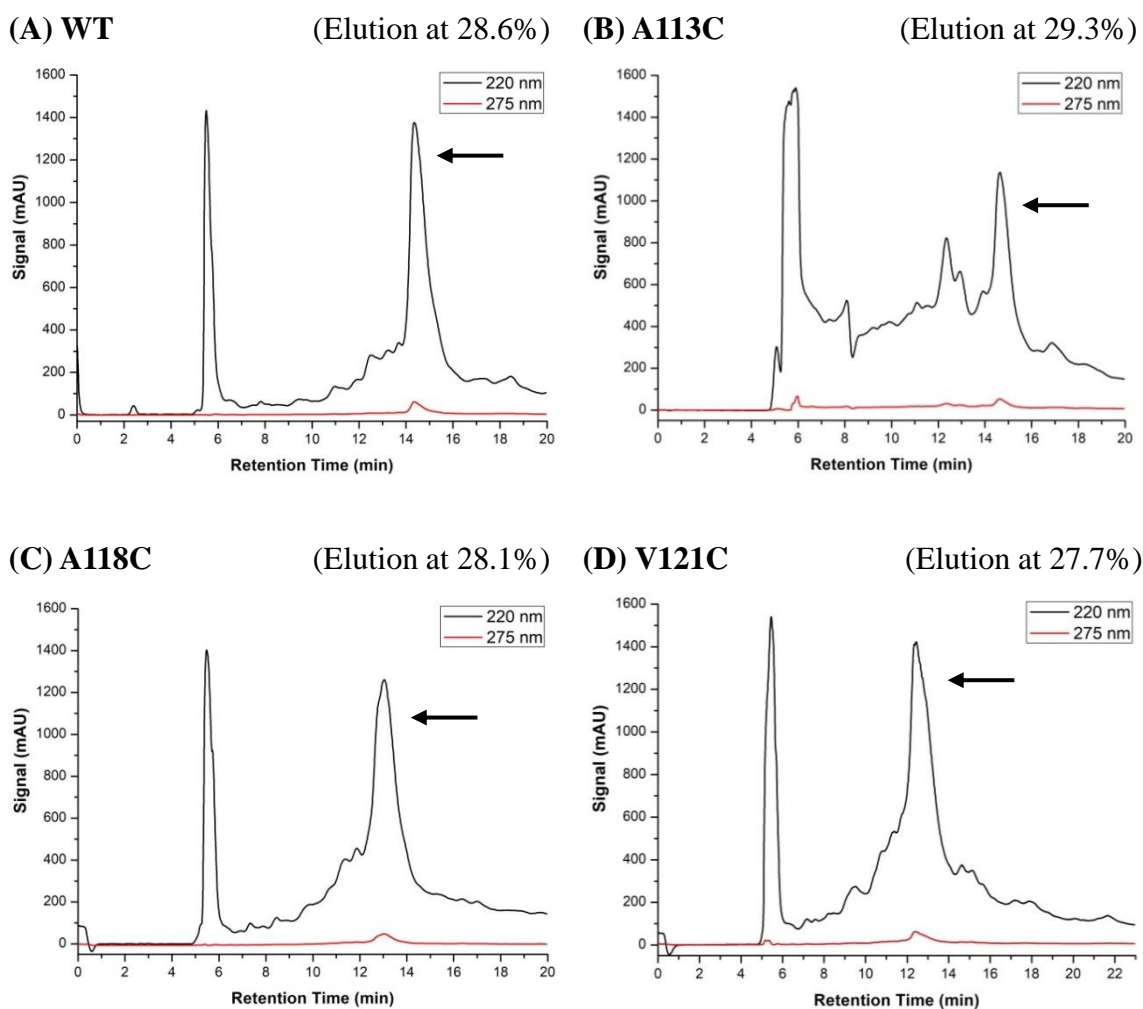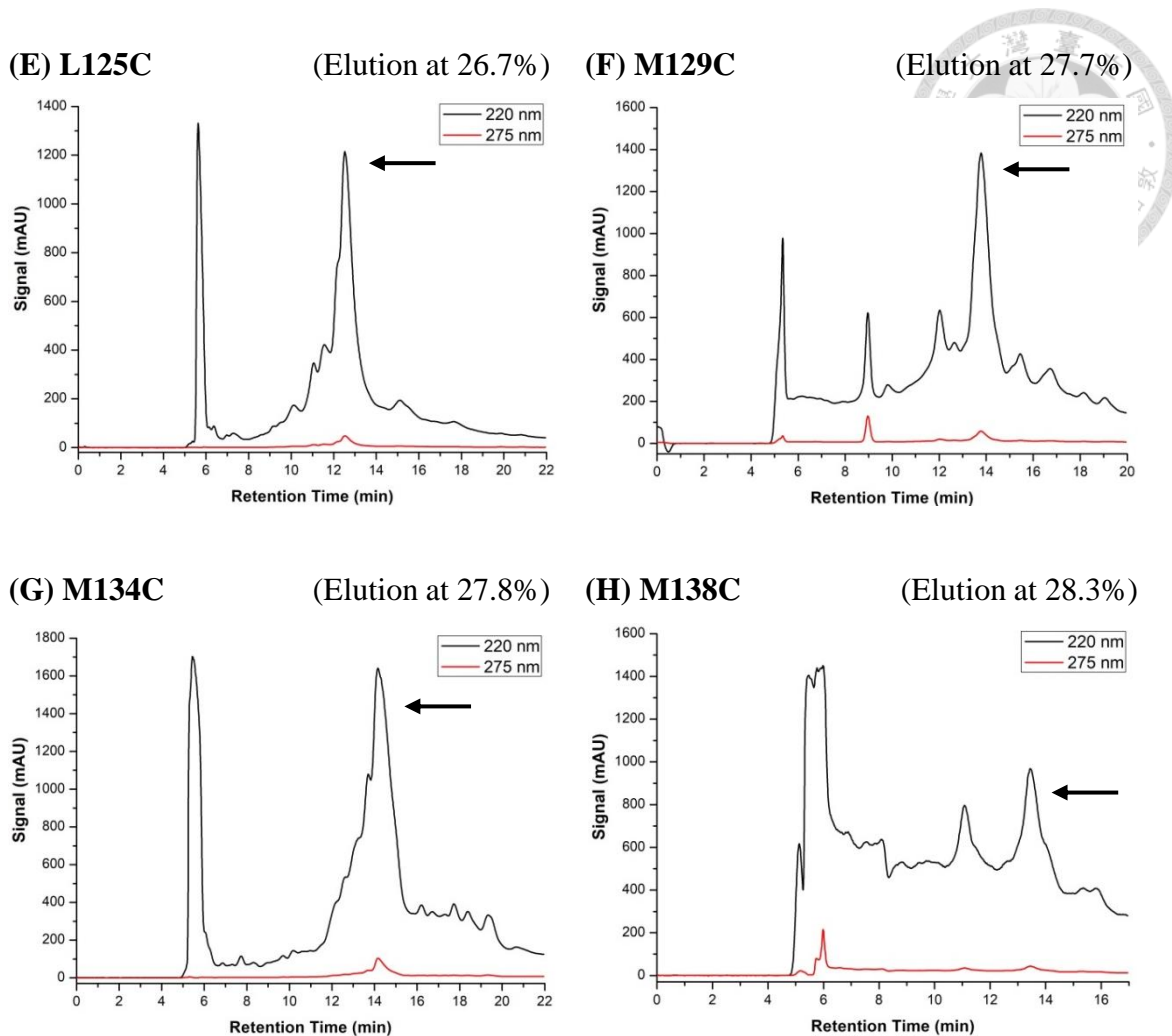
Figure 3.1 HPLC chromatograms showing the purification of HaPrP(108-144) peptides.

All of the peptides were purified with a C18 column. Samples of **(A)** WT, **(C)** A118C, **(D)** V121C, and **(H)** M138C were purified in the linear gradient of 24-40% B buffer, and **(B)** A113C was purified with 24-42% B buffer, with **(E)** L125C, **(F)** M129C, and **(G)** M134C purified with 22-42% B buffer. All of the sample purification was performed with the retention time of 30 minutes. The wavelengths of UV absorbance were set to be 220 nm and 275 nm for detection of total substances and tyrosine-containing peptides respectively. The solid arrows indicated the collected peaks of the peptides respectively. The solvent peaks appeared at approximately 5.5 minutes among all of the chromatograms.
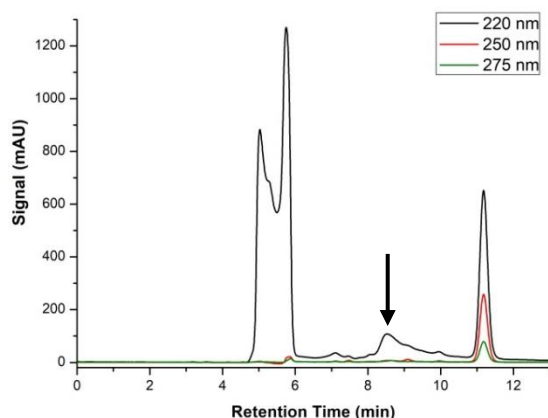
From the chromatograms above, it is obvious to see that all of the samples eluted within the same range of gradient around 27-29% B buffer, indicating that different sites

of cysteine residue mutant did not cause big changes in their properties, e.g. polarity or hydrophobicity. In addition, most of the major peaks were prominent to collect except for A113C and M138C, in which there were two to three obvious peaks. Usually, the peak with the highest intensity would be the correct products to collect based on previous experiences. Splitting of major peak was also a hint of the poor efficiency of solid-phase peptide synthesis and reducing amount of the desired products, which might be mutant-specific based on the chromatograms above.

3.1.3 Identification of peptides

After the elutes were collected in 50-mL Falcon tubes, 10 μL aliquot of the samples were taken out and sent for MALDI-TOF mass spectrometry analysis conducted by Ms. His-Lin Cheng in Mass Spectrometer Facility at the Institute of Molecular Biology, Academia Sinica (Figure 3.2). Aside from the purified samples, aliquot of the crude peptides were also sent for mass spectrometry analysis for precedent check before RP-HPLC purification once they were dissolved in the solvent, usually 8-10% acetic acid (Figure A.1).

(A) WT
(Theoretical molecular mass: 3705.676 Da)
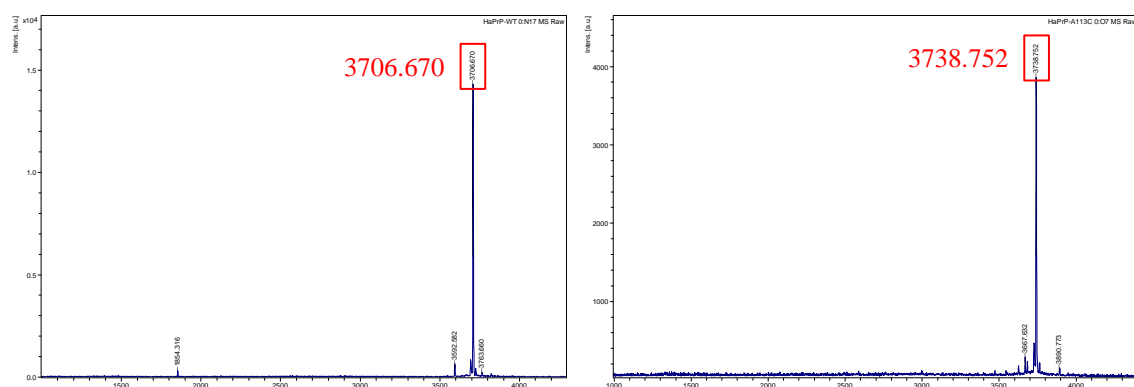
(B) A113C
(Theoretical molecular mass: 3737.648 Da)

51

(C) A118C
(Theoretical molecular mass: 3737.648 Da)
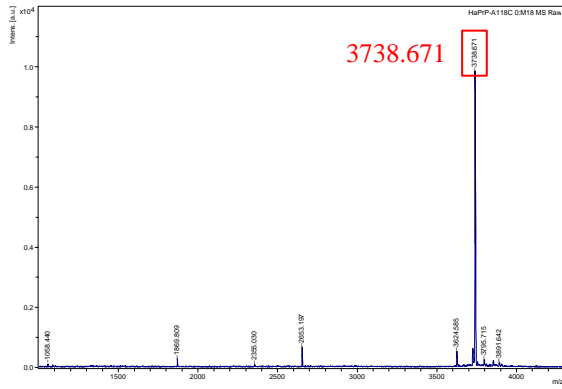
(D) V121C
(Theoretical molecular mass: 3709.616 Da)
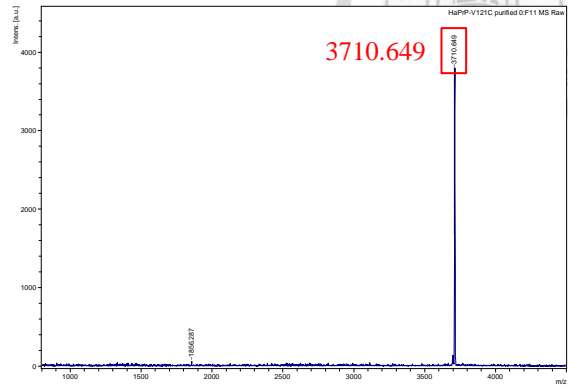
(E) L125C
(Theoretical molecular mass: 3695.601 Da)
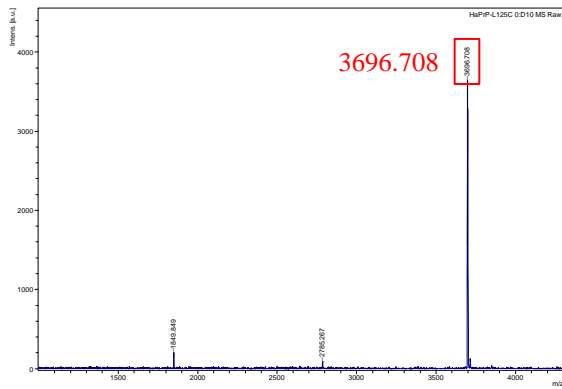
(F) M129C (crude)
(Theoretical molecular mass: 3677.644 Da)

52
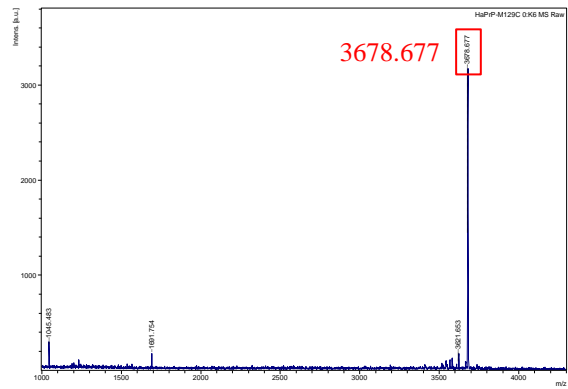
(G) M134C
(Theoretical molecular mass: 3677.644 Da)
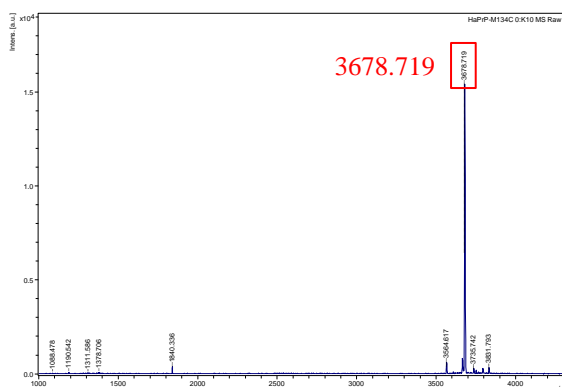
(H) M138C (crude + purified)
(Theoretical molecular mass: 3677.644 Da)
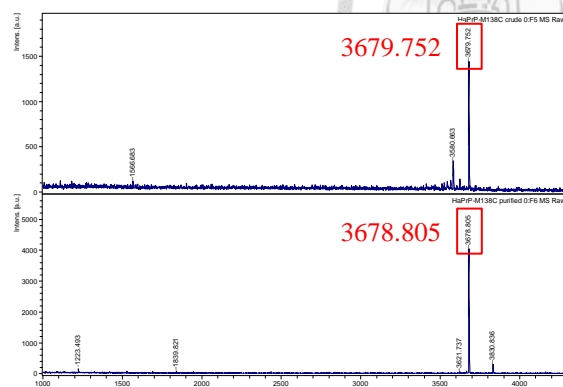
Figure 3.2 MS spectra of purified HaPrP(108-144) peptides obtained by MALDI-TOF/MS.

The actual molecular mass of the peptides were quite matched with their theoretical mass, with 1 Dalton more than the theoretical average mass. The spectrum of M129C was obtained from analysis of the crude peptide instead of the purified one. The spectra of M138C are juxtaposed since the spectra of crude peptide (upper part) and purified peptide (lower part) were drafted on the same graph.

The differences of 1 Dalton between the actual and theoretical molecular mass was due to the ionization of the peptide sample caused by energy transfer from the laser-treated matrix. In addition, the purity of the purified peptides was obviously better than the one of the crude peptides, proving that the efficiency of RP-HPLC purification was good enough.

53

3.2 MTSSL labeling, purification, and identification of peptides

3.2.1 Overview

The experiment of MTSSL spin labeling was performed after the seven purified mutant peptides were freeze-dried (lyophilized) by the lyophilizer, turning the peptides from aqueous transparent solution to cotton-like white powder. In form of solid powder, the peptide samples can be stored in -30°C freezer for months. To begin the labeling experiment, the peptides were first dissolved in water and quantified by UV-Visible spectrophotometer to determine their values of concentration based on the absorbance at 280 nm. According to Beer-Lambert Law ($A = \varepsilon \times b \times c$), the molar concentration (c) of the peptides could be calculated from the absorbance (A), the wavelength-dependent molar attenuation coefficient (ε), and the path length (b). The molar attenuation coefficient for the absorbance at 280 nm for the wild-type peptide was determined to be 1490 $M^{-1}cm^{-1}$, and the one for the mutant peptide was 1615 $M^{-1}cm^{-1}$, based on the equation proposed by previous studies (Nick, Felix et al. 1995). The concentration of the peptides was further adjusted to ~300 μM for labeling reaction.

The peptide solution was mixed with equal volume of 50 mM MOPS buffer (pH 6.5) and certain amounts of 126 mM MTSSL stock solution (in DMSO), making the final molar ratio of cysteine to MTSSL 1:4. Compared to the spin labeling protocol of full-length mouse prion mutant protein (Yang, Lo et al. 2015), our peptides were relatively hydrophilic and could be dissolved only in water instead of DMSO, and the volume ratio of peptide solution to MOPS buffer was 1:1 instead of 4:6 in the mixture. Different concentration of MOPS buffer and molar ratio of cysteine to MTSSL had been tested for labeling reaction. When using 60 mM MOPS buffer, the solution became more viscous and foamy and made it difficult to collect for follow-up purification. As

54

for the molar ratio of cysteine to MTSSL, once it was reduced to 1:3 or lower, the purity of labeling became worse as the portion of unlabeled peptides increased based on the analysis of MALDI-TOF/MS (data not shown). Usage of higher molar ratio had also been reported for better efficiency of labeling reaction (Cobb, Sönnichsen et al. 2007).

After the mixture of peptide solution, MOPS buffer and MTSSL stock solution was prepared, it was incubated on rotator in speed of ~30 rpm for ~10 hours at room temperature in dark. Shorter reaction time had been used along with higher molar ratio of MTSSL to cysteine (Cobb, Sönnichsen et al. 2007). Once the peptides were covalently bonded with the nitroxide R1 group from MTSSL, the samples should be kept from light in avoidance of jeopardizing the stability of the oxygen-centered free radicals.

3.2.2 HPLC purification of labeled peptides

Once the labeling reaction was over, the solution was brought to RP-HPLC purification with almost the same procedure as previously described. The biggest difference between the purification of unlabeled peptides and labeled peptides was that white peptide precipitate might be present after spin labeling. Since the precipitate was not homogenously distributed in the solution, it caused troubles when purifying with autosampler. Many kinds of solvents had been tested for dissolution of the precipitate, including 30% acetonitrile in water, DMSO and even hexafluoro-2-propanol (HFIP), but the precipitate exhibited poor solubility among most of them. Based on the observation that the column pressure did not rise highly even after the solution with precipitate was injected into HPLC, it was assumed that the precipitate could be dissolved in certain ratio of A buffer and B buffer mixture. The ratio was calculated to

55

be 34.5% B buffer in A buffer, and the precipitate truly exhibited better solubility in this ratio of mixture. Thus, once the precipitate appeared, the solution would be centrifuged to collect the precipitate, and the pellet would be resuspended and dissolved in 34.5% B buffer in A buffer.
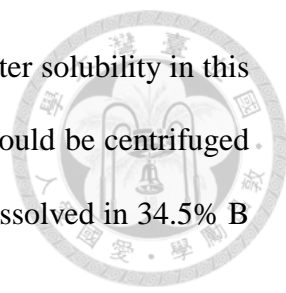
All of the labeled samples were purified with three kinds of gradients including 20-48%, 30-60%, and 24-45% B buffer, and the products eluted out at approximately the same range of retention time respectively, indicating that their properties inside the HPLC column were quite similar (Figure 3.3).

(A) A113R1   (Elution at 33.6%)   **(B) A118R1**   (Elution at 33.3%)

(C) V121R1   (Elution at 32.2%)   **(D) L125R1**   (Elution at 33.0%)

56

(E) M129R1   (Elution at 34.1%)   **(F) M134R1**   (Elution at 34.1%)

(G) M138R1   (Elution at 34.0%)
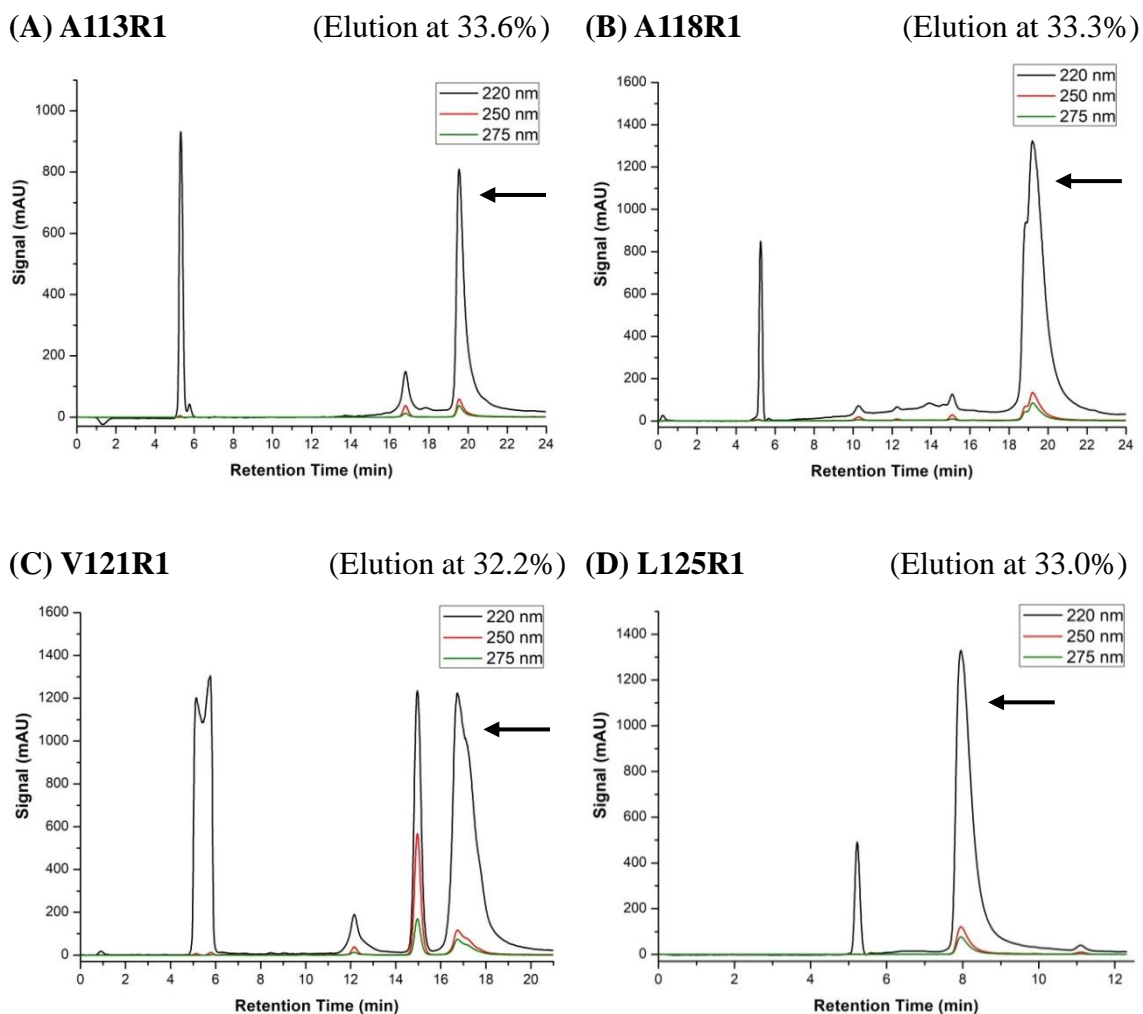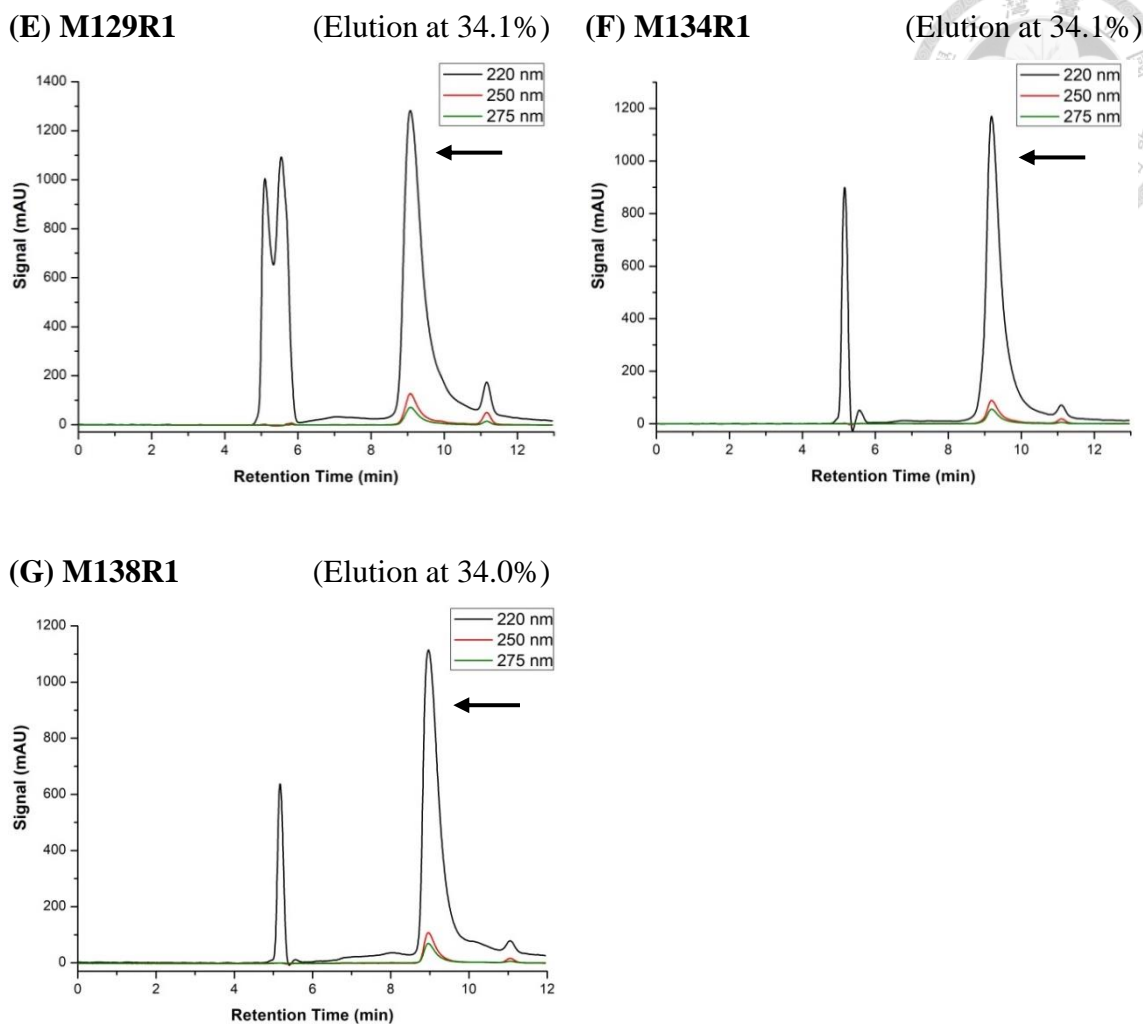
Figure 3.3 HPLC chromatograms showing the purification of spin-labeled HaPrP(108-144) peptides.

All of the peptides were purified with a C18 column. Samples of **(A)** A113R1 and **(B)** A118R1 were purified in the linear gradient of 20-48% B buffer, and **(C)** V121R1 was purified with 24-45% B buffer, with **(D)** L125R1, **(E)** M129R1, **(F)** M134R1, and **(G)** M134C purified with 30-60% B buffer. All of the sample purification was performed with the retention time of 30 minutes. The wavelengths of UV absorbance were set to be 220 nm, 250 nm, and 275 nm for detection of total substances, MTSSL labels and tyrosine-containing peptides respectively. The solid arrows indicated the collected peaks of the labeled peptides respectively. The solvent peaks appeared at approximately 5 minutes among all of the chromatograms.

In the chromatograms above, two merged solvent peaks (including the peaks of acetonitrile/water and MOPS) were apparent when the solution was directly sent for

57

HPLC purification, excluding precedent centrifugation.

From the chromatograms above, it is obvious to see that all of the samples eluted within the same range of gradient around 32-34% B buffer, showing that different sites of spin labeling on mutant cysteine residue did not cause significant variation. However, compared to the previous results of unlabeled peptide purification, the gradient of elution had increased from 27-29% to 32-34% B buffer. In addition to the increase of molecular mass, there might be other changes in the properties to which the spin labeling had brought the peptides. By the way, wild-type peptide was not labeled with MTSSL because it did not include cysteine residue mutation.

To make sure that the supernatant did not include extra labeled peptides after centrifugation, the supernatant was sent for the same procedure of HPLC purification. Besides, supernatant from the solution which was put quiescently after spin labeling was sent for purification for content check as well.

58

(A) Supernatant from quiescent solution   **(B) Supernatant from centrifuged solution**
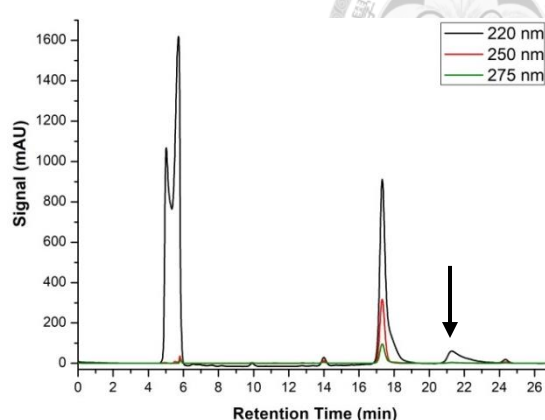
Figure 3.4 HPLC chromatograms showing the purification of supernatant from solutions of different treatments.
Supernatant from **(A)** quiescent solution of L125R1 and **(B)** solution of A113R1 after centrifugation were purified in the linear gradient of 30-60% and 20-48% B buffer respectively. Both of the purification was performed with the retention time of 30 minutes. The wavelengths of UV absorbance were set to be 220 nm, 250 nm, and 275 nm. The solid arrows indicated the peaks of the remnant labeled peptides respectively.

From the chromatograms above, it can be seen that most of the desired peptide products did exist in the white precipitate instead of the transparent supernatant, and that the treatment of centrifugation could help collect the peptides in a significantly effective way. To know the amount or percentage of the remnant peptides, both of the chromatograms should be compared to their own chromatograms of spin-labeled peptide purification, and the amount of initial injection volume should be also taken into consideration.

3.2.3 Identification of labeled peptides

After the elutes were collected in 50-mL Falcon tubes, 10 μL aliquot of the samples were taken out and sent for MALDI-TOF mass spectrometry analysis conducted by Ms.

59

His-Lin Cheng in Mass Spectrometer Facility at the Institute of Molecular Biology, Academia Sinica (Figure 3.5).
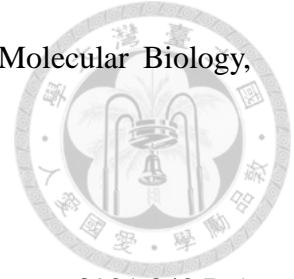
(A) A113R1
(Theoretical molecular mass: 3921.842 Da)
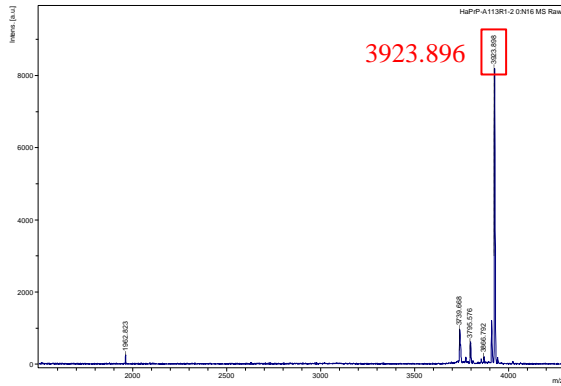
(B) A118R1
(Theoretical molecular mass: 3921.842 Da)
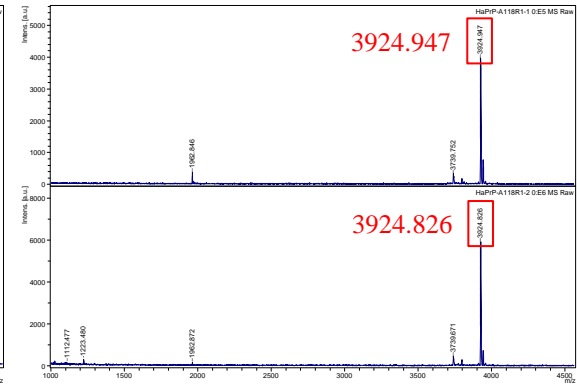
(C) V121R1
(Theoretical molecular mass: 3893.810 Da)
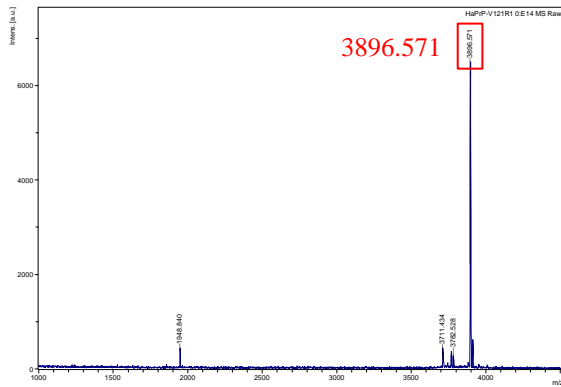
(D) L125R1
(Theoretical molecular mass: 3879.795 Da)
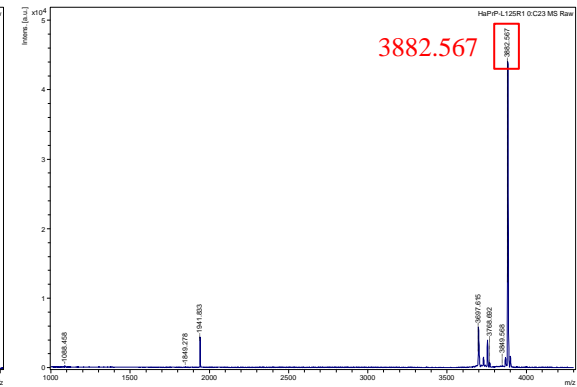
(E) M129R1
(Theoretical molecular mass: 3861.838 Da)
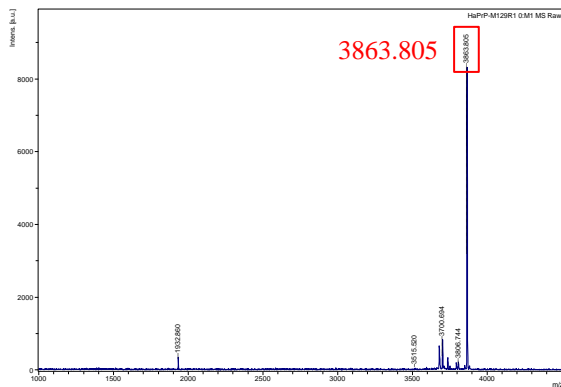
(F) M134R1
(Theoretical molecular mass: 3861.838 Da)

60
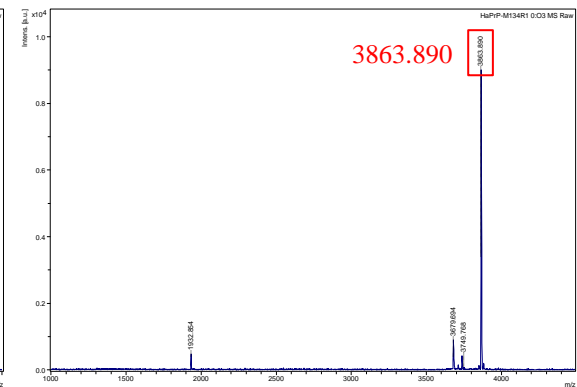
(G) M138R1
(Theoretical molecular mass: 3861.838 Da)
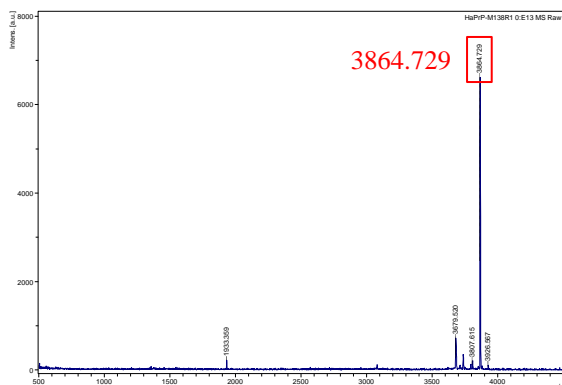
Figure 3.5 MS spectra of purified spin-labeled HaPrP(108-144) peptides obtained by MALDI-TOF/MS.
The actual molecular mass of the peptides were quite matched with their theoretical mass, with 2-3 Dalton more than the theoretical average mass. The spectra of A118R1 were based on different elutes from the same peak, and they both ultimately matched with the theoretical mass.
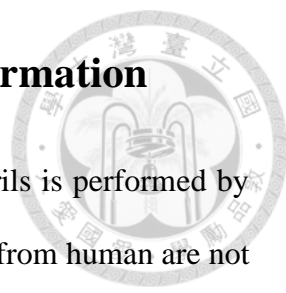
The consistent differences of 2-3 Dalton between the actual and theoretical molecular mass appeared to be based on reasons with the ionization of the unlabeled peptides and calibration issues. In addition, the purity of many of the mutant peptides might be concerned that small portions of unlabeled peptides were included in the collected elute. This issue might be improved by increasing the molar ratio of MTSSL to cysteine in the labeling reaction.

After the identity and purity of the seven labeled mutant peptides were checked, the peptides were again freeze-dried by the lyophilizer and stored in -30°C freezer for the following experiments of fibril formation.

61

Chapter 4   Results (II): Amyloid Fibril Formation

In this thesis, the structural study of hamster prion peptide fibrils is performed by first preparing the peptide fibrils *in vitro*. Since the samples of PrP^{Sc} from human are not easy to obtain and usually arouse safety concerns, the system of PrP fibril formation *in vitro* had been established as a more practical way to observe amyloid fibril growth. The similarities between structures of fibrils formed *in vitro* and *in vivo* had also been linked to their capabilities of transmission and thus infectivity. In terms of infectivity, both of the recombinant PrP from hamster and mouse had been reported to be able to use for *de novo* generation of infectious prions *in vitro* by different means, including incubation in partially denaturing conditions followed by annealing technique and multiple rounds of protein misfolding cyclic amplification (PMCA) (Makarava, Kovacs et al. 2010, Wang, Wang et al. 2010). Based on the fact that both PrP^{Sc} and fibril formed from recombinant monomers are rich in β-structure, this had given an implication that the fibrils formed *in vitro* might be used to simulate the structures of the infectious agents of PrP *in vivo*.

In addition to spontaneously formed peptide fibrils, seeding is also an important mechanism to accelerate the formation of amyloid. In the pathogenesis of transmissible spongiform encephalopathy (TSE), it is a significant feature that the native form of PrP^{C} can be transformed into the abnormal PrP^{Sc} isoform in a self-induced way by the presence of PrP^{Sc} fragments. Based on the proposal that the conversion from monomeric to fibrillary form is characterized by the model of nucleation-dependent polymerization (Kundu, Maiti et al. 2003), it is also assumed that the seeding assay performed *in vitro* can be used to clarify the detailed mechanism of PrP self-propagation *in vivo*. Seeding assay can be also a powerful tool in investigating the species barrier in mammalian prion propagation (Lee and Chen 2007), in which the PrP^{Sc} agent could cross the

63

species to be infectious but the efficiencies are quite variable in different species. This phenomenon is mainly due to the differences of amino acid sequences between the species.
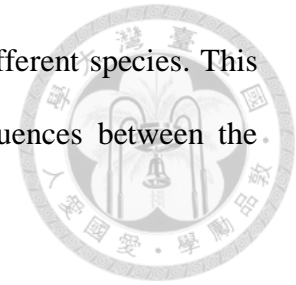
Before the seeding assay, it is necessary to observe the formation of the amyloid fibrils spontaneously first. In that way, the natural condition for fibrillization could be investigated, and then seeds would be prepared for follow-up seeded fibril formation experiments.

4.1   Spontaneous fibril formation of HaPrP peptides

All of the peptide stock solutions were prepared by dissolving the spin-labeled peptide powder in water and quantified by UV-Visible spectrophotometer to be at least 200 μM. This step is important since the rate of fibril formation is dependent on the peptide concentration. The peptide stock solution was then mixed with equal volume of fibril formation buffer and incubated in amber-colored Eppendorf tubes quiescently.

Three kinds of fibril formation conditions were tested for spontaneous fibril formation to determine the relative efficiencies first, including 20 mM sodium acetate (NaOAc) with 140 mM NaCl in 25°C (pH 3.7) (Chatterjee, Lee et al. 2013), 25 mM sodium acetate with 175 mM NaCl in 25°C (pH 3.6) (Chung-Yu Lee's protocol), and 10 mM sodium phosphate with 396 mM NaCl and 0.01% NaN$_3$ in 37°C (pH 7.6) (Lin, Chao et al. 2010) (Figure 4.1). The buffer of sodium acetate had been reported to be suitable for the growth of mouse prion protein and peptide fibrils but not for the hamster ones, and the sodium phosphate buffer had been previously used by Dr. Jerry Chun-Chung Chan's group and in Howard's thesis in our lab. The values of

64

concentration above were the final salt concentration after being mixed with the peptide stock solution, of which the concentration was 150 μM after dilution.
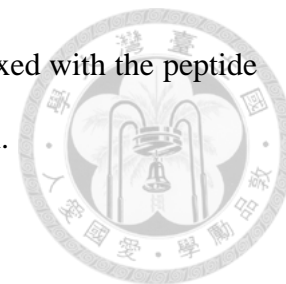
(A) 20 mM NaOAc
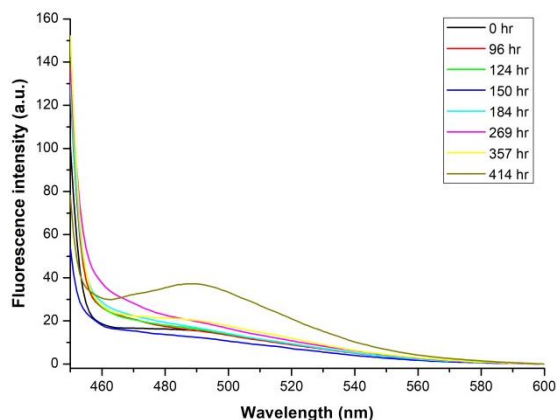
(B) 25 mM NaOAc
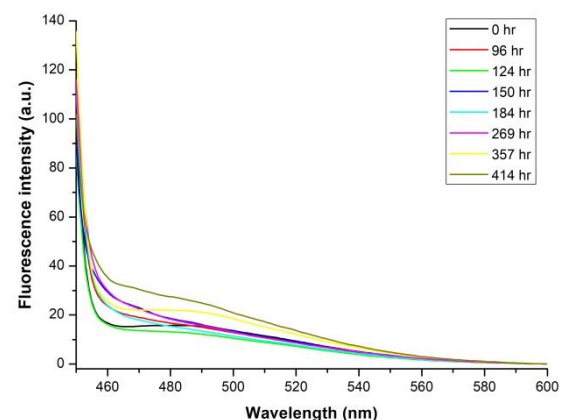
(C) 10 mM sodium phosphate
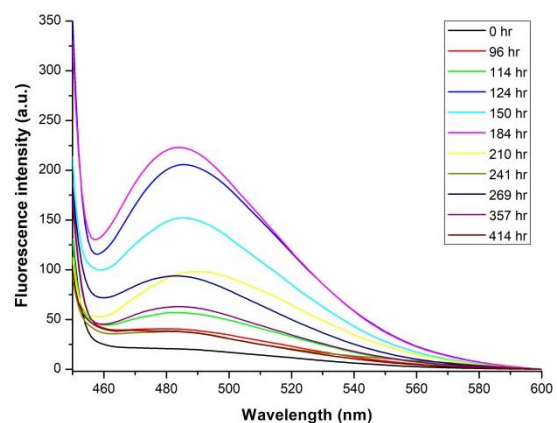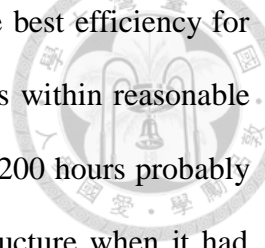
(D) Combined data at 487 nm
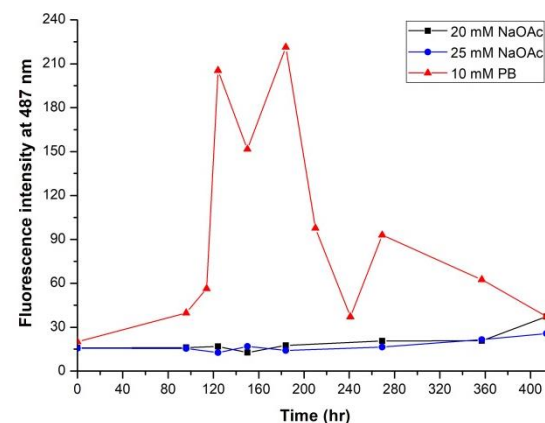
Figure 4.1 Condition-dependent spontaneous fibril formation of HaPrP(108-144) WT.

The conditions of **(A)** 20 mM NaOAc with 140 mM NaCl in 25℃ (pH 3.7), **(B)** 25 mM NaOAc with 175 mM NaCl in 25℃ (pH 3.6), and **(C)** 10 mM sodium phosphate with 396 mM NaCl and 0.01% NaN₃ in 37℃ (pH 7.6) were all tested for the optimal condition of spontaneous fibril formation. The values of peptide concentration in the sample were all diluted to 150 μM. **(D)** The kinetic curves showing values of emission intensity at 487 nm of the three samples were drafted together for comparison, and they were not calibrated by the water/FFB control. The values of fluorescence intensity at 600 nm were all adjusted to 0. The emission spectra were measured from 450 to 600 nm with the excitation at 442 nm. PB: phosphate buffer. FFB: fibril formation buffer.

It was found that the sodium phosphate buffer had brought the best efficiency for HaPrP peptides to form amyloid fibrils from hamster prion peptides within reasonable incubation period, though the intensity dropped significantly after ~200 hours probably due to the incapability of ThT insertion into the amyloid fibril structure when it had been formed in a too compact way. These peptides were assumed to be gradually polymerized probably based on this high salt concentration. Therefore, the sodium phosphate buffer, with the addition of NaCl salt and NaN_3 for antiseptic effects, were used throughout the following experiments for convenience of comparison. Compared to the fibril formation protocol of full-length mouse prion mutant protein (Yang, Lo et al. 2015), our peptides were dissolved only in water without any other denaturants such as guanidine hydrochloride (GdnHCl) or urea. In addition, our fibril formation buffer included only sodium salts without extra potassium salts such as potassium phosphate and potassium chloride.

For the observation of effective seeding assay, the fibril growth between spontaneous and seeded must be distinguished by different rate of fibril formation. It is assumed that the rate of seeded fibril formation would be higher than the one of spontaneous fibril formation based on the presence of seeds, which serve as the key factor in the nucleation process. Since the rate of fibril formation is dependent on the peptide concentration, the optimal lowest concentration for differentiating spontaneous and seeded fibril growth must be first determined. Thus, for each mutant peptide, the fibril formation experiments were carried out based on different values of concentration, with the highest one not exceeding 120 μM. The wild-type peptide was also tested with exactly the same procedure (Figure 4.2).

66

(A) WT

(B) WT

(C) A113R1

(D) A113R1
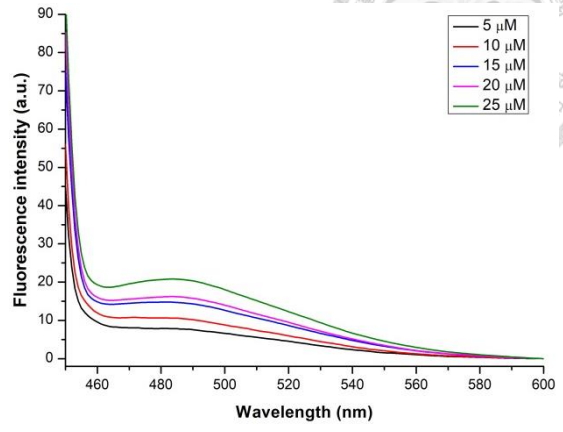
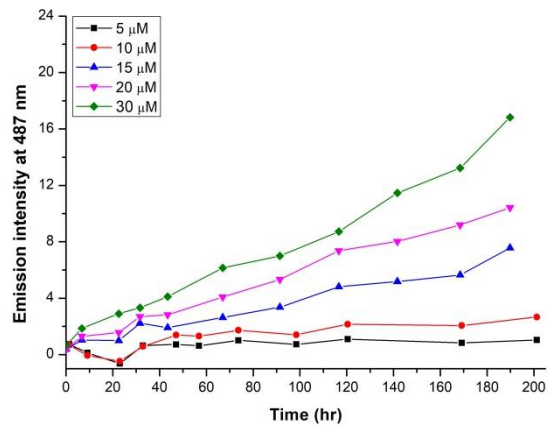**(E) A118R1**
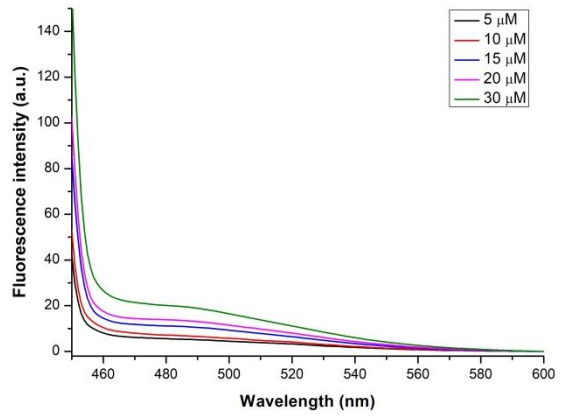
(F) A118R1

67
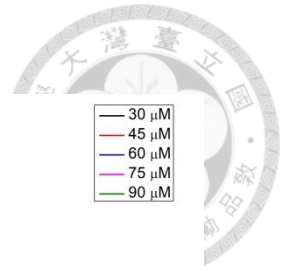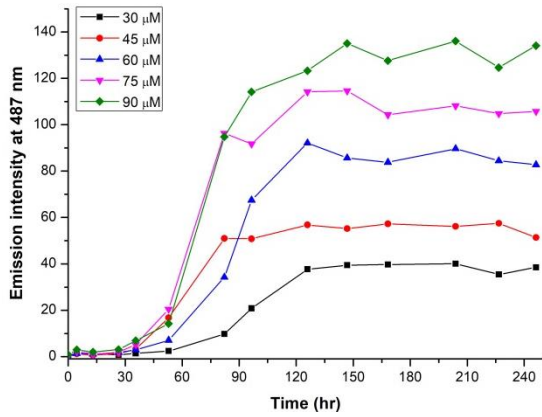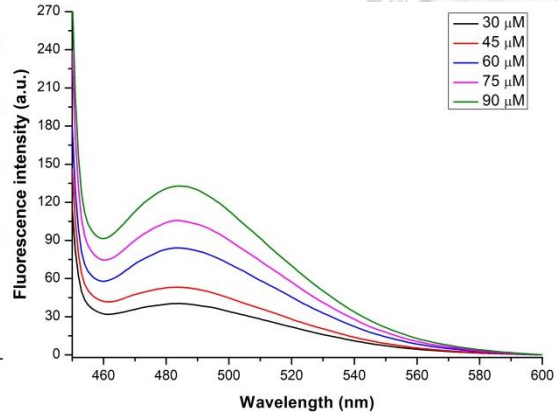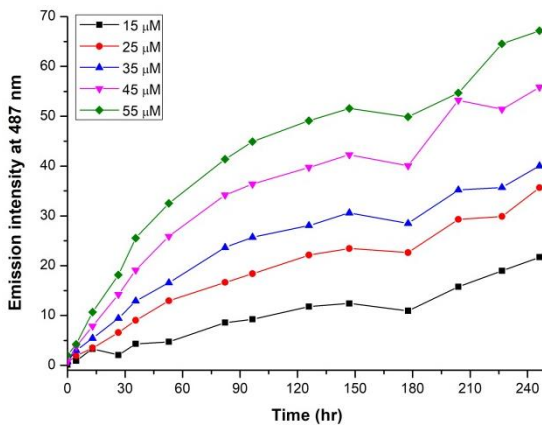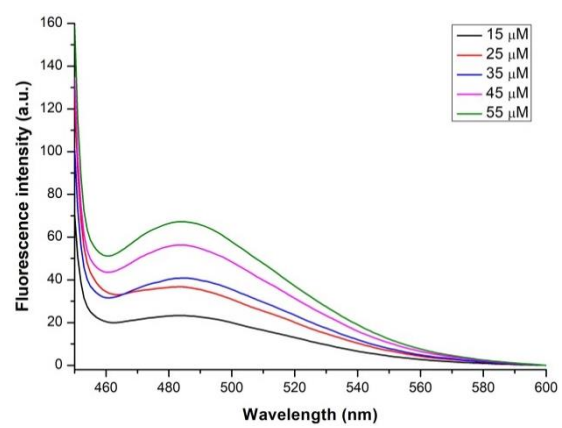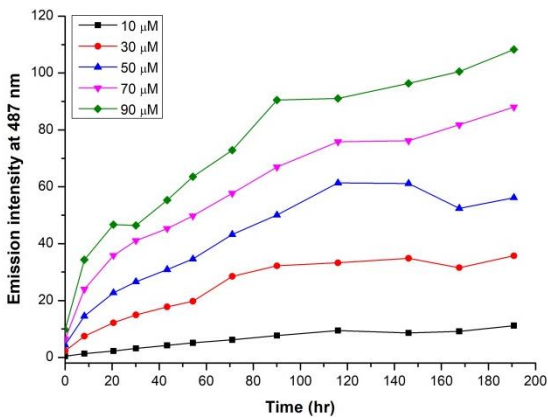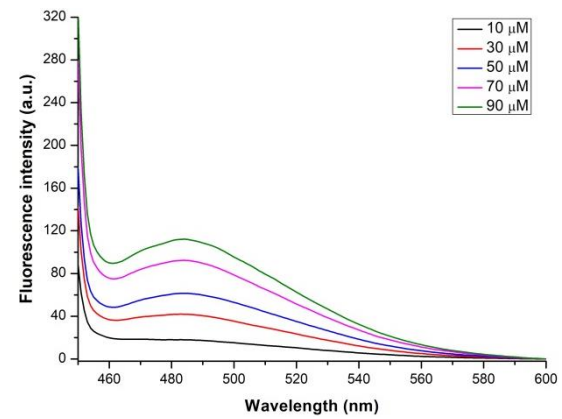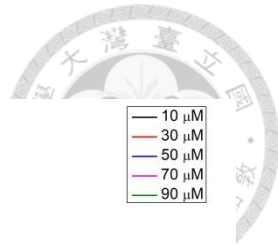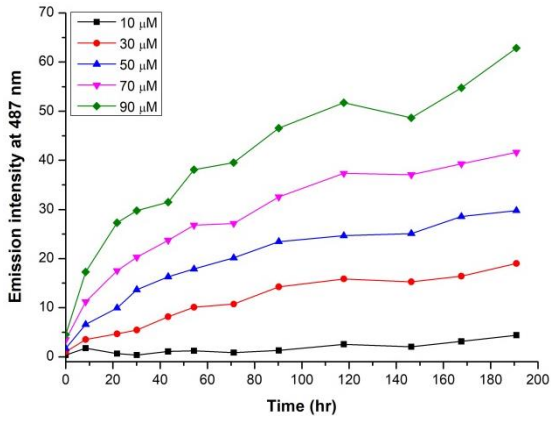
(G) V121R1

(H) V121R1

(I) L125R1

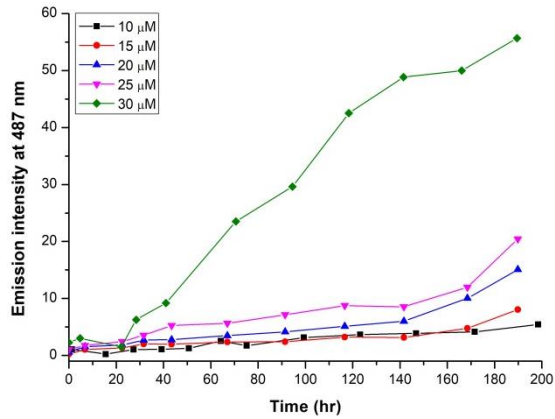**(J) L125R1**
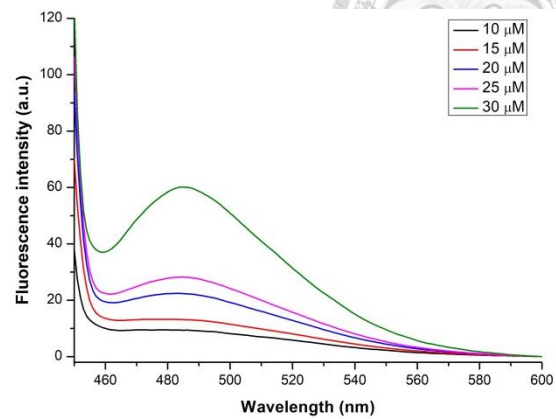
(K) M129R1

(L) M129R1

68
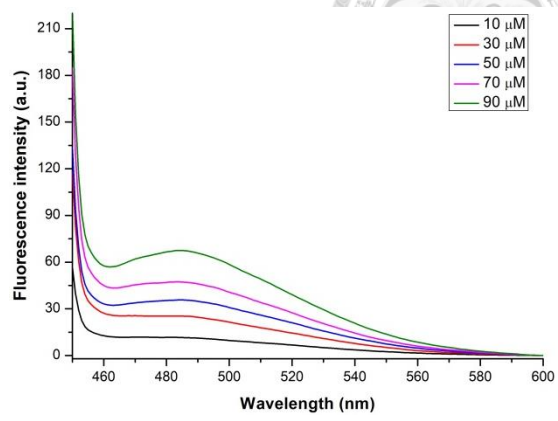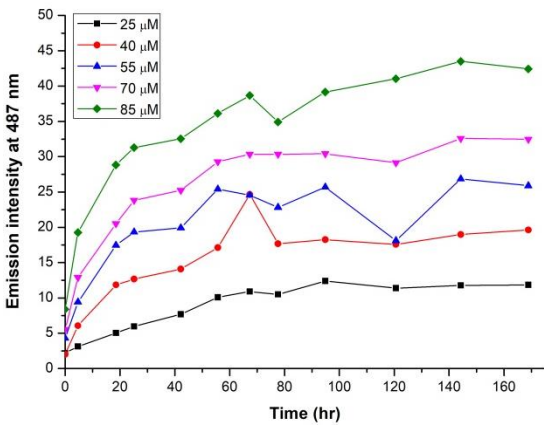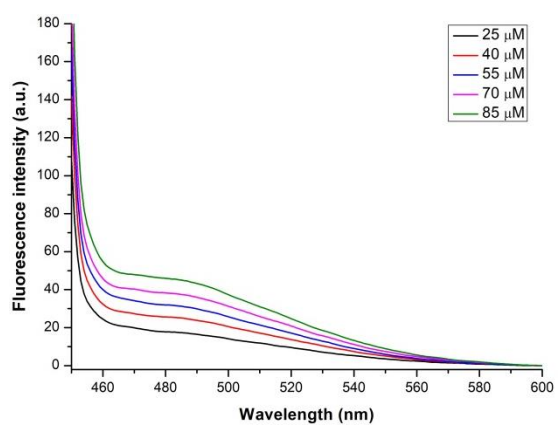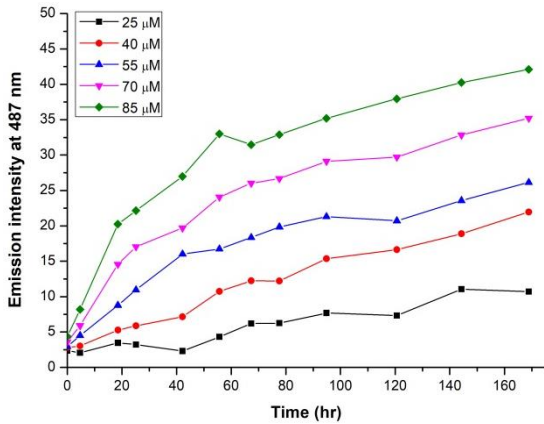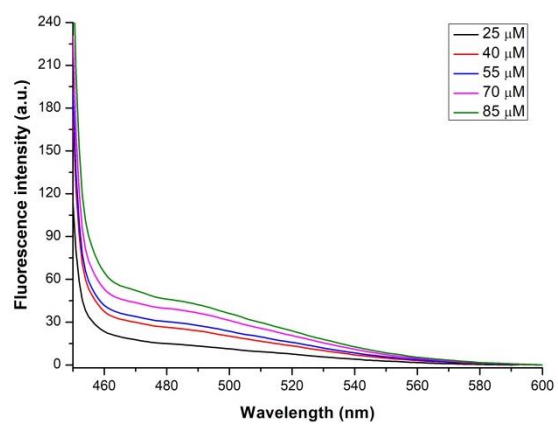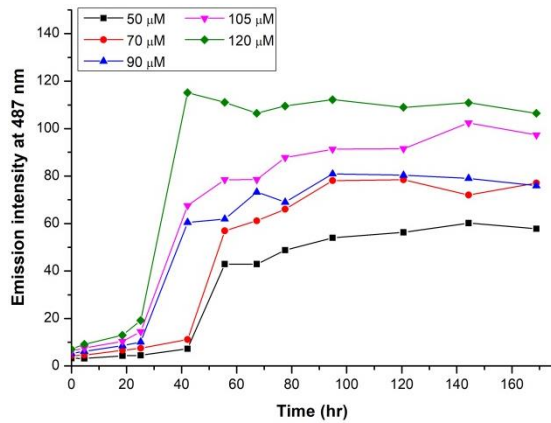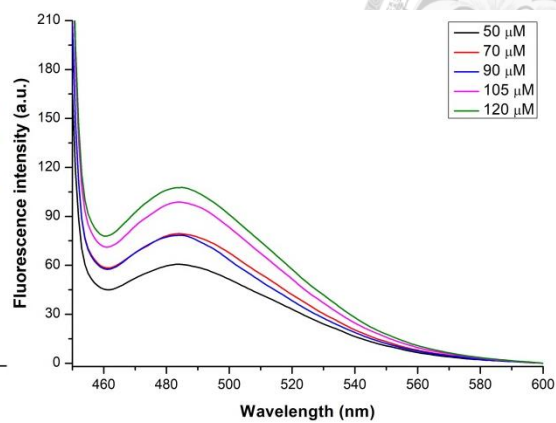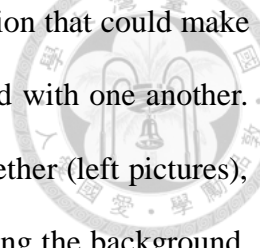
(M) M134R1
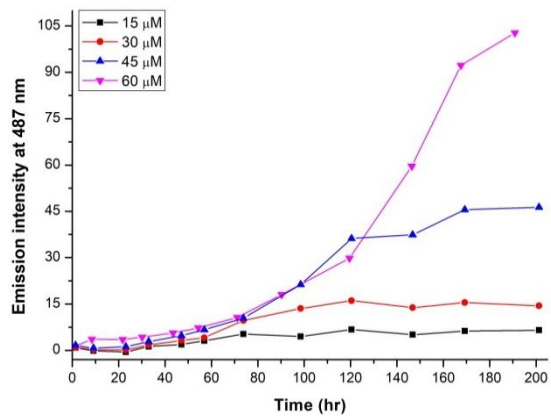
(N) M134R1
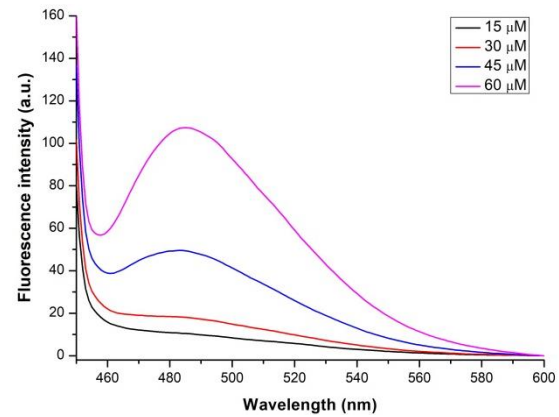
(O) M138R1

(P) M138R1

Figure 4.2 Concentration-dependent spontaneous fibril formation of HaPrP(108-144) peptides.

The peptides of **(A)** WT, **(C)** A113R1, **(E)** A118R1, **(G)** V121R1, **(I)** L125R1, **(K)** M129R1, **(M)** M134R1, and **(O)** M138R1 were tested for the optimal concentration of spontaneous fibril formation, and they had all been calibrated by the water/FFB control. The kinetic curves showing values of emission intensity at 487 nm between different values of concentration of the all samples were drafted together for comparison. The fluorescence spectra obtained from the last data point were drafted together between different values of concentration as from **(B)** to **(P)**. The values of fluorescence intensity at 600 nm were all adjusted to 0. The emission spectra were measured from 450 to 600 nm with the excitation at 442 nm, and the slit widths were set to be 5 nm and 10 nm respectively.

69

In the process of data analysis, there were two kinds of calibration that could make the spectra measured from different time points able to be compared with one another. For the values of emission intensity at 487 nm that were drafted together (left pictures), the values had been subtracted by the water/FFB control for excluding the background. For the whole fluorescence spectra from 450 to 600 nm (right pictures), the values of fluorescence intensity at 600 nm were all adjusted to 0 since no fluorescence intensity was supposed to be detected at this wavelength. The original values of this wavelength usually vary from time to time with a little gap from 0, and the adjustment would help to compare different spectra in style of more fidelity. Note that since these two ways of calibration were not the same, values of fluorescence intensity from the same sample could not be compared in quantity between left and right pictures and could only be compared within the same picture.

From the fluorescence spectra above, it was obvious to see that the fibril growth between wild-type and different mutant peptides were significantly different. The curves of wild-type peptide exhibited the feature of sigmoidal shape, proving the features of lag time and elongation phase in the nucleation-dependent polymerization model (Figure 1.5). However, the curves of many mutant peptides showed gradual increase in fluorescence intensity and didn't exhibit significant lag time except for the mutant M134R1. In some samples of higher concentration, the curve exhibited hyperbolic shape, featuring immediate increase of fluorescence intensity at the start of incubation. This might imply that the spin labeling on the prion peptide might have changed some of the original structural features, turning the fibrils to grow in a faster or slower way.

The fluorescence spectra of each mutant in its highest concentration were also put together to show the change of intensity through time, and this helped to visualize the

70

sudden increase in the intensity of 487 nm in some of the samples, such as WT, M134R1, and M138R1 (Figure 4.3).
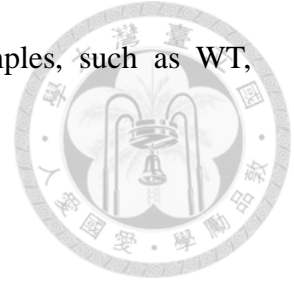
(A) WT_90 µM
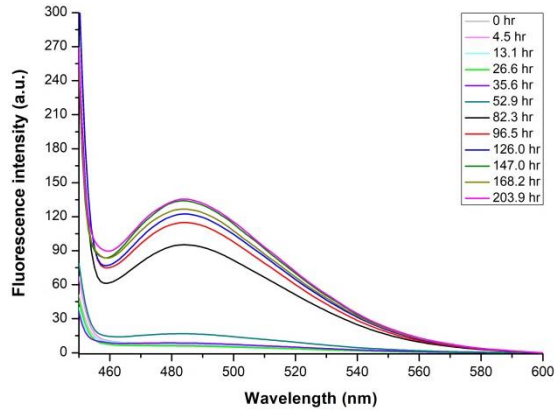
(B) A113R1_55 µM

(C) A118R1_90 µM

(D) V121R1_90 µM

(E) L125R1_85 µM

(F) M129R1_85 µM

71
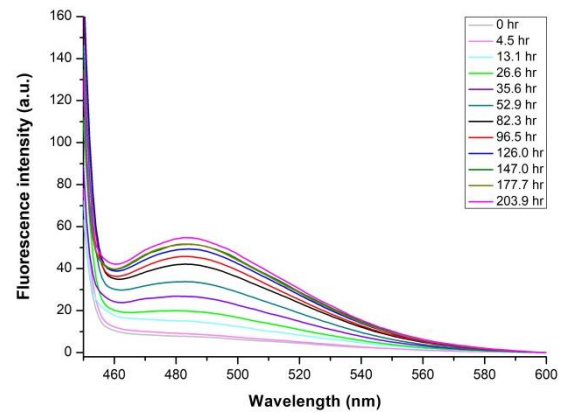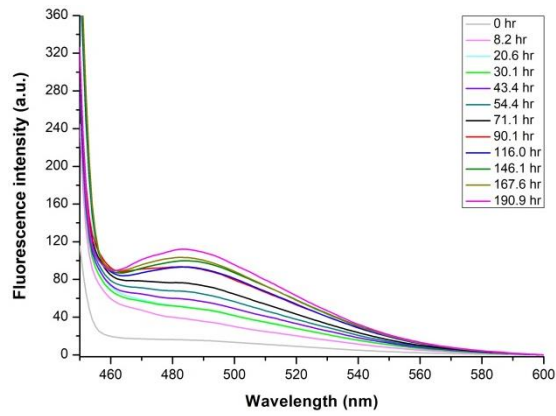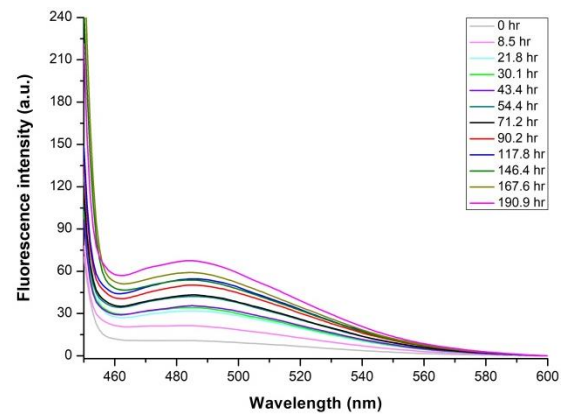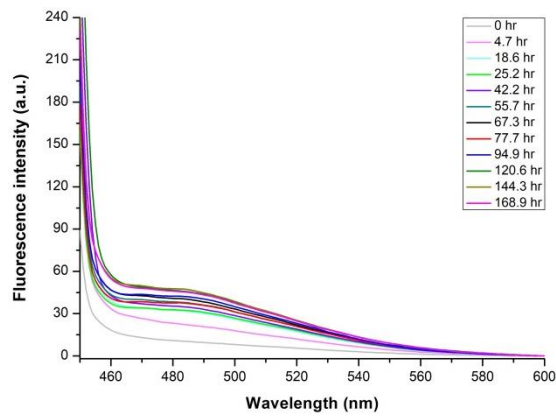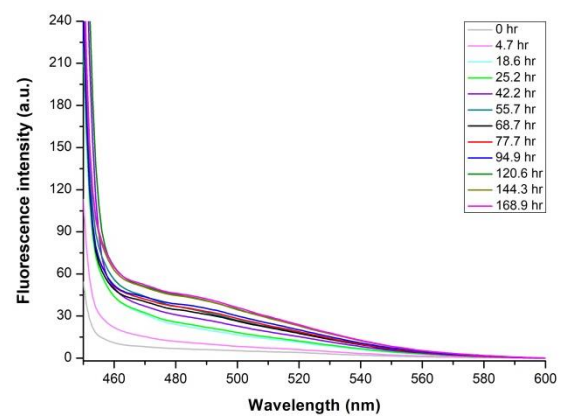
(G) M134R1_120 µM
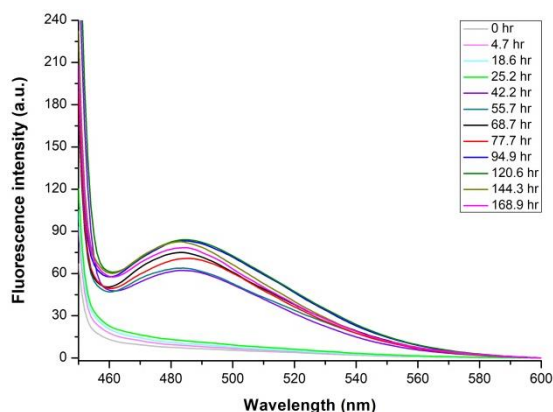
(H) M138R1_60 µM
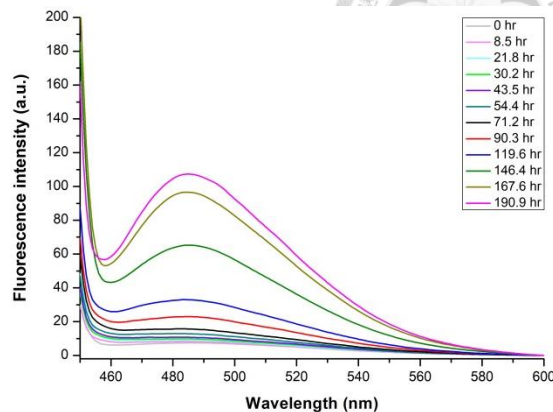
Figure 4.3 Fluorescence spectra of spontaneous fibril formation of HaPrP(108-144) peptides in their highest concentration.

The fluorescence spectra of the peptides listed from **(A)** to **(H)** were drafted for comparison in their respective highest concentration. The emission spectra were measured from 450 to 600 nm with the excitation at 442 nm, with the slit widths set to be 5 and 10 nm.

Among some of the mutant peptides, higher values of concentration had also been tested for spontaneous fibril formation, and they all showed rapid growth and were not suitable for our desired lowest concentration (Figure A.2).

To further examine the effects of subtler differences in peptide concentration on spontaneous fibril formation, sets of lower concentration had been used for test in most of the peptides, aiming to find the optimal lowest values for distinguishing spontaneous and seeded fibril formation in each peptide (Figure 4.4).

72
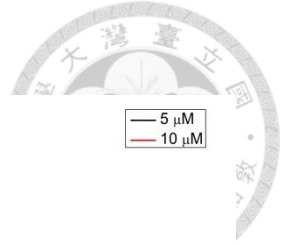
(A) WT
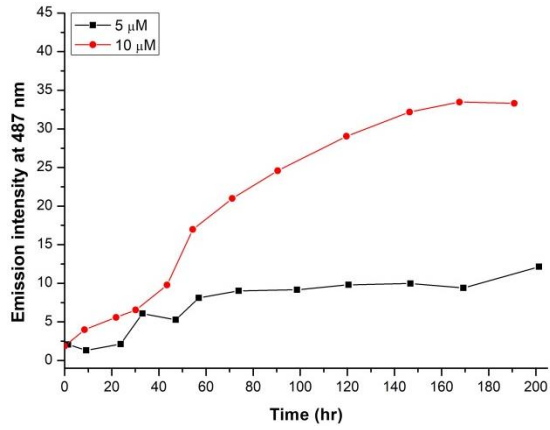
(B) WT
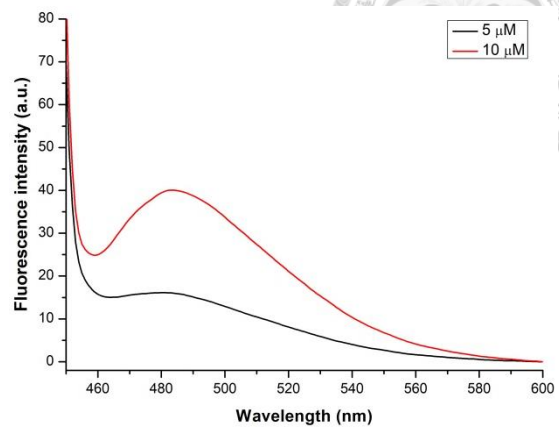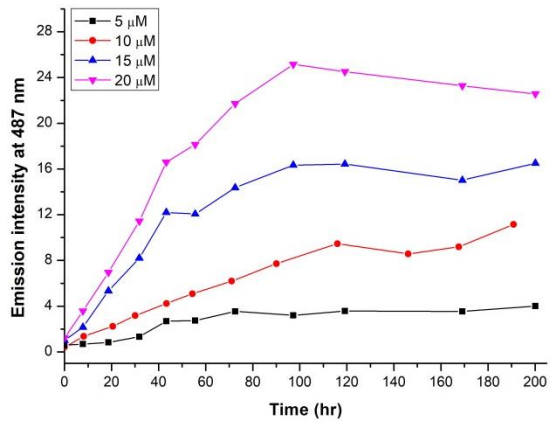
(C) A118R1

(D) A118R1

(E) V121R1

(F) V121R1

73
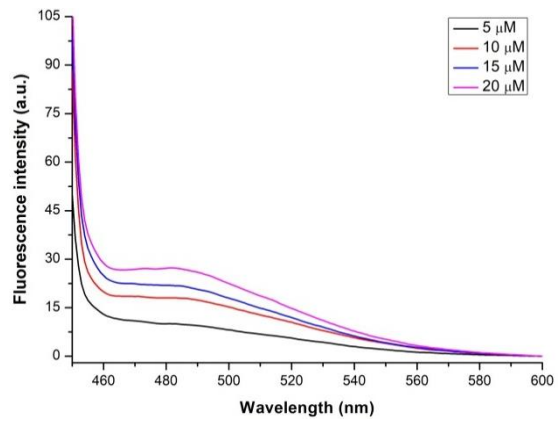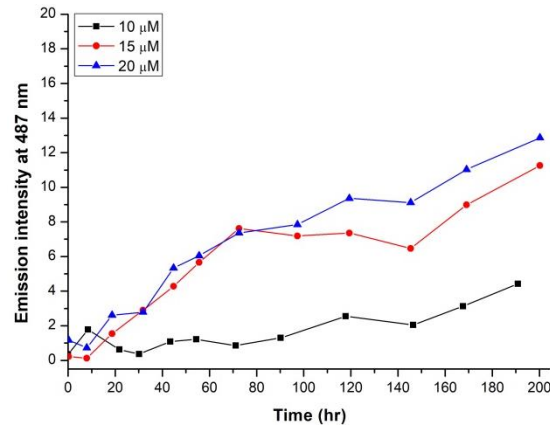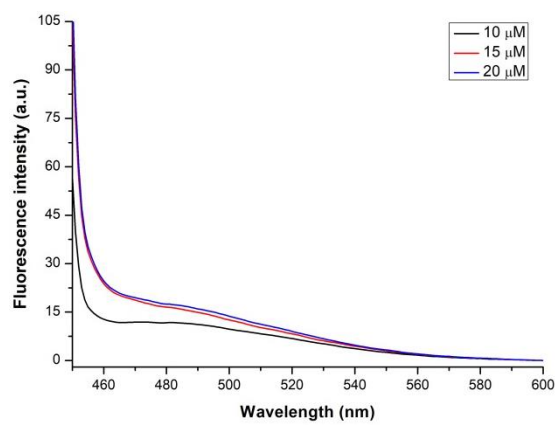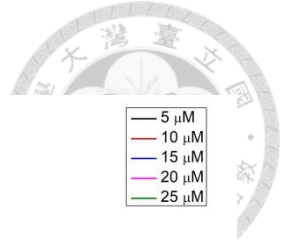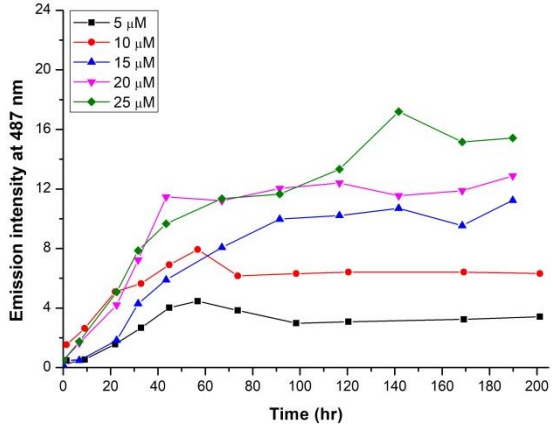
(G) L125R1

(H) L125R1

(I) M129R1

(J) M129R1

(K) M134R1

(L) M134R1

Figure 4.4 Lower concentration tests of spontaneous fibril formation of HaPrP(108-144) peptides.

The peptides of **(A)** WT, **(C)** A118R1, **(E)** V121R1, **(G)** L125R1, **(I)** M129R1, and **(K)** M134R1 were tested for the optimal concentration of spontaneous fibril formation. The fluorescence spectra obtained from the last data points were drafted together between different values of concentration as from **(B)** to **(L)**. The lowest optimal concentration of mutant A113R1 and M138R1 had been determined and was not tested for lower concentration.

Furthermore, the spectra were compared between different mutant and wild-type peptides based on roughly the same values of peptide concentration including 10 and 15 μM (Figure 4.5). The fluorescence intensity of wild-type peptide significantly increased faster than the other mutants through the time. Within the mutants, the fibrils of A113R1 and A118R1 grew a little faster than other mutants, and M129R1 showed the least and nearly no noticeable growth.

75

(A)

(B)
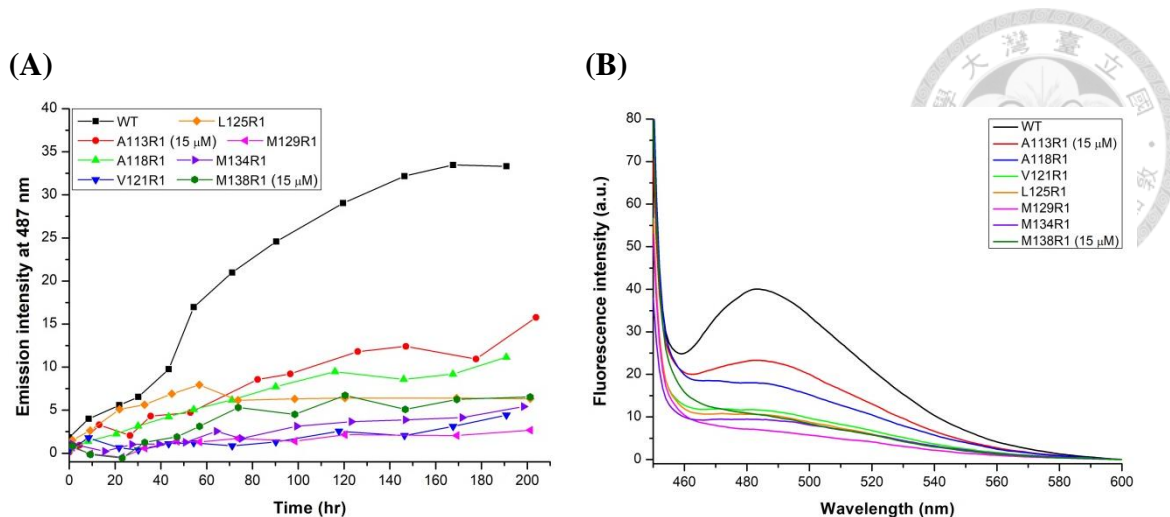
Figure 4.5 Comparison of spontaneous fibril formation between different HaPrP(108-144) peptides.

The fluorescence spectra from spontaneous fibril growth of the peptides listed above were organized and compared for their relative rate of growth. The kinetic curves showing values of emission intensity at 487 nm of the samples were drafted together for comparison as **(A)**. The fluorescence spectra obtained from the last data point were drafted together between different values of concentration as **(B)**. All values of the peptide concentration were 10 μM, except for A113R1 and M138R1 being 15 μM.

The optimal lowest values of concentration for distinguishing spontaneous and seeded fibril formation in each peptide were listed in Table 4.1 for comparison. From the table we can see that the values fell in the range of 5-15 μM, showing no big differences between different samples.

Table 4.1 Optimal lowest values of concentration for distinguishing spontaneous and seeded fibril formation in each peptide.

Samples	WT	A113	A118	V121	L125	M129	M134	M138
Concentration (μM)	5	15	5	10	5	5	10	15

After all of the peptides were tested in the spontaneous fibril formation, they were next tested with seeding assay, and changes in the rate of fibril growth were expected.

76

4.2 Seeded fibril formation of HaPrP peptides

In order to better understand the amyloid core of hamster prion peptide, the seeded fibril formation of prion peptides were carried out by using seeding assay upon the previous procedures of spontaneous fibril formation. It's important to note that mutant peptides might form fibrils of different structures compared to the wild-type peptide since they were mutated to cysteine and spin-labeled with an extra nitroxide group in their own residues of the sequence. With the presence of seeds, the fibril fragments formed of wild-type peptide, the mutant peptides could grow and elongate on the basis of the seeds, and the resulting fibril structures were assumed to bear more resemblance to the wild-type fibrils. This is an important concept throughout this study since this should make the resulting ESR data more convincing than the data from spontaneously formed fibrils.

The only difference between these two ways of fibril formation was the presence of seeds, and it is expected that the rate of seeded fibril formation would be higher than the one of spontaneous fibril formation based on the seeding effects. The fluorescence intensity values of the control of water mixed with fibril formation buffer and seed solution only, without the addition of peptides, were first measured and would both serve as the blanks for the calibration of spontaneous and seeded samples (Figure A.3). From the figure, the fluorescence intensity of seed solution remained in a steady level and didn't change much with the time, suggesting that this could be a good blank for calibrating the following seeded samples.

Before the seeding assay is performed with the optimal lowest concentration in Table 4.1, there was an issue about how much seeds should be used in the assay. In Howard's thesis, the amounts of seeds were used in various quantities based on both

sources of seeds (fibrils from protein or peptide) and targets of seeding (homologous or heterologous), ranging from about 200 to 4000 pmol. Since the peptide concentration used Howard's study was mostly higher than in this thesis, more amounts of seeds were considered to be used to compensate the lower concentration of peptide monomers.

The efficacy of seeding assay was tested and compared by adding different quantities of seeds in different mutant samples (Figure 4.6). The quantities were set to be fixed from 800 to 4500 pmol no matter how much the concentration of the peptide solution was.

(A) A113R1_15 μM
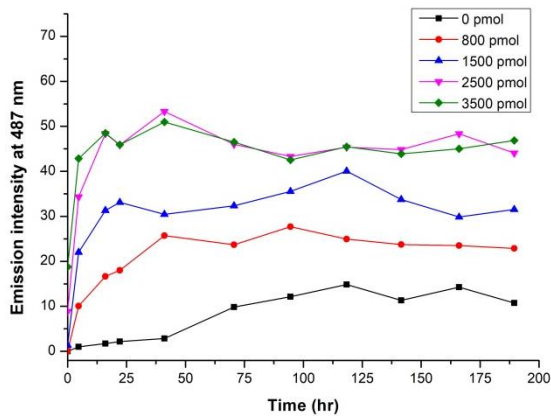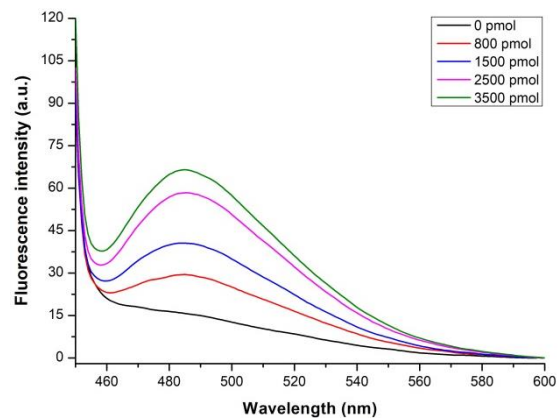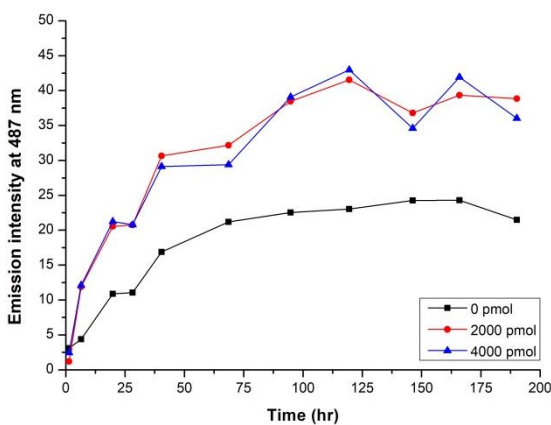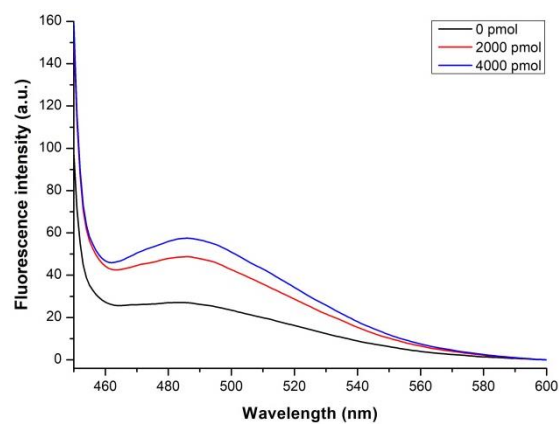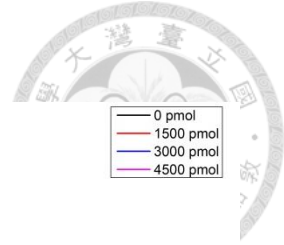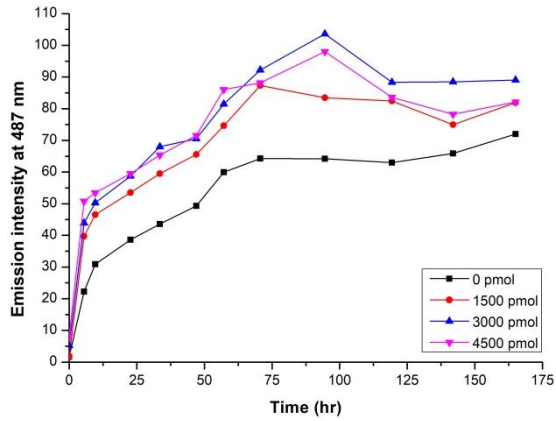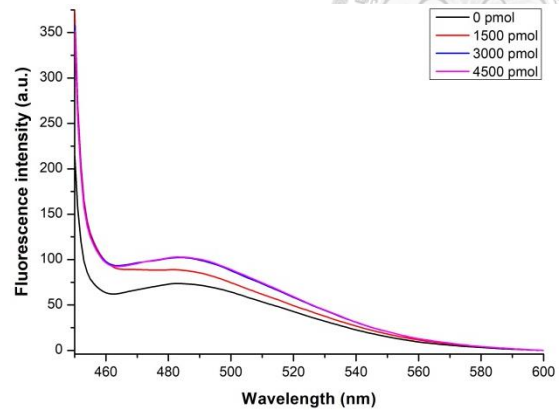
(B) A113R1_15 μM

(C) L125R1_40 μM

(D) L125R1_40 μM

78

(E) L125R1_105 μM

(F) L125R1_105 μM

(G) M129R1_40 μM

(H) M129R1_40 μM

(I) M129R1_110 μM

(J) M129R1_110 μM

79
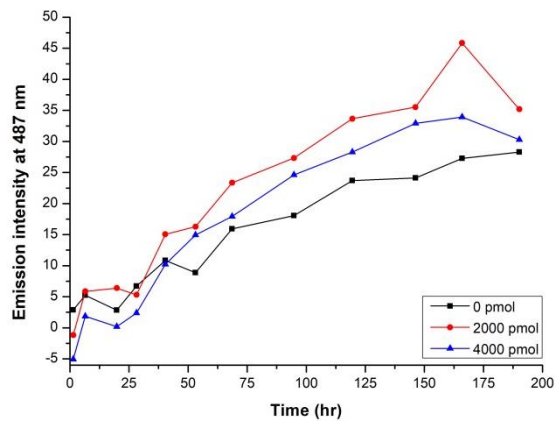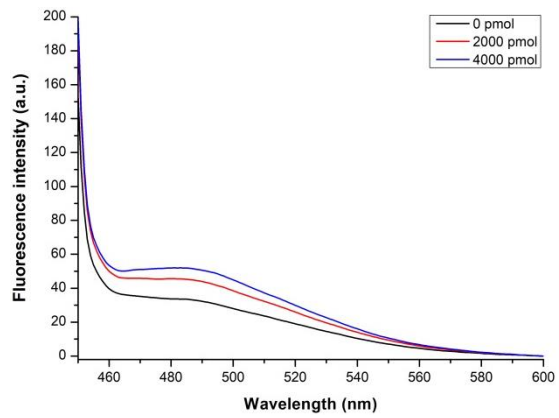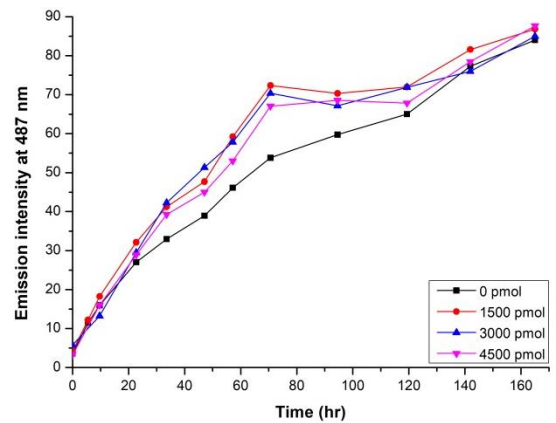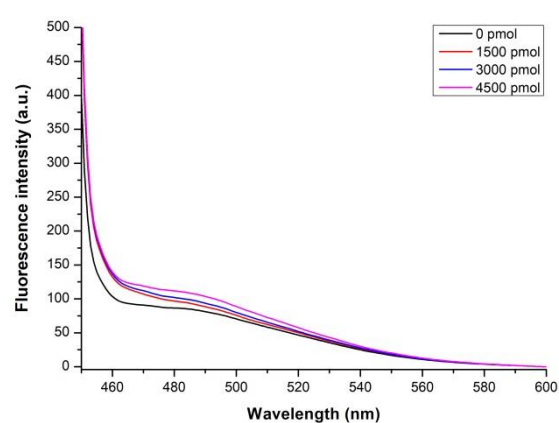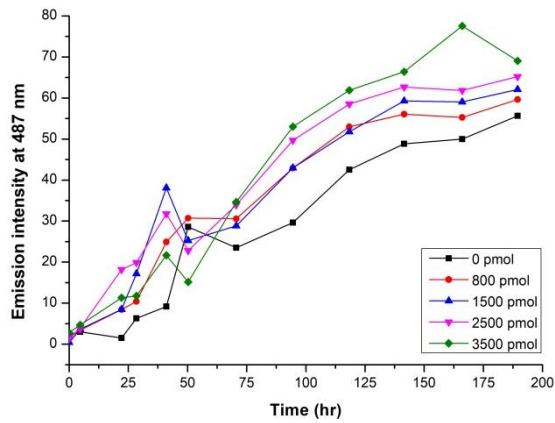
(K) M134R1_30 μM

(L) M134R1_30 μM
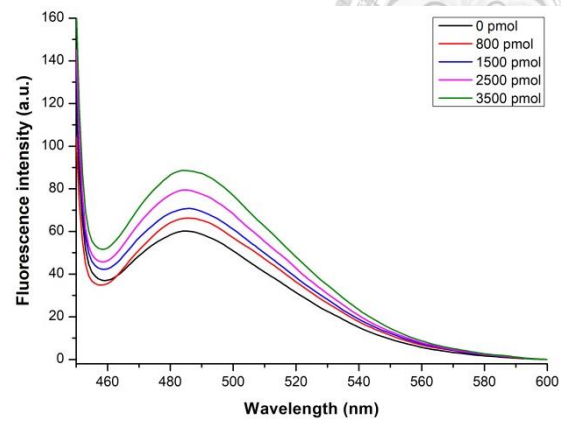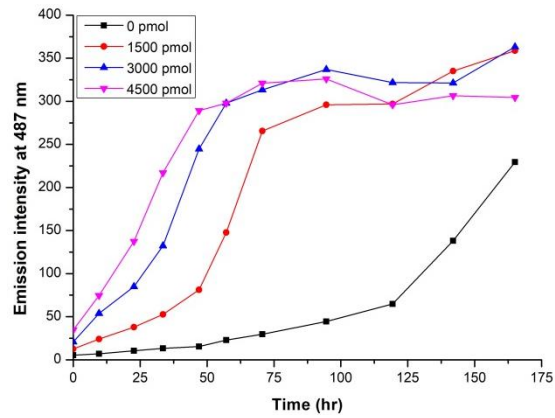
(M) M138R1_130 μM

(N) M138R1_130 μM
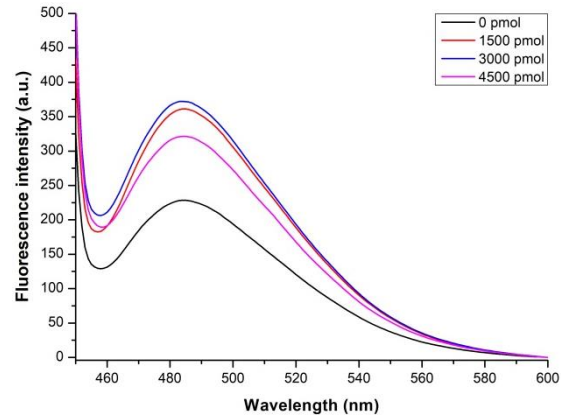
Figure 4.6 Seeded fibril formation of HaPrP(108-144) peptides with various concentration of seeds.

Three sets of seed quantities were used for testing the efficacy of seeding assay. Samples of **(A)** A113R1_15 μM and **(K)** M134R1_30 μM were tested with seed quantities of 0, 800, 1500, 2500, and 3500 pmol, and **(C)** L125R1_40 μM and **(G)** M129R1_40 μM were tested with seed quantities of 0, 2000, and 4000 pmol, with **(E)** L125R1_105 μM, **(I)** M129R1_110 μM, and **(M)** M138R1_130 μM being tested with seed quantities of 0, 1500, 3000, and 4500 pmol. The kinetic curves showing values of intensity at 487 nm had been calibrated by the controls of water/FFB and seed solution. The fluorescence spectra obtained from the last data points were drafted together between different quantities of seeds as from **(B)** to **(N)**. The emission spectra were measured from 450 to 600 nm with the excitation at 442 nm, and the slit widths were set to be 5 nm and 10 nm respectively. Mutants of A118R1 and V121R1 as well as wild-type were not tested in this part of experiments.

80

From the results above, the efficacy of seeding assay could varied between different amounts of seeds such as in mutants of A113R1 and M138R1, but it could be also unobvious for the rest of the mutants. This kind of variance could be either concentration-dependent or mutant-dependent (or could be both) in the assay. For example, higher amounts of seeds could accelerate the fibril growth in M138R1, but this doesn't work for L125R1 and M129R1. As for the peptide concentration, the efficacy of seeding could be distinguished in lower concentration of L125R1 but not with M129R1. The seeding assay using various seed quantities was also carried out in 80 uM of M129R1, and the result was quite consistent with the ones of M129R1 above (Figure A.4).

For convenience of comparison, the amounts of seeds were set to be either 2000 or 3000 pmol. In the 1-mL fibril solution, the molar ratio of monomer to seed would be 10:3 if seed of 3000 pmol was used and the peptide concentration was set to be 10 μM. The experiments of fibril formation for all peptides were then performed by seeding assay with the optimal lowest concentration listed in Table 4.1 (Figure 4.7).

(A) WT

(B) WT
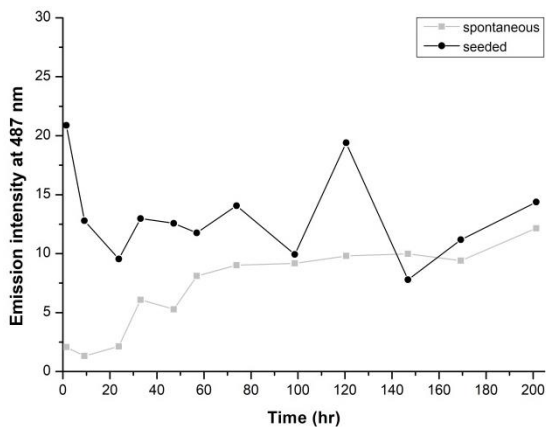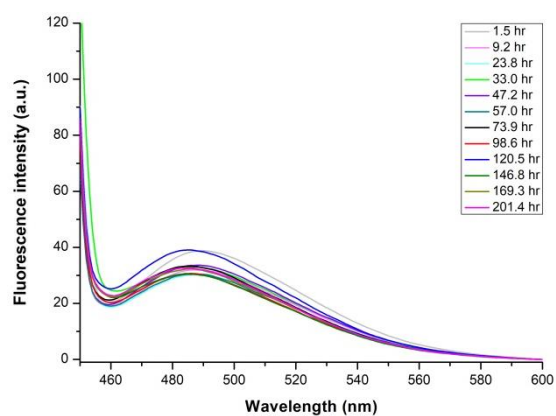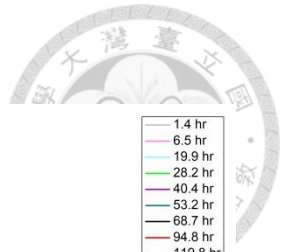
(C) A113R1
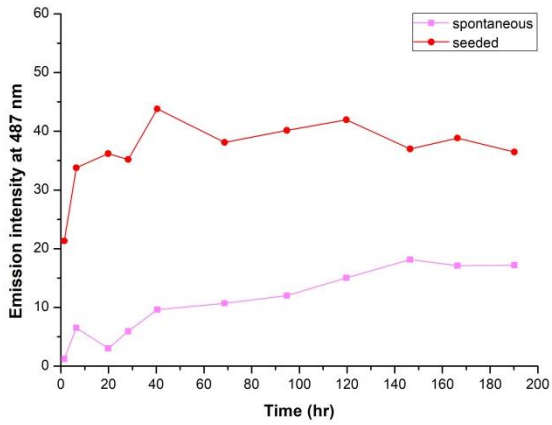
(D) A113R1

(E) A118R1

(F) A118R1

(G) V121R1

(H) V121R1

82
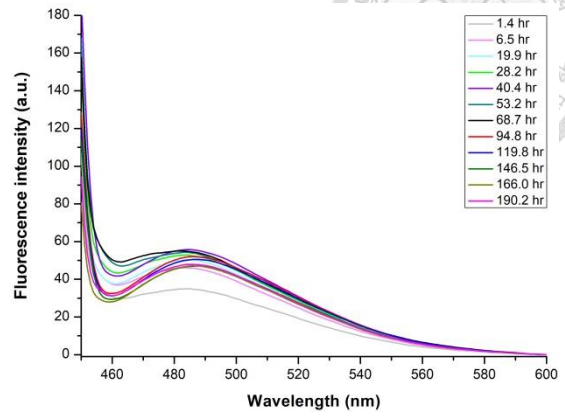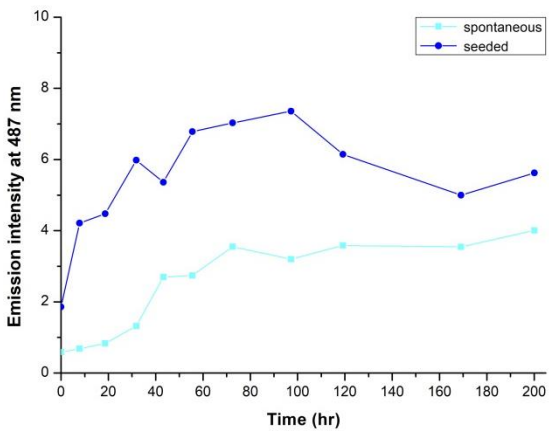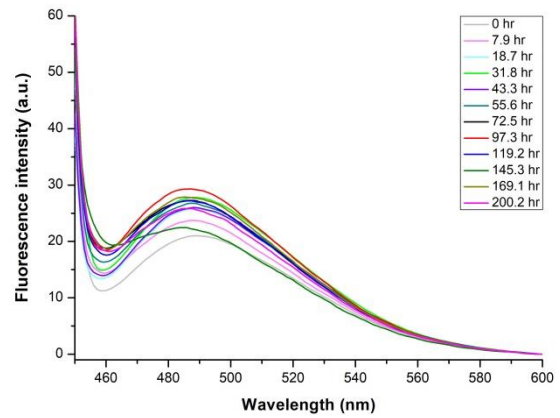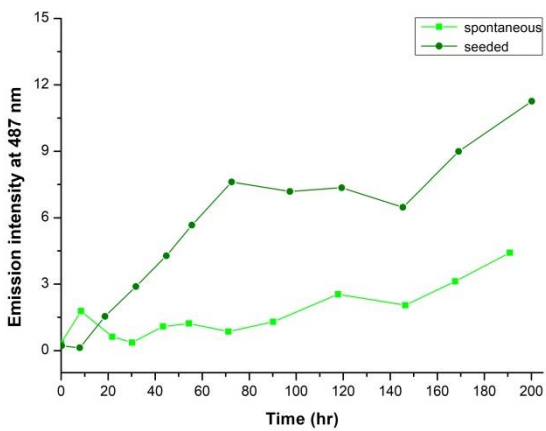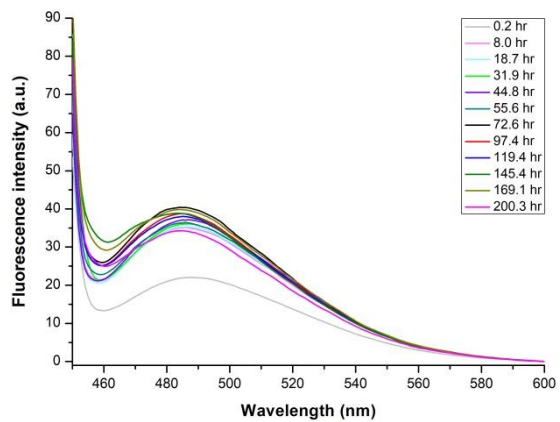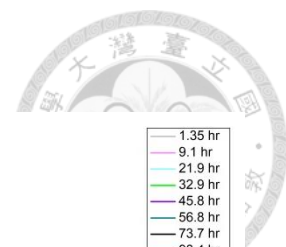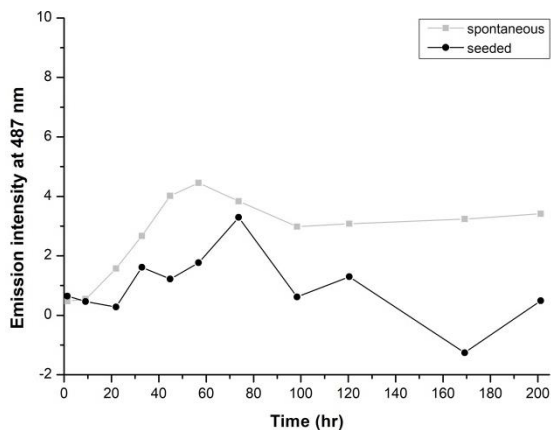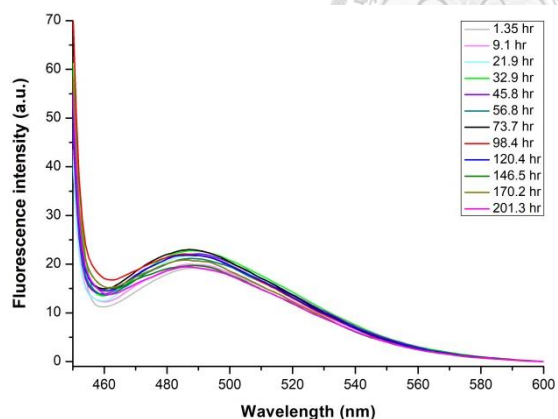
(I) L125R1
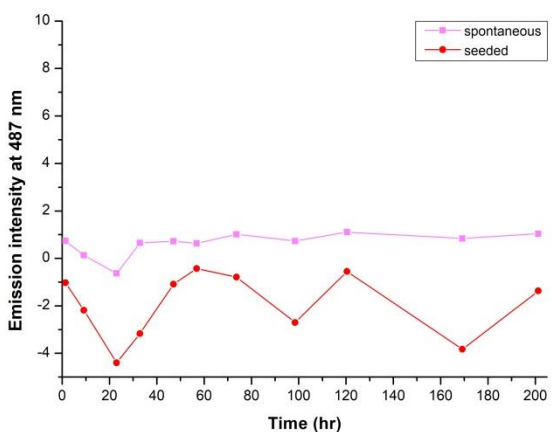
(J) L125R1

(K) M129R1
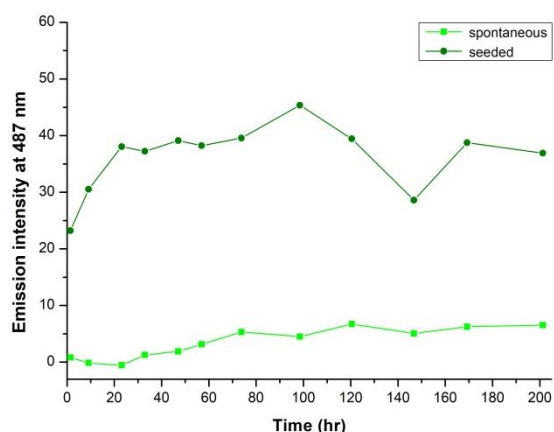

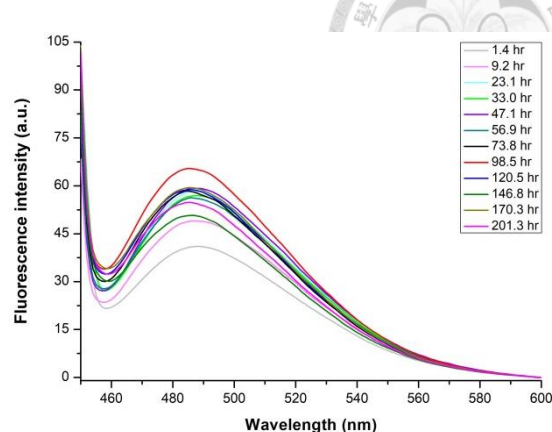**(L) M129R1**

(M) M134R1

(N) M134R1


83
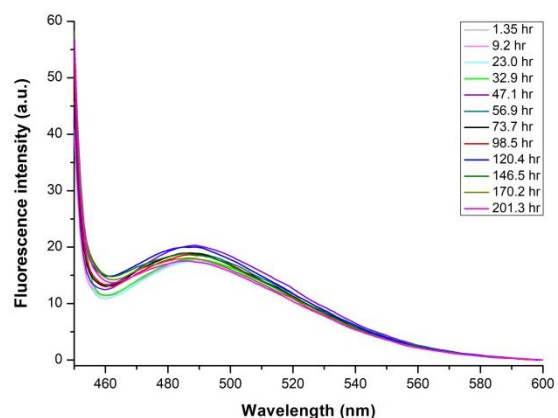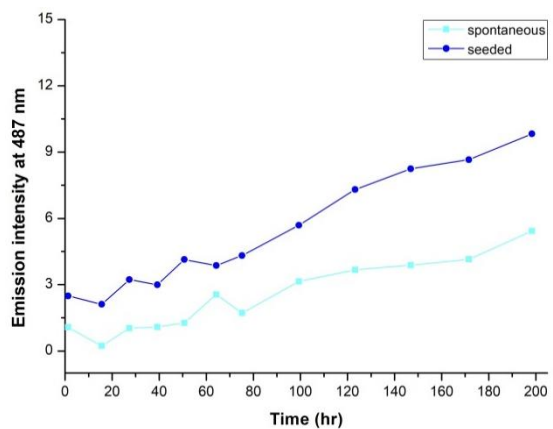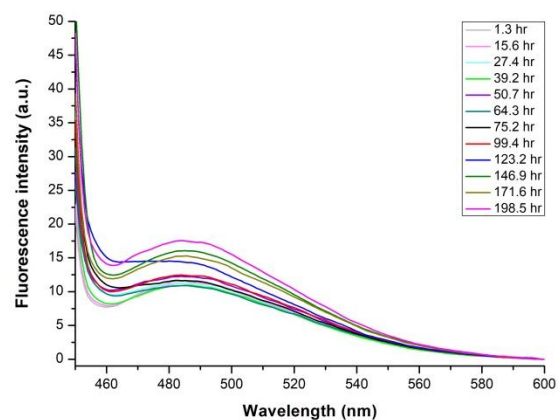
(O) M138R1

(P) M138R1

Figure 4.7 Seeded fibril formation of HaPrP(108-144) peptides with the lowest concentration of peptides.

The seeded fibril formation of peptides **(A)** WT, **(C)** A113R1, **(E)** A118R1, **(G)** V121R1, **(I)** L125R1, **(K)** M129R1, **(M)** M134R1, and **(O)** M138R1 were tested with the lowest concentration by seeding assay. The fluorescence spectra of the seeded peptides listed from **(B)** to **(P)** were drafted for visualizing the fibril growth. All peptides were seeded by 3000 pmol of seeds, except for A113R1 and M134R1 by 2000 pmol.

According to the spectra above, the efficacy of seeding effect was not as good as expected in some of the samples. The mutants of A113R1, A118R1, V121R1, and M138R1 exhibited faster growth of fibrils after seeding, but L125R1, M129R1, and M134R1 showed no significant differences with the spontaneously formed fibrils, with the former two mutants even remaining lower intensity than spontaneous fibrils or slightly minus in the whole period. This might be due to the reason that the determined values of optimal lowest peptide concentration were too low for the peptide monomers to form enough fibrils to be detected by ThT molecule, and a little bit of errors in fluorescence intensity could lead to minus values of fluorescence intensity after calibration.

To further examine the efficacy of seeding, slightly higher values of peptide
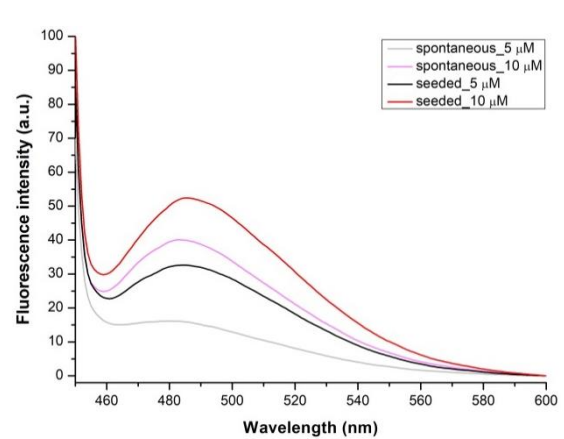
84
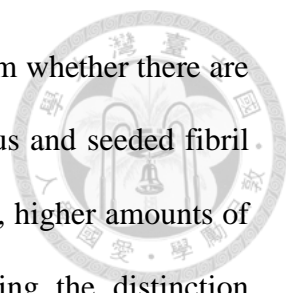
concentration were tested along with seeding assay, aiming to confirm whether there are better choices of concentration values for distinguishing spontaneous and seeded fibril formation. Based on the previous tests of different amounts of seeds, higher amounts of seeds were temporarily not taken into consideration for improving the distinction because it might be mutant-specific and fail to work. Also, in some of the samples below, to prevent the catch-up of spontaneous fibril growth, the fibril formation would be stopped in the middle of the incubation period and the fibrils would be collected for ESR sample production, as indicated by black arrows. This would make the ESR data more convincing that the differences between seeded and spontaneously formed fibrils truly originated from seeding effects.
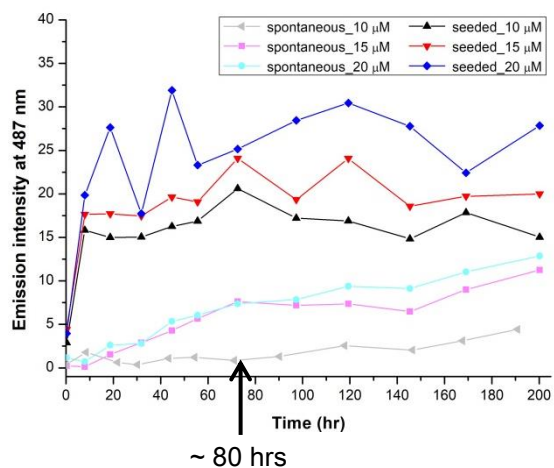
(A) WT

(B) WT

(C) A118R1

~ 80 hrs

(D) A118R1

85

(E) V121R1

~ 80 hrs

(F) V121R1

(G) L125R1
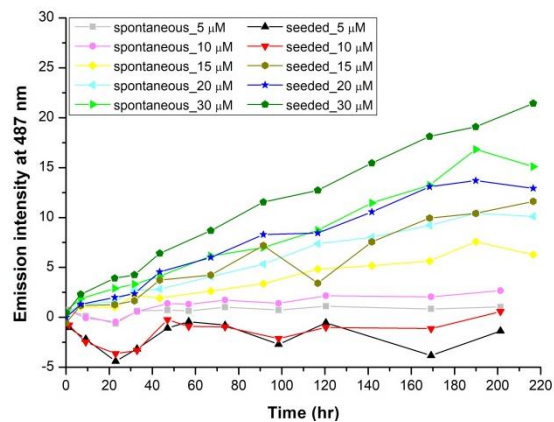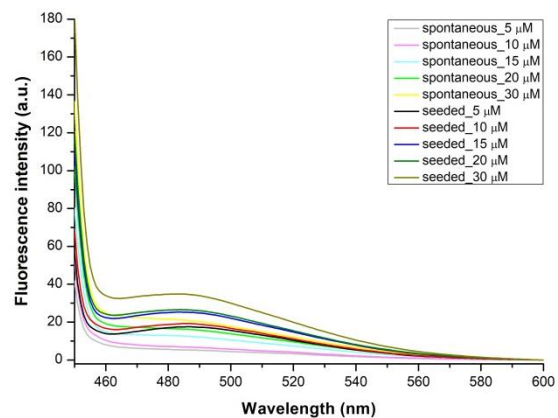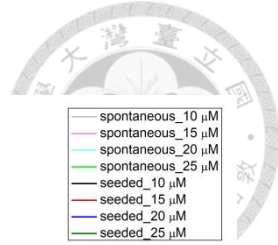

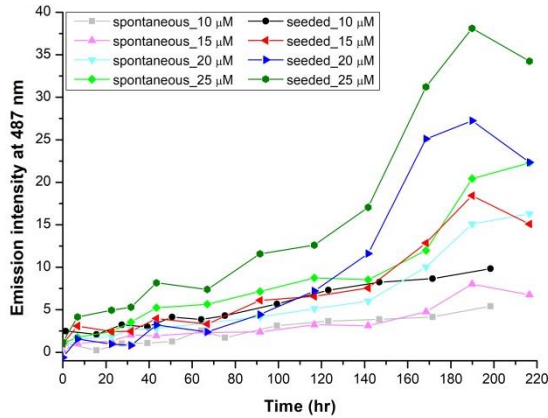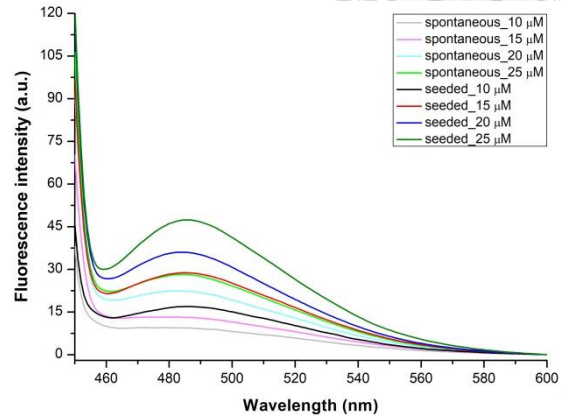
~ 20 hrs

(H) L125R1

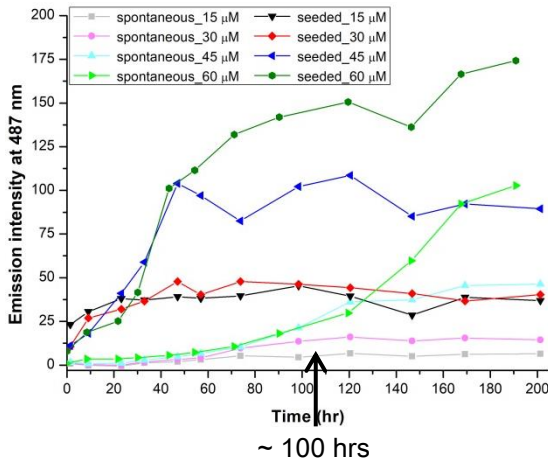**(I) M129R1**

(J) M129R1
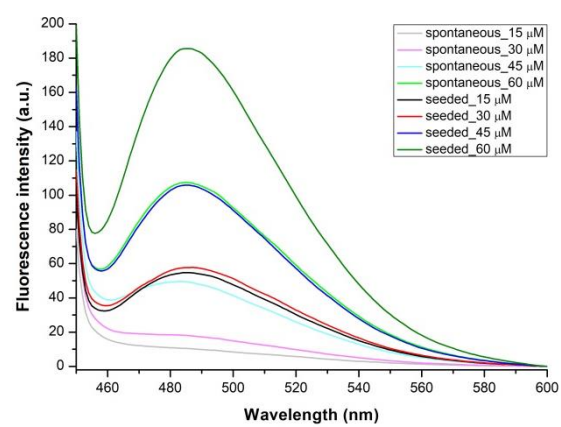

86
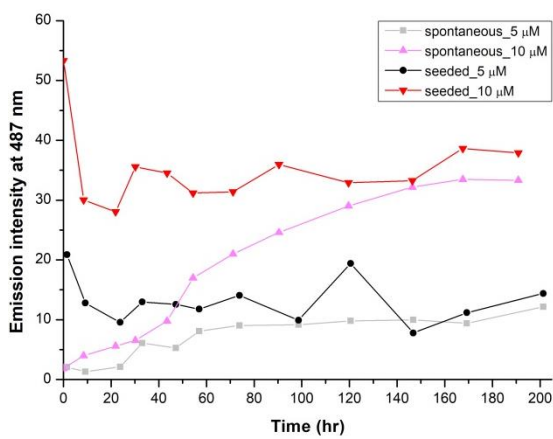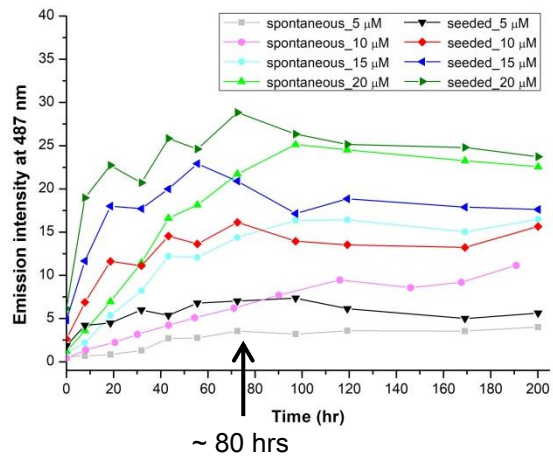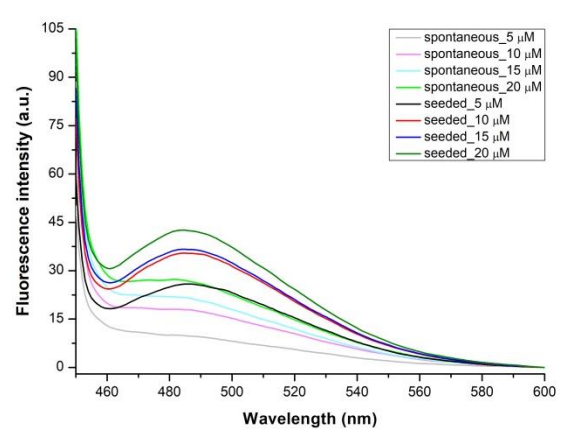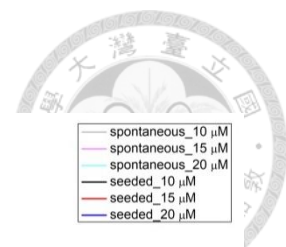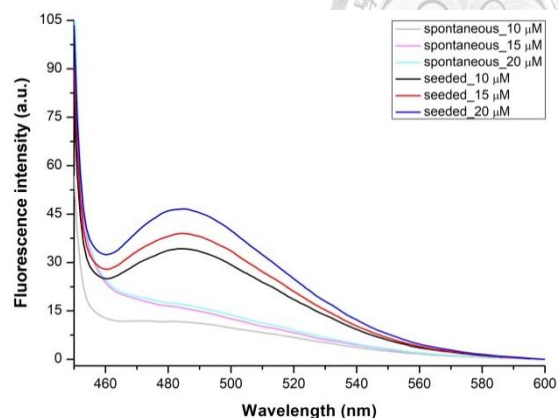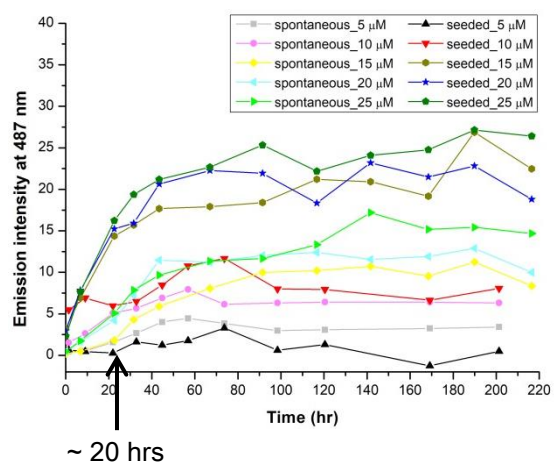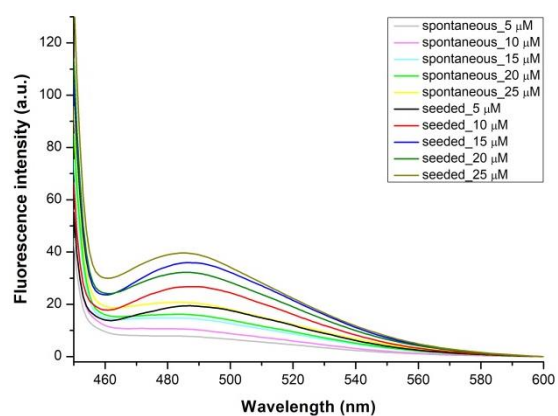
(K) M134R1

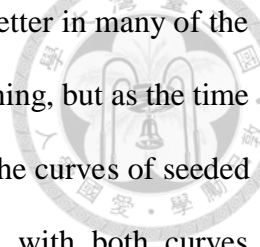**(L) M134R1**

(M) M138R1

~ 100 hrs

(N) M138R1

Figure 4.8 Seeded fibril formation of HaPrP(108-144) peptides with slightly higher concentration of peptides.

The seeded fibril formation of peptides **(A)** WT, **(C)** A118R1, **(E)** V121R1, **(G)** L125R1, **(I)** M129R1, **(K)** M134R1, and **(M)** M138R1 were tested with slightly higher values of concentration by seeding assay. The fluorescence spectra obtained from the last data point were drafted together between different values of concentration as from **(B)** to **(P)**. Mutant of A113R1 was not tested in this part of experiment. All peptides were seeded by 3000 pmol of seeds. The black arrows indicated in the graphs represent the time when we stopped the fibril formation and collected the fibrils for ESR sample production.

The curves of spectra from seeded samples above were drawn in deep colors, and curves of spontaneous samples were drawn in their corresponding light colors. From the

87

results above, we could see that the efficacy of seeding assay went better in many of the mutants. For A118R1, the seeding effect was prominent in the beginning, but as the time went on, the curves of spontaneous fibril formation would catch up the curves of seeded samples. This was more obvious as the concentration increased, with both curves reached to ceiling after 60~80 hours of incubation. For V121R1, the seeding effect was very obvious in all of the samples. For L125R1, the seeding effect was better when the concentration was increased to values over 15 μM, but it was soon caught up by curves of spontaneous fibrils after 30~40 hours. The mutants of M129R1 and M134R1 exhibited the worst seeding efficacy among all the samples for not showing significant differences between spontaneous and seeded fibril formation even the concentration was raised to 30 μM. For M138R1, the efficacy was great in all of the samples, and it was even better when the concentration was increased to more than 45 μM. As for wild-type, the intensity of seeding had reached to its limit once it was introduced seeds, and unexpected increase of intensity was observed in the first data point.

Finally, the spectra between different mutant and wild-type peptides were also compared based on roughly the same values of peptide concentration including 10 and 15 μM and quantities of seeds including 2000 and 3000 pmol (Figure 4.9). The increases of fluorescence intensity were not so regular, as intensity of wild-type, A113R1 and M138R1 already reached their ceiling from the beginning of the incubation period. Within other mutants, the fibrils A118R1 and V121R1 grew faster than L125R1, M129R1, and M134R1, and M129R1 again showed the least and nearly no significant growth.

(A) **(B)**
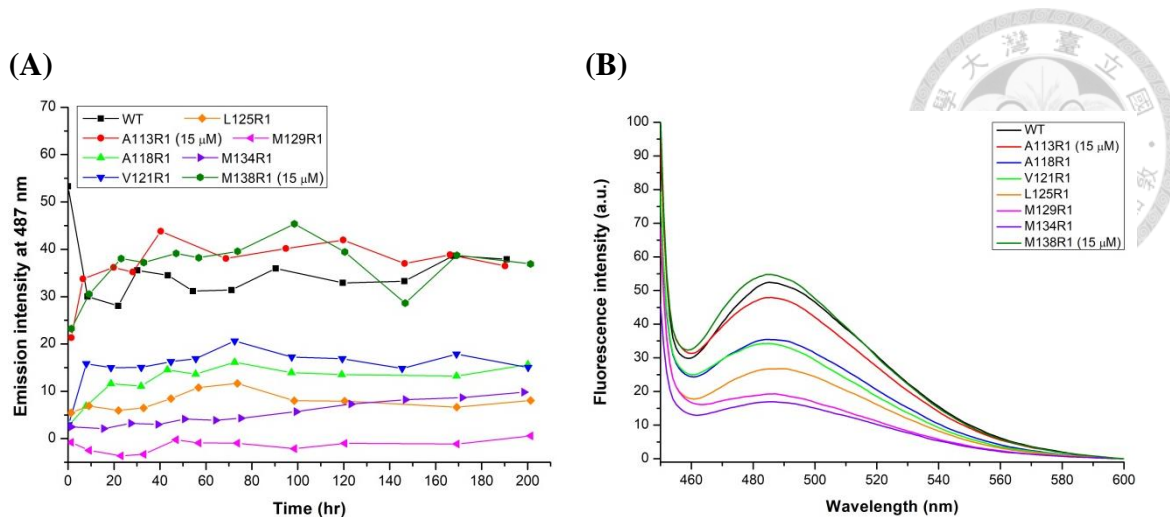
Figure 4.9 Comparison of seeded fibril formation between different HaPrP(108-144) peptides.

The fluorescence spectra from seeded fibril growth of the peptides listed above were organized and compared for their relative rate of growth. The kinetic curves showing values of emission intensity at 487 nm of the samples were drafted together for comparison as **(A)**. The fluorescence spectra obtained from the last data point were drafted together between different values of concentration as **(B)**. All values of the peptide concentration were 10 μM, except for A113R1 and M138R1 being 15 μM. All peptides were seeded by 3000 pmol of seeds, except for A113R1 and M134R1 by 2000 pmol.

From the serial tests of seeding assay, now we could be sure to a degree about the differences between spontaneous and seeded fibril formation, which could help us move on to the next step of ESR spectroscopy. Once the fibril formation was distinguished by ThT binding assay, all of the mutant samples were collected and prepared for ESR measurement to determine the spin-spin interaction, aiming to elucidate the structural features of the mutant fibrils. Furthermore, the fibril samples were double checked by examining the fibril morphology by TEM as a second proof of the fibril existence.
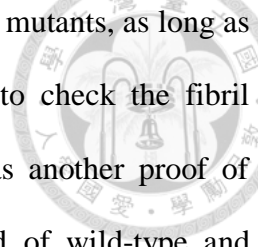
89

90

Chapter 5 Results (III): TEM & ESR Spectroscopy

After the growth of amyloid fibrils from hamster prion peptides was monitored by ThT binding assay, the fibrils were further examined and analyzed by TEM and ESR spectroscopy. The former is to check the morphology of the amyloid fibrils, and the latter is to elucidate the fibril structure by measuring the spin-spin interaction between the spin labels on the mutant peptides.

5.1 Fibril morphology observation by TEM

Transmission electron microscopy (TEM) is a powerful tool to investigate the morphology of biomolecules such as virus particles, bacteria, and protein aggregates. It can also be used to visualize the architecture and organelles inside the cells. The imaging is achieved by elucidating angles of diffraction after the electron beams collide with samples of very thin layer. Through the technique of negative staining, which makes the specimen visible by staining the background, atomic structures of the biomolecules could be studied with much better resolution than the traditional light microscopy. Some negative stains including uranyl acetate, phosphotungstic acid and ammonium molybdate are suitable for this technique, since they scatter electrons strongly and adsorb to biological substances well, which make the images clear enough to interpret.

In the fields of prion amyloidogensis, TEM had been used in many studies to examine the morphology of prion protein and peptide fibrils (Chatterjee, Lee et al. 2013, Cheng, Huang William et al. 2013, Yang, Lo et al. 2015), and fibrils formed of different segments of hamster prion peptide had also been observed in Howard's thesis. Yet no observation of spin-labeled prion peptide fibril morphology had been made before.

In this thesis, all of our amyloid fibrils, including wild-type and mutants, as long as seeds produced from wild-type fibrils, were examined on TEM to check the fibril morphology after either spontaneous or seeded fibril formation, as another proof of presence of amyloid fibrils. Morphologies between fibrils formed of wild-type and mutant peptides and between spontaneous and seeded were also compared. Rod-like or silk-like morphologies are expected to be observed, and presence of amorphous aggregation was checked as a negative indicator of amyloid structural formation.
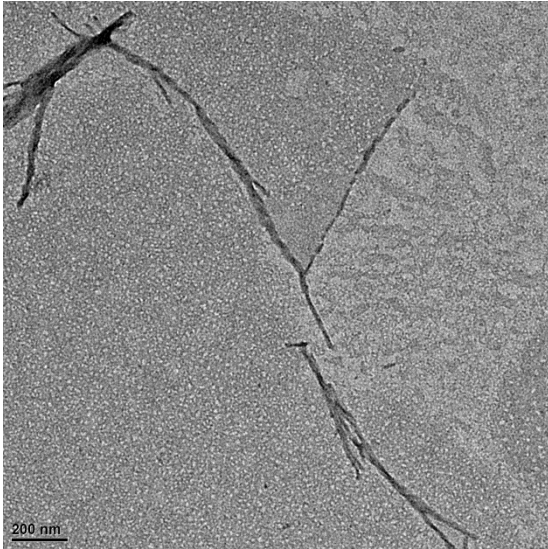
5.1.1 Morphology of spontaneously formed fibrils

Before being observed on TEM, the TEM samples were prepared by loading aliquots of fibril solution onto the copper grid and staining the fibrils with either phosphotungstic acid (PTA) or uranyl acetate (UA) stains. The hydrophobicity of the copper grid could hold up the hydrophobic prion peptide fibrils so the fibrils would adsorb onto the grid stably. Before staining, the grid was washed gently by little amount of water to remove the salts from the fibril formation buffer. The loading of water onto the grid should be gentle to avoid washing the fibrils away. In addition, the time of staining could vary based on different samples or different stains that were used. According to previous studies, the staining time of uranyl acetate was set to be 4 minutes (Chatterjee, Lee et al. 2013), and the time of PTA was 1 minute for prion peptides (Cheng, Huang William et al. 2013). Nevertheless, it had also been suggested that 15 seconds of uranyl acetate staining would be enough to visualize the fibrils. Since the stains could bind to the grid too tightly and block the vision on fibrils as the staining time increases, in this study, the average of staining time using either uranyl acetate or PTA was set to be near 15-40 seconds, and the time was lengthened based on necessity
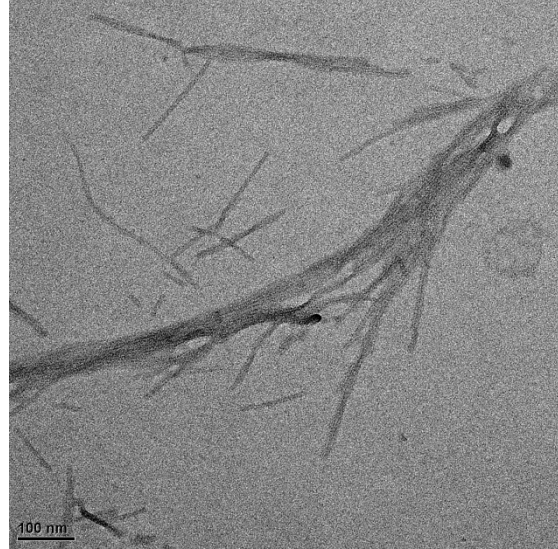
92

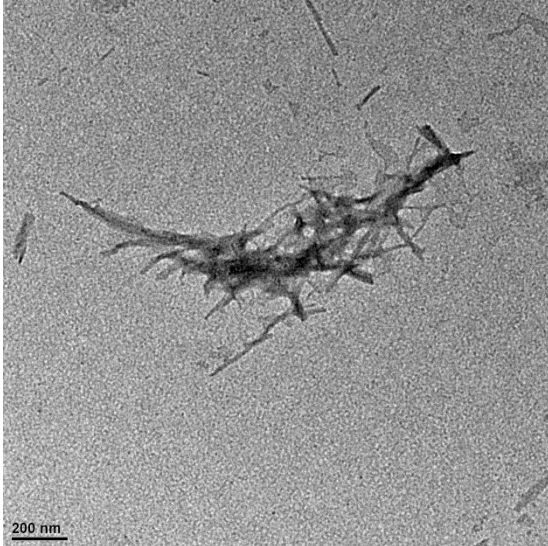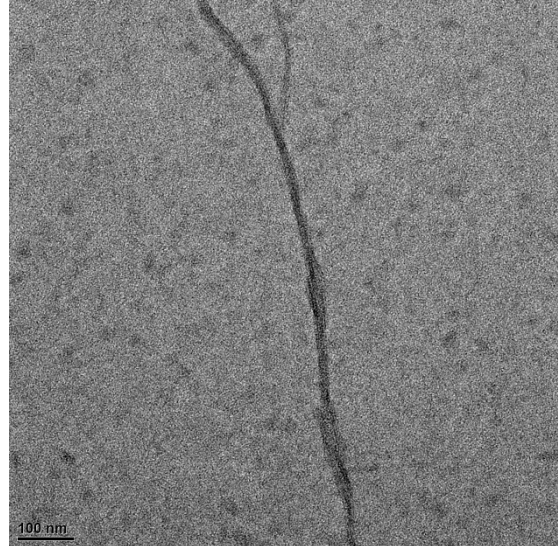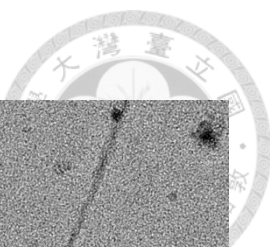if the imaging of fibrils was not good enough for observation.
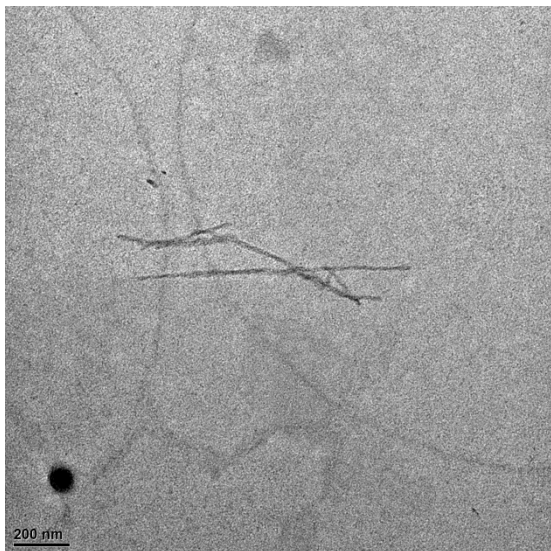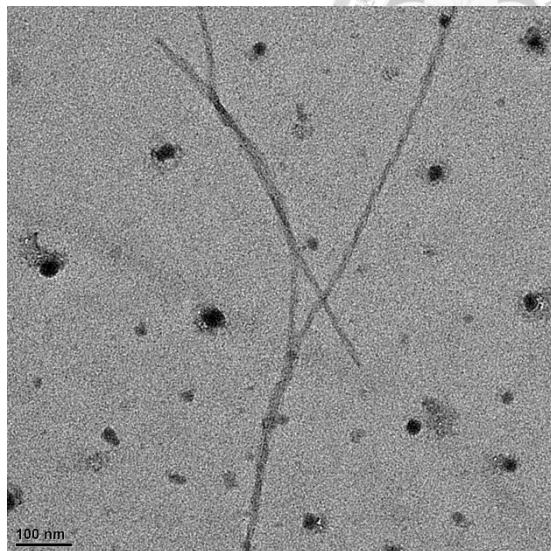
(A) WT

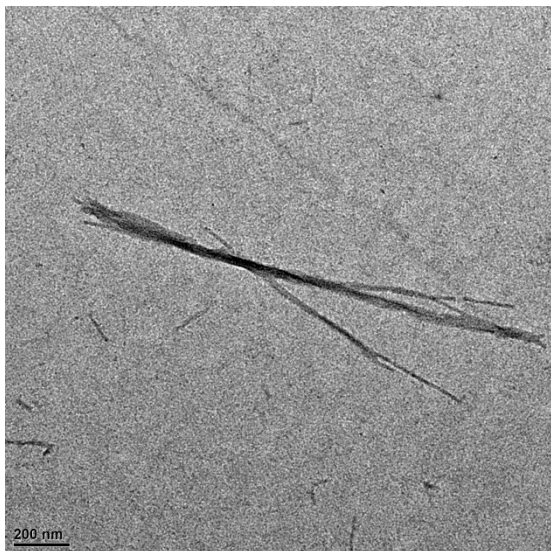**(B) WT**

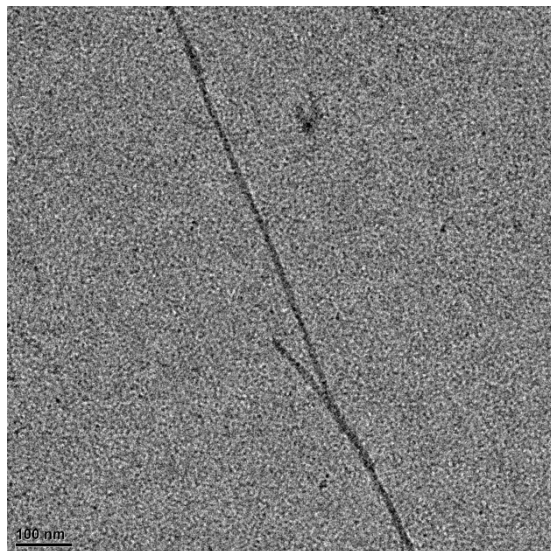**(C) A113R1**

(D) A113R1

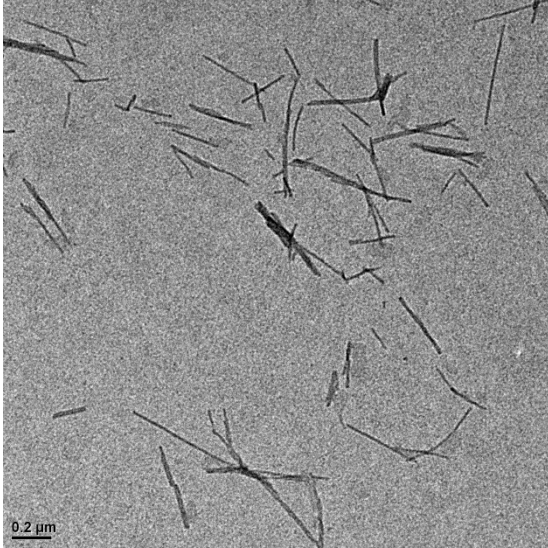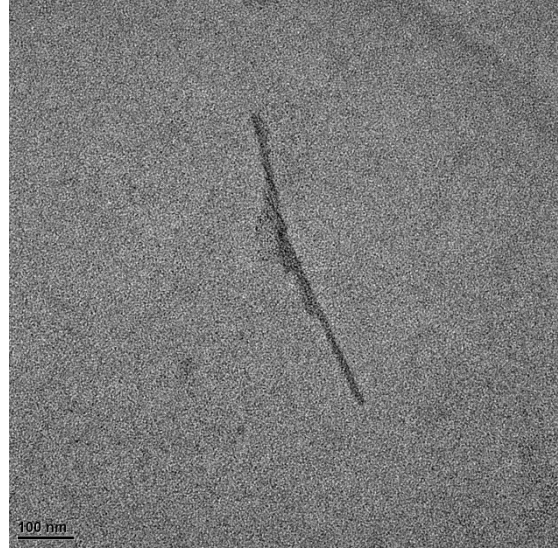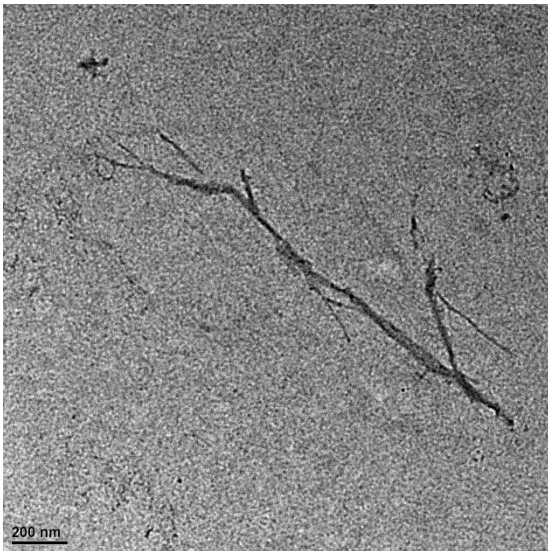

93

(E) A118R1

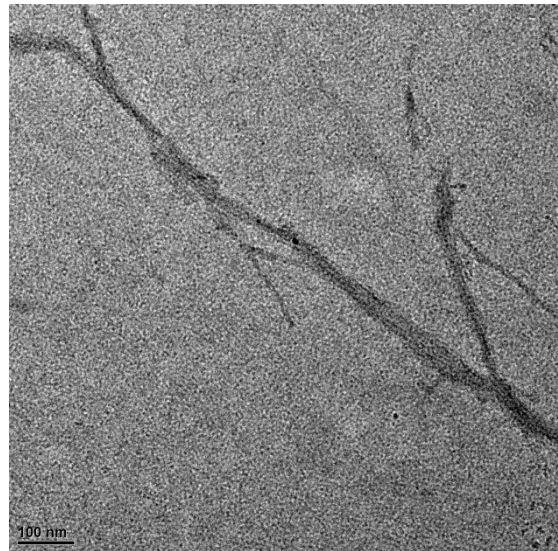**(F) A118R1**

(G) V121R1

(H) V121R1

94

(I) L125R1

0.2 µm

(J) L125R1

100 nm

(K) M129R1

200 nm

(L) M129R1

100 nm

95
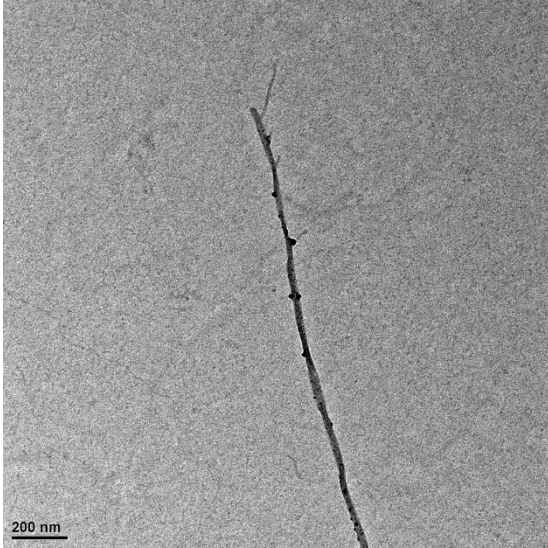
(M) M134R1

(N) M134R1
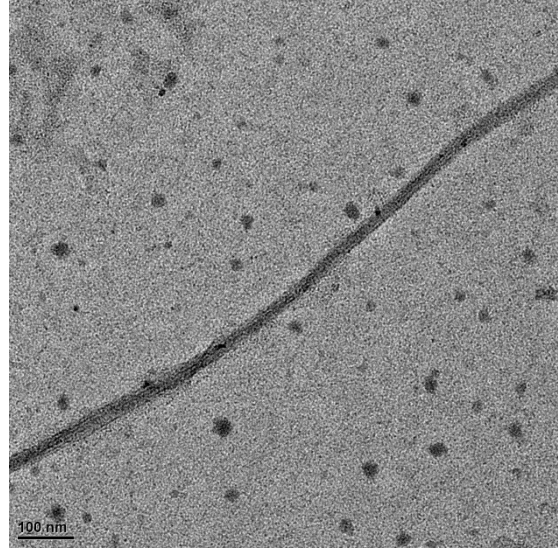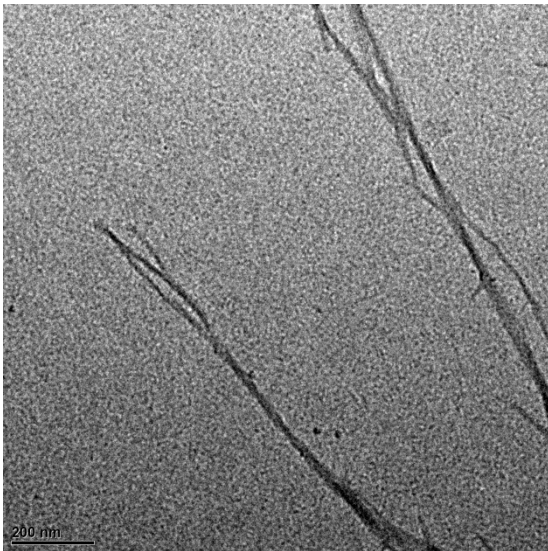
(O) M138R1

(P) M138R1
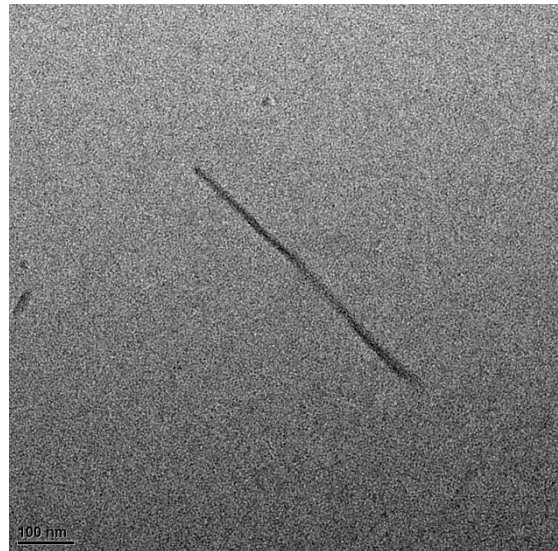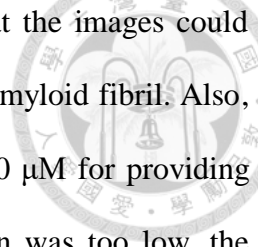
Figure 5.1 TEM images of spontaneously formed HaPrP(108-144) amyloid fibrils.
All of the samples were incubated at 37℃ quiescently and stored in 4℃ refrigerator after the incubation period ended. All of the samples were negatively stained by 2 % (w/v) uranyl acetate except for **(B)** of WT being stained by 2 % (w/v) phosphotungstic acid. The images were chosen based on scale bars of either 100 or 200 nm. The values of concentration of the samples used for TEM observation are listed below:

WT: 100 and 60 μM; A113R1: 80 μM; 15 μM, 20 μL with 3 repeats; A118R1: 90 μM; V121R1: 90 μM; L125R1: 105 μM; M129R1; 85 μM, M134R1; 80 μM; M138R1: 60 μM with two repeats.

The images above had been selected out from the criteria that the images could exhibit the clearest fibril morphology with nearly single bundle of amyloid fibril. Also, the values of sample concentration were controlled to be at least 60 μM for providing sufficient amounts of fibrils to observe. If the initial concentration was too low, the procedure of sample loading onto the grid was repeated several times until the total amount of fibrils were assumed to be enough. Images of larger scales were also collected, offering a broader view of the distribution and density of fibrils under the scope of TEM (Figure A.5).

From the images above, we could tell that the morphology of spin-labeled mutant fibrils was obvious enough to tell with the feature of rod-shaped fibril sticks that were often accumulated in bundles. However, one should keep the fact in mind that the amounts of observable fibrils under the scope of TEM would vary from time to time, and images of good quality were not guaranteed to be obtained in every case. Besides, the morphology of the wild-type fibrils exhibited feature of twisted structure that were not so obvious in other mutants.

We next examined the morphology of fibrils formed by seeding assay. Since the fibrils prepared by seeding were formed at a faster rate, the final structure of the fibrils might be discriminated from the structure of spontaneously formed fibrils.

5.1.2 Morphology of fibrils formed by seeding

Before the seeded fibrils were observed, the morphology of seeds freshly prepared from wild-type fibrils was first examined (Figure 5.2). The same experiment had been carried out in Howard's thesis on seeds from different segments of hamster prion peptide, showing the feature of fragmented fibril sticks or bundles.

97

(A)
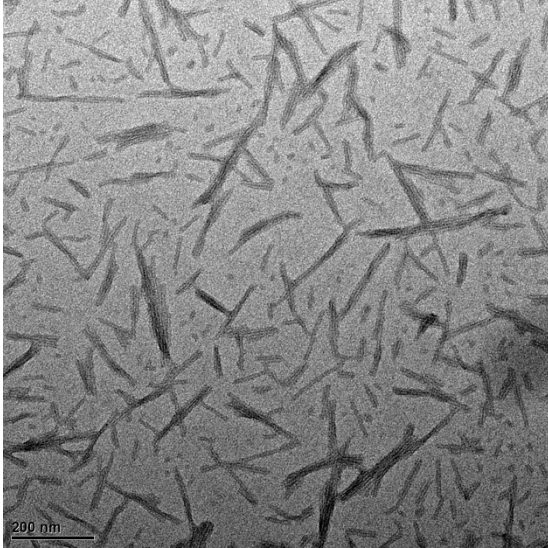
(B)
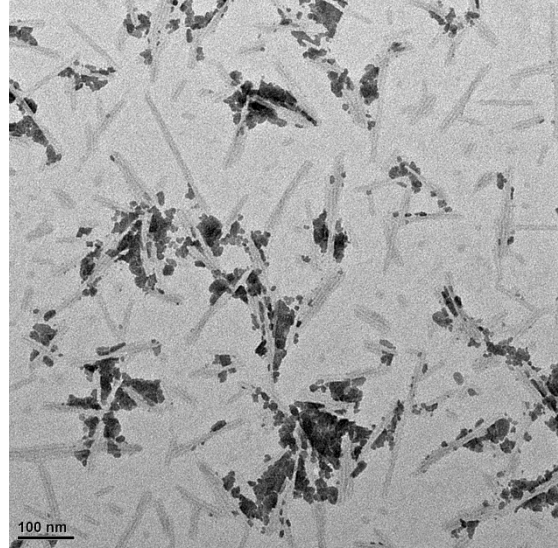
(C)
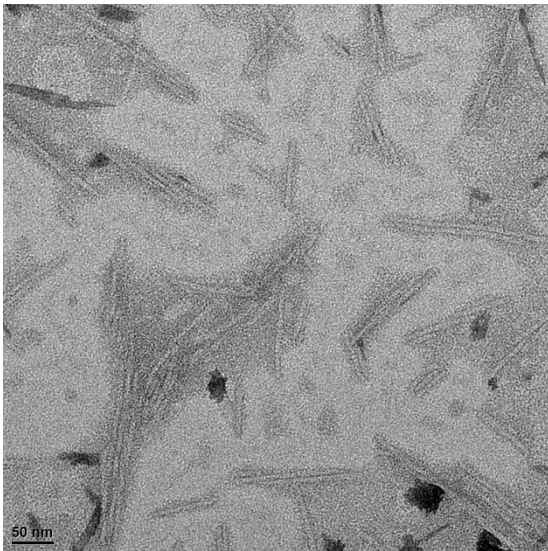
Figure 5.2 TEM images of seeds prepared from wild-type peptides.

The seeds were prepared from mature fibrils incubated over 1 month and then stored in 4℃. The samples were negatively stained by 2 % (w/v) uranyl acetate. The concentration of seed was calculated to be 96.4 µM. The images were chosen based on scale bars of **(A)** 200, **(B)** 100 or **(C)** 50 nm.

Surprisingly, the effect of negative staining in these samples was good that the

contrast between seeds and background was better than images of other peptide samples,

with some flaws that a small portion of the stains were stuck on the grid in some of the samples. The better effect of staining might result from the phenomenon that the shorter length of seeds had made the stains harder to adsorb on the samples, bringing less but more suitable intensity of staining.
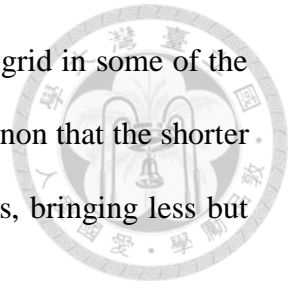
The morphology of fibrils formed by seeding assay was next examined with exactly the same procedures as previously described (Figure 5.3).

(A) WT
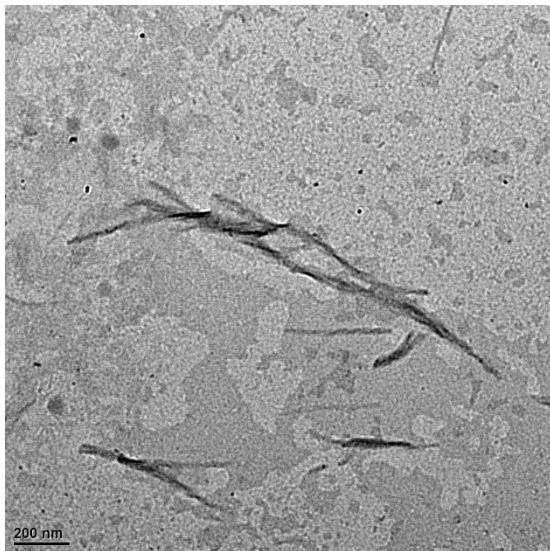
(B) WT
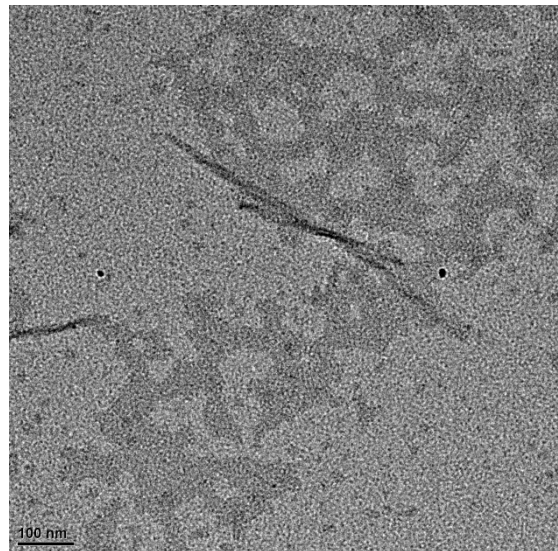
(C) A113R1
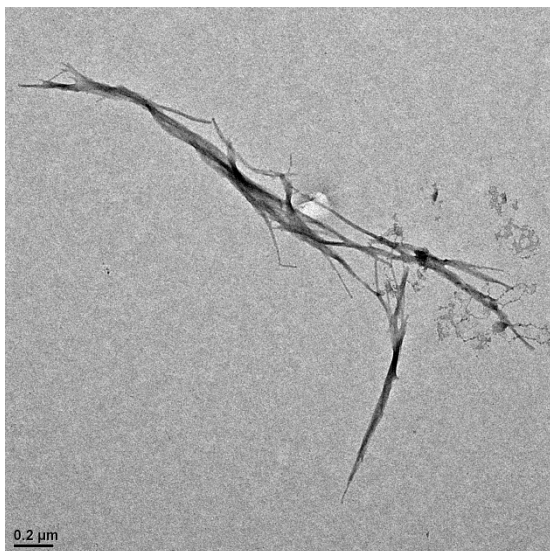
(D) A113R1
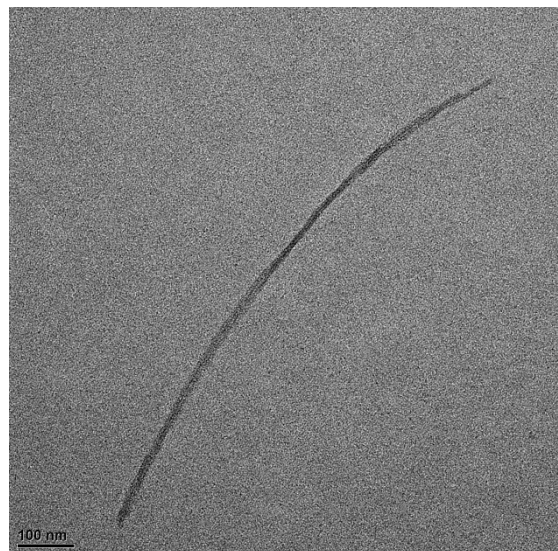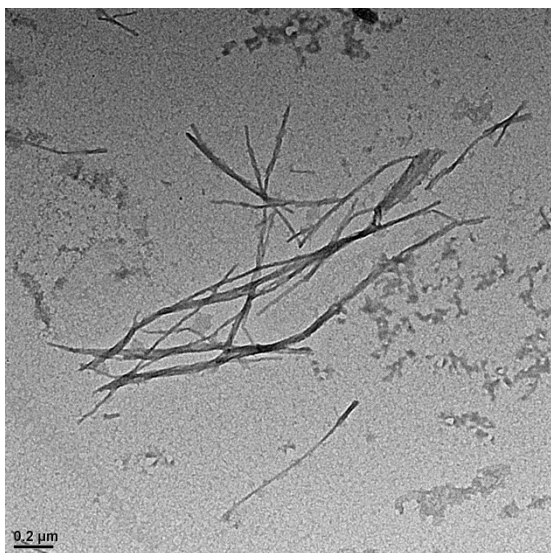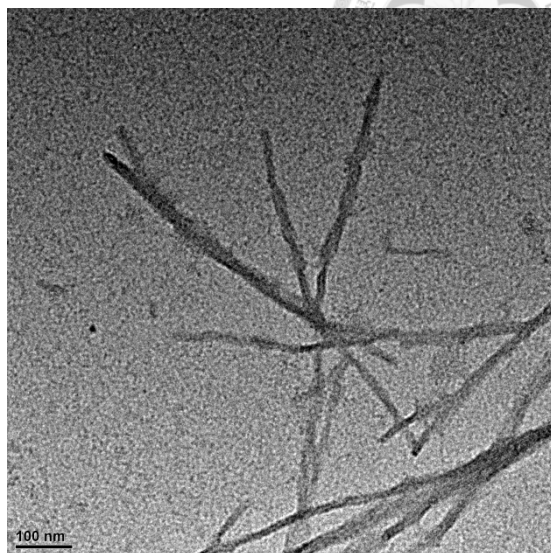
99

(E) A118R1

(F) A118R1

(G) V121R1

(H) V121R1

100

(I) L125R1

(J) L125R1

(K) M129R1

(L) M129R1

101

(M) M134R1

0.2 μm

(N) M134R1

100 nm

(O) M138R1

200 nm

(P) M138R1

100 nm
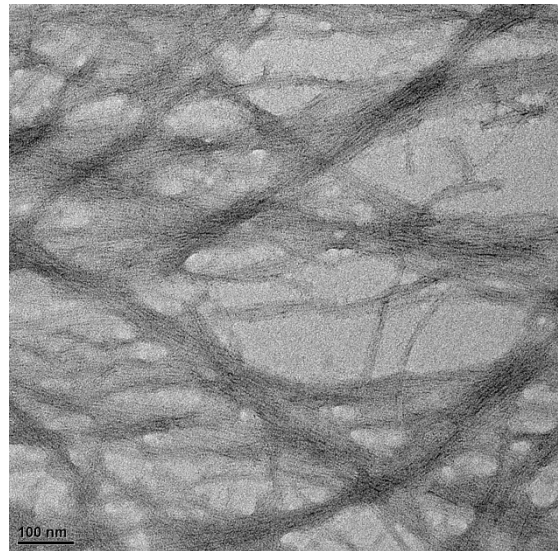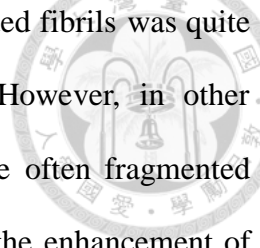
Figure 5.3 TEM images of HaPrP(108-144) amyloid fibrils formed by seeding.

The samples were all negatively stained by 2 % (w/v) uranyl acetate. The values of concentration of the samples used for TEM observation are listed below:

WT: 10 μM, 20 μL with 5 repeats; A113R1: 15 μM; A118R1: 10 μM, 20 μL with 5 repeats; V121R1: 15 μM, 20 μL with 3 repeats; L125R1: 105 μM; M129R1: 85 μM; M138R1: 130 μM. The fibrils of M134R1 were collected from its ESR sample. The images were chosen based on scale bars of either 100 or 200 nm.

102

The images above showed the fact that the morphology of seeded fibrils was quite similar with the morphology of spontaneously formed fibrils. However, in other instances of observation, the fibrils from seeding assay were more often fragmented instead of being long, thin sticks (data not shown), indicating that the enhancement of fibril growth might still affect the resulting morphology.

Images of different scales could be seen in Figure A.6. The seeds in Figure A.6 exhibited different density of distribution because the seeds of (B) had been stored in $4°$ C refrigerator for weeks, resulting in the aggregation of seeds that showed thick bundles of short fibrils in the image. In addition, since it was suggested that fibrils formed in different rate could possibly result in different morphology, the fibrils formed in different buffer were also sent for TEM observation. Based on the result of Figure 4.1 that fibrils grew much slower in sodium acetate buffer, the fibrils formed in this buffer samely exhibited even thinner morphology (Figure A.7).

Finally, after the fibril morphology of the prion peptides were examined and compared, ESR spectroscopy was applied to elucidate the spin-spin interaction between the spin-labeled peptides.

5.2 ESR spectroscopy

ESR spectroscopy had been used to investigate the structures of amyloid protein aggregates including amyloid-β, tau and prion protein (Török, Milton et al. 2002, Margittai and Langen 2004, Yang, Lo et al. 2015), by measuring the intensity of spin-spin interaction between the peptides that were labeled with radical spins. By introducing external magnetic field onto the samples, the electrons on the samples would align in either parallel or antiparallel way and creates certain energy level differences. When this difference is equal to the energy of given photon, the electrons would transit to the upper state and emit light after returning back to the lower state, producing measurable spectrograms.

In the procedures of experiments, fibrils samples were spun down and dissolved in aliquot of 10% glycerol, and then spun down into the capillaries. The amounts of fibrils should be enough to offer the signal scanning of spin-labeled peptides. The capillaries were placed into a thicker NMR tube when cw-ESR measurements were carried out, and the experiments were done in Instrument Center of National Tsing Hua University by the aid of the doctor student Chien-Lun Hung from Dr. Yun-Wei Chiang's group. Before scanning, the spectrometer was calibrated and the samples were frozen to 200K. The scanning process was repeated more times if the signals from the electrons were too weak, but there would be a limit of signal resolution due to saturation effect.

The spectrograms were first compared by superposing the data of spontaneously formed fibrils and seeded fibrils in each mutant. The spectrogram of full-length hamster prion mutant protein M138R1 by seeding was served as the control showing the least linewidth. Since the spectrograms had been normalized by the total spin numbers of each mutant and could be compared with one another, the unit of the ordinates was
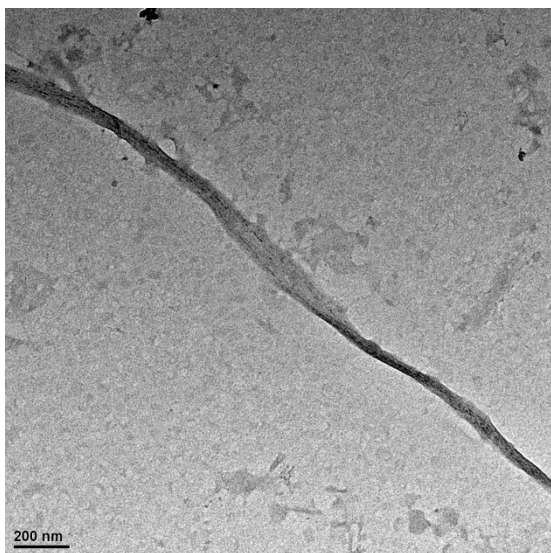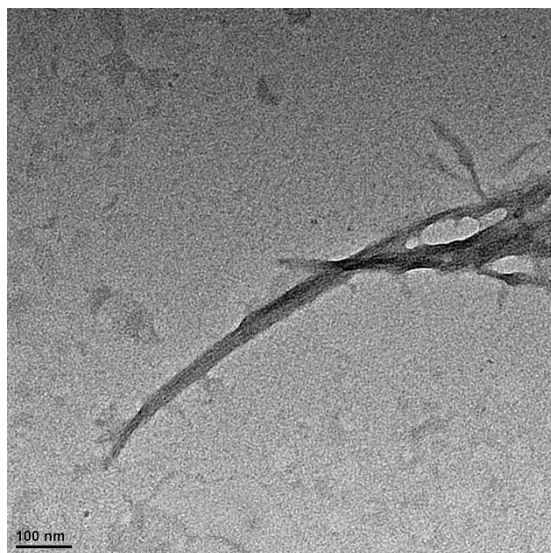
104

often abridged and not shown.
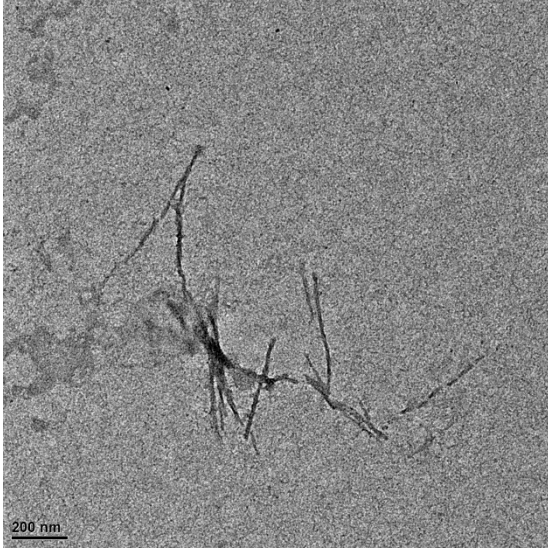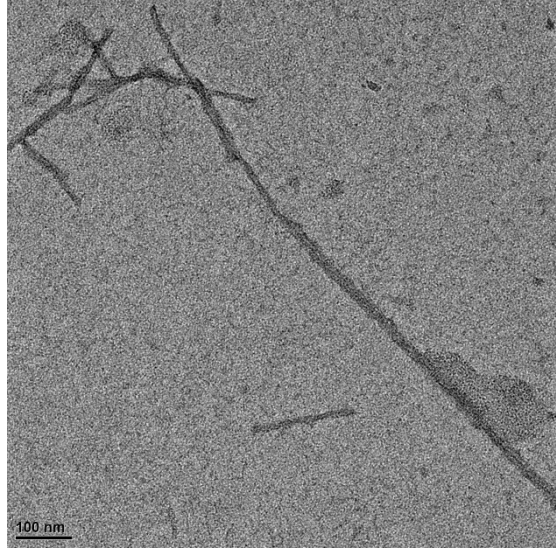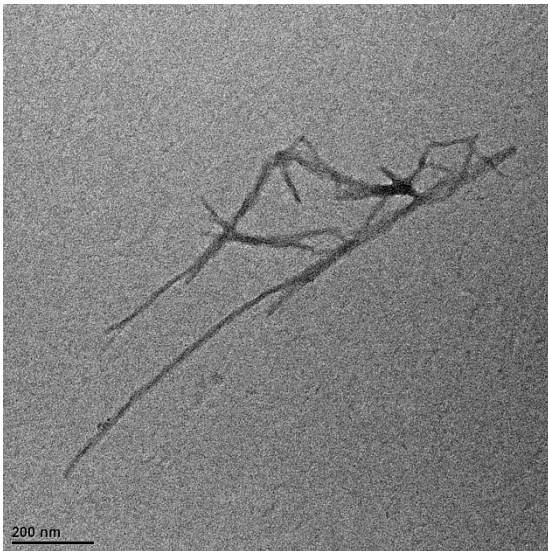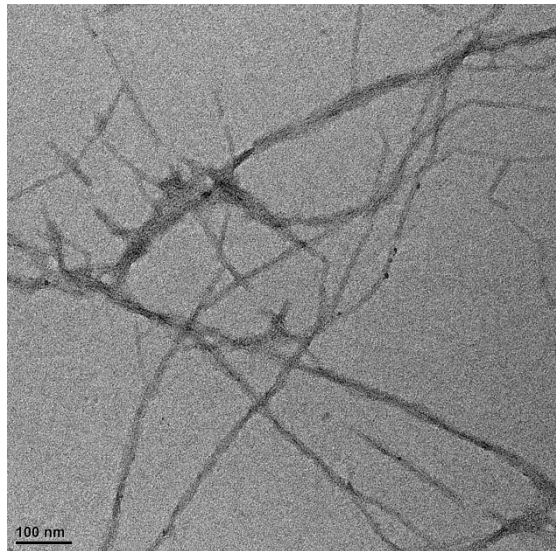
(A) A113R1
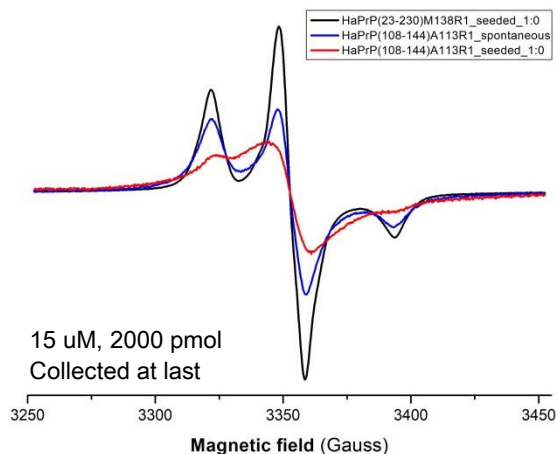
(B) A118R1
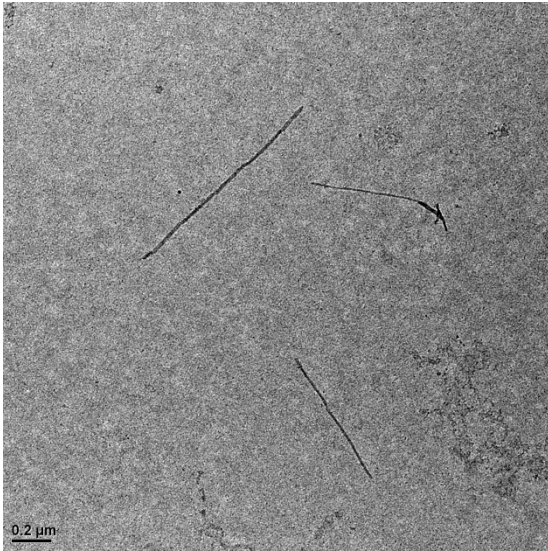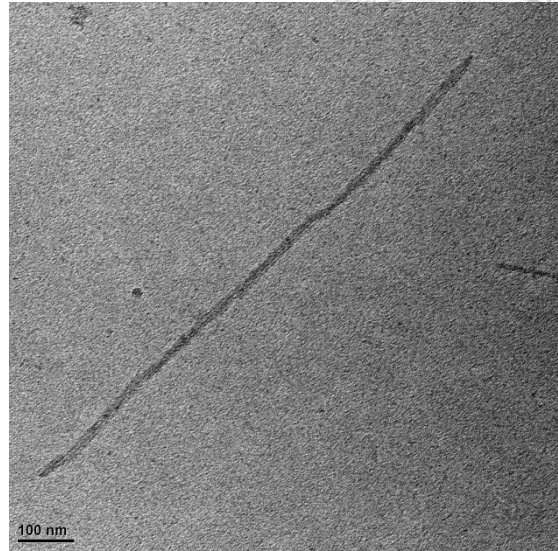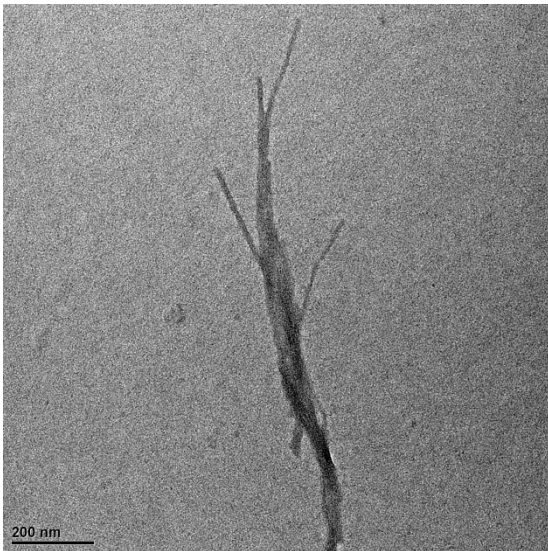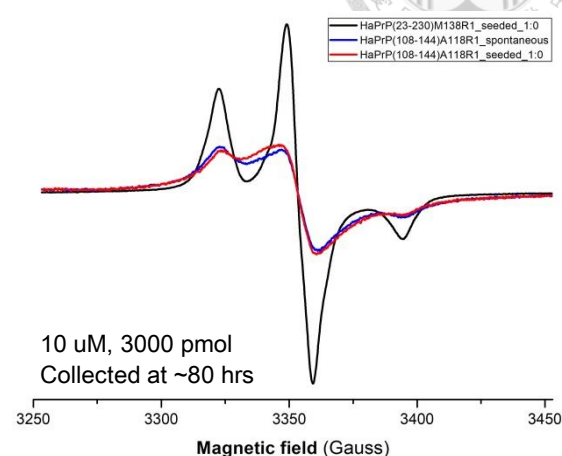

(C) V121R1

(D) L125R1

(E) M129R1

(F) M134R1

105
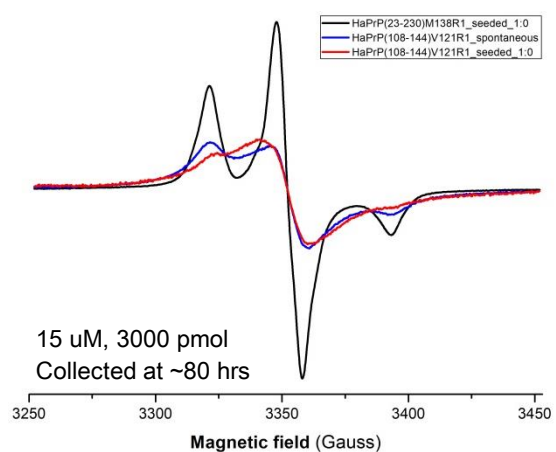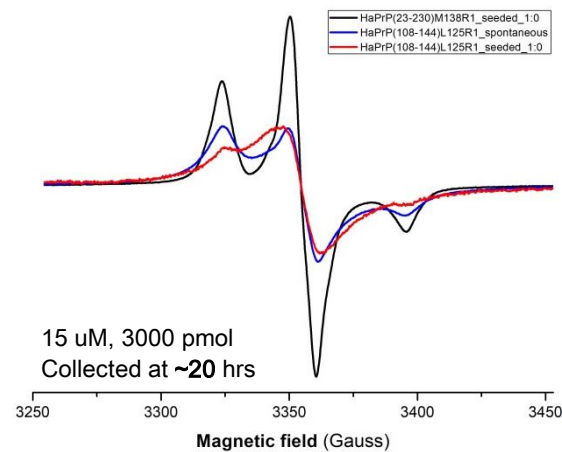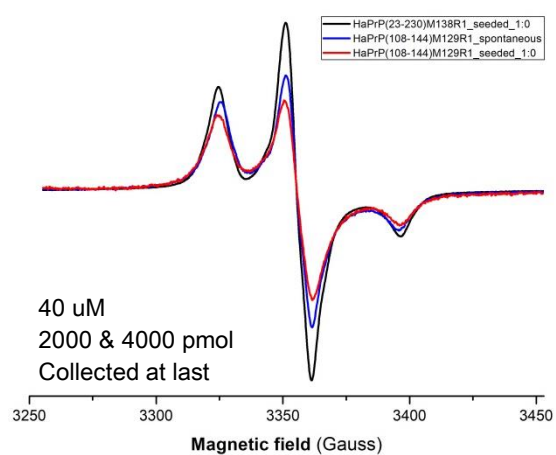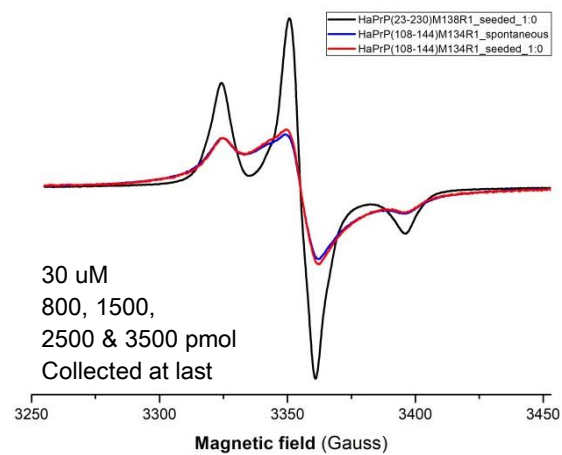
(G) M138R1
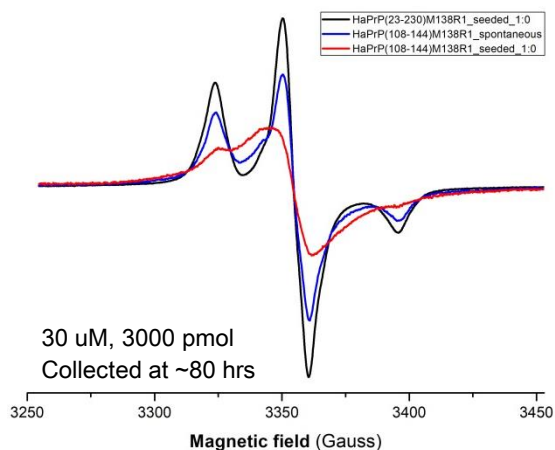
Figure 5.4 Comparison of ESR spectrograms between spontaneously formed fibrils and seeded fibrils in each mutant.

X-band continuous wave (cw)-ESR was measured at an operating frequency of ~9.42 GHz at the temperature of 200K. The sweep width of the measurement was 200 G, ranging from 3250 to 3450 Gauss. The original formation conditions of the seeded fibrils and the time of fibril collection were specified in each graph.

The spectrograms were compared based on their shape and their linewidth, which was designated the width near the baseline in the upper half of the spectrum. Usually if the shape of the curve is broader, the linewideth is more, and the sharper the curve is, the less the linewidth is. From the results above, the difference between spontaneous and seeded spectrograms could be mutant-dependent. For mutants of A118R1, V121R1, L125R1, and M134R1, the two spectrograms showed similar shapes and linewidths; For mutants of A113R1, M129R1, and M138R1, the spectrograms were more diverse than the other mutants, with linewidths of seeded fibrils more than the ones of spontaneously formed fibrils. This might indicate the fact that there might be structural changes of spin-labeling fibrils from spontaneous to seeded samples based on different labeling sites.

106

The spectrograms from all the mutant peptides were also superposed together and compared with the group of spontaneous and seeded fibrils divided, which could help us distinguish better between the curves and thus linewidths.

(A) Spontaneous

(B) Seeded

Legend:
- HaPrP(23-230)M138R1_spon_1:0
- HaPrP(108-144)A113R1
- HaPrP(108-144)A118R1
- HaPrP(108-144)V121R1
- HaPrP(108-144)L125R1
- HaPrP(108-144)M129R1
- HaPrP(108-144)M134R1
- HaPrP(108-144)M138R1

Magnetic field (Gauss)
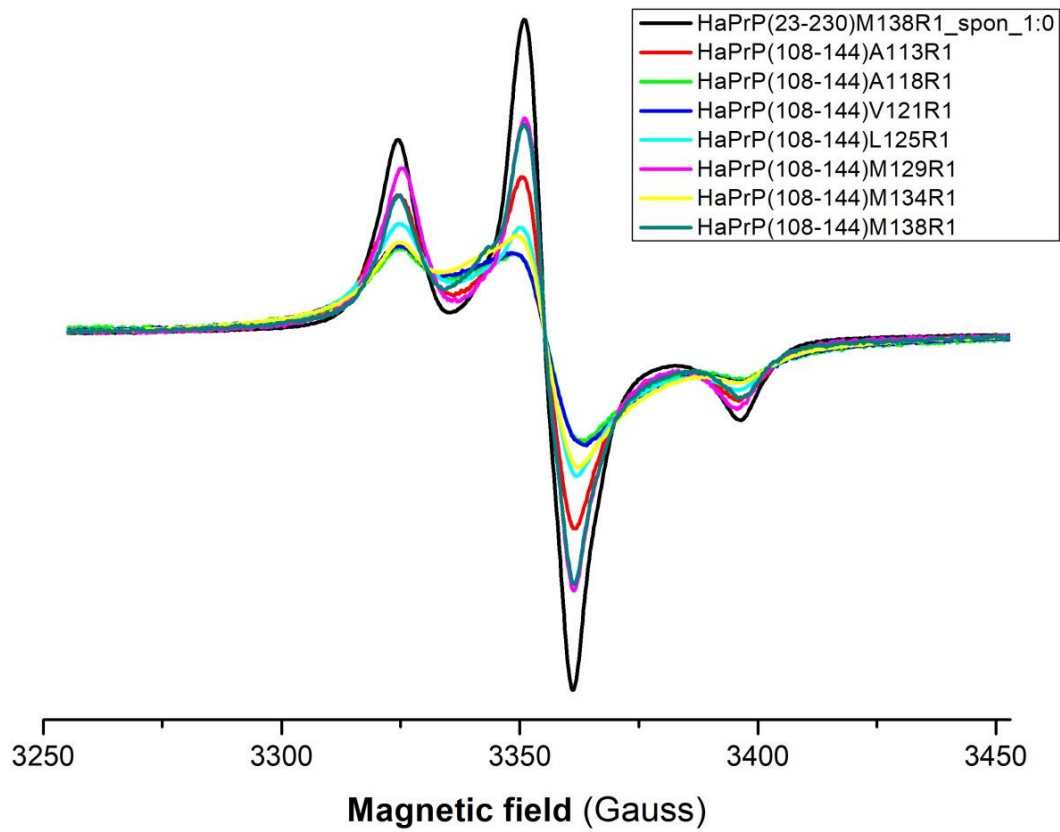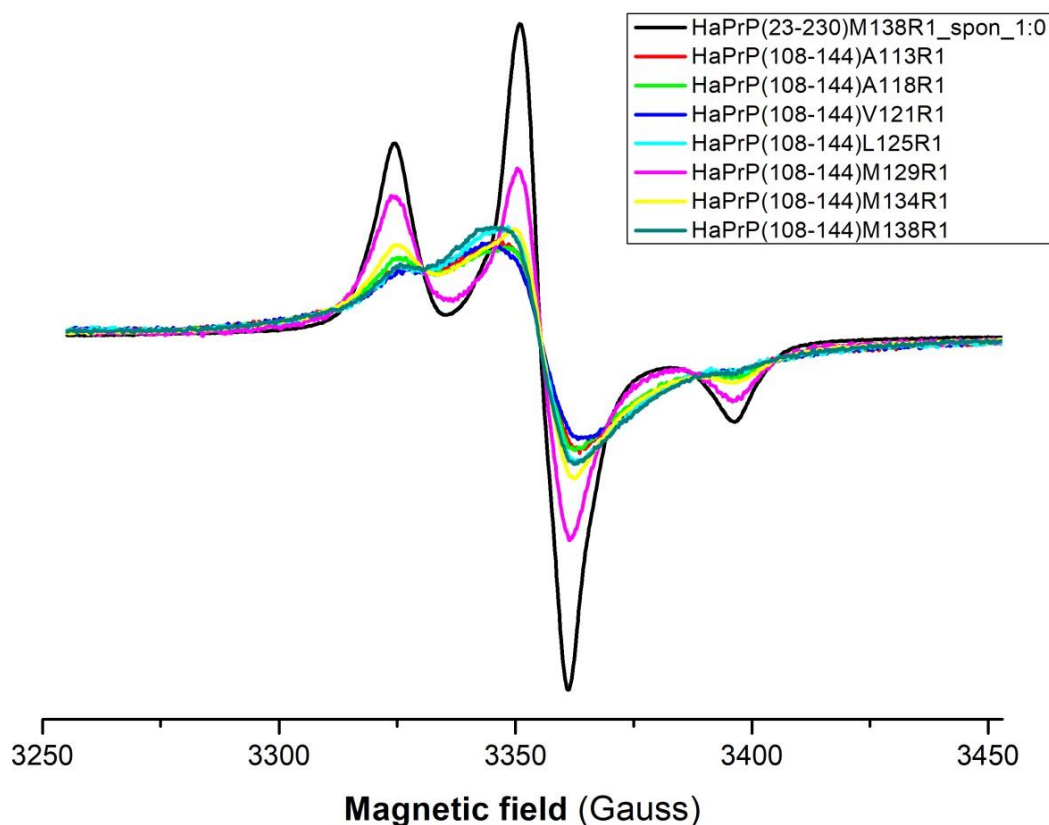
Figure 5.5 Comparison of ESR spectrograms between different mutants on spontaneously formed fibrils and seeded fibrils.
X-band continuous wave (cw)-ESR was measured at an operating frequency of ~9.42 GHz at the temperature of 200K. The sweep width of the measurement was 200 G, ranging from 3250 to 3450 Gauss.

From the spectrograms, the linewidths between different mutants of spontaneously formed fibrils could be ranked as A118R1 ≈ V121R1 > M134R1 ≈ L125R1 > A113R1 > M129R1 ≈ M138R1, and the linewidths between different mutants of seeded fibrils were all relatively broadened except for M129R1. Since the data from seeding assay were more convincing for structural elucidation, it was suggested that the distances between spins in each mutant were all very close except for M129R1.

108

We now had measured all ESR from the amyloid fibrils formed from various ways (spontaneous or seeded) and mutant sites (seven in total). The results of ESR data would be discussed and compared based on previous fluorescence spectra in the following chapter, aiming to see through the possible mechanism of prion fibril formation.

110
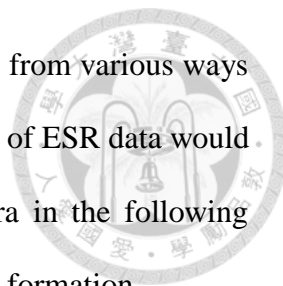
Chapter 6 Discussion
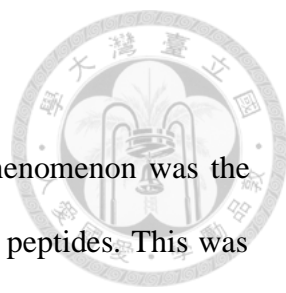
6.1 Overview

In the research of prion protein amyloidogenesis, an important question was the mechanism of conformational change from the α-dominant cellular PrP^C to the β-rich PrP^{Sc}, and many possibilities had been issued to explain this phenomenon. It was reported that transmission of prion aggregation between species has transmission barrier, which resulted from the slightly differences in amino acid sequences. Yet how these sequence differences generated significantly different seeding efficiency still remains unknown.

In this thesis, we tried to elucidate the relative proximity between the same residues of different hamster prion peptides 108-144 within the amyloid fibril structure by using spin-labeled cysteine-mutating peptides and ESR spectroscopy. The fibrils were generated *in vitro* to mimic the production of PrP^{Sc} structures *in vivo*. TEM and ThT binding assay was also used to evaluate the generation and kinetics of amyloid fibril formation. By comparing the kinetics, morphology and spin-spin interaction of the fibrils, we aimed to have a deeper insight into where the amyloid core might be within the fibril structure of prion peptides.

111

6.2   Sample preparation (Chapter 3)

In the process of sample preparation, the most unexpected phenomenon was the appearance of white precipitates during MTSSL labeling on mutant peptides. This was once reported in the labeling process of prion peptide on H140C in Jenny's thesis, but it was stated that the addition of denaturant like GdnHCl in the labeling mixture could help to lessen the amount of the precipitates. This approach turned out to be ineffective, and other solvents like DMSO couldn't help dissolve the precipitates as well. Surprisingly, certain percent of B buffer mixed with A buffer could solve this problem, and the percent was not far away from the gradients when unlabeled peptides eluted out in HPLC purification. Generally, it was thought that the amount of the precipitates was related to the peptide concentration in the labeling experiment, for too much peptide could exceed the solubility of mutant peptides in MOPS buffer. It was not certain still that whether the appearance of precipitates would lead to different results of structural elucidation. It might be regarded that the formation of precipitate could be reversed by dissolving it into the appropriate solvent, but the peptides in the solution could have formed larger units than monomers such as oligomers or proto-fibrils that could not be observed by naked eyes. Further check should be done by putting these precipitated samples to be analyzed by other tools. For example, TEM could help visualize whether these peptides had already formed larger units. Once this phenomenon had occurred, monomers must be further separated from these formations by techniques like analytical ultracentrifugation (AUC).

Another interesting issue arose when some of the mutant peptides were found to be oxidized in the prolife of MALDI-TOF MS data (Figure A.8). In those MS spectra, two to three oxidized products were found in either unlabeled or spin-labeled samples,

112
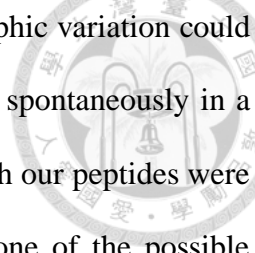
leading peaks of serial oxidation with intervals of 16 Dalton. The biggest possible source of these oxidized products was ought to be methionine oxidation, which turned the thiol groups on the side chains of methionine residue into sulfinyl (one oxygen atom) or even sulfonyl (two oxygen atoms) groups, and up to six methionine residues were present in our peptide sequences and thus possible to be modified. There were several possible reasons for the oxidation of the peptides, including storing the peptide in solution in 4°C for too long, or some factors of the labeling process including rotating speed, temperature, reaction time and space of air in the Falcon tube. Since oxidized peptides have more oxygen atoms on their side chains and might arouse concerns of fibril structural variance, they were not used for the following experiments including fibril formation and ESR measurement.

113

6.3 Amyloid fibril formation (Chapter 4)

In this part of experiment, the biggest difference of conditions between the full-length protein and peptide fibril formation was the presence of denaturants (Yang, Lo et al. 2015). Unlike the full-length protein fibril growth, amyloid fibril formation from peptides did not require denaturants like GdnHCl or urea for structure unfolding. This had given the advantage of our study since the conditions were closer to physiological environment, and the resulting fibril structure would have more possibilities to be closer to natural conformation. Since peptide structural elucidation could give a clearer look at the structural features of protein local region, some previous studies had also turned to target on peptide as a comparison of related protein structural analysis (Lin, Chao et al. 2010, Cheng, Tsai et al. 2011).

In the results of fluorescence spectra, it was obvious to see that the fibrils growth varied between mutants. For spontaneous fibril formation, most of the mutants showed gradually increased and hyperbolic growth instead of sigmoidal pattern like the wild-type fibrils. For seeded fibril formation, the mutants of A113R1, A118R1, V121R1 and M138R1 showed the pattern of growth more like the wild-type fibrils featuring the instant increase of fluorescence intensity; Mutants of L125R1, M129R1, and M134R1 showed the pattern of growth not so much different with spontaneous fibril formation. All of the results above had given some clues that the spin-labeling had led to certain structural changes during the formation of amyloid fibrils, and seeding assay could help in some of the mutants. However, fibril growth could not be recovered to wild-type-like pattern in some of the mutants, showing that these mutant sites could be unusually important. Among these sites, M129 exhibited the most obvious pattern change. According to the previous study, though the polymorphism of codon 129 did not change

the efficiency of conversion to the β-rich conformation, the polymorphic variation could have an impact on the ability of the protein to form amyloid fibrils spontaneously in a partially denatured conformation (Lewis, Tattum et al. 2006). Though our peptides were not in the same partially denatured condition, this could still be one of the possible reasons why M129 exhibited the most different patterns of fibril growth.
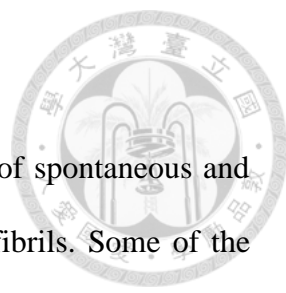
The hyperbolic and sigmoidal patterns of fibril growth had a resemblance to the enzymatic models of Michaelis-Menten kinetics and kinetics of allosteric enzymes respectively. In the former, the model features the formation of enzyme-substrate complexes, which would accelerate the reaction and reach to a maximal velocity when the substrate concentration is increased. In the latter, the model is based on the fact that the binding of substrate to an active site could change the properties of other active sites in the same enzyme molecule, which makes the binding to be cooperative. One of the examples of cooperative binding is the hemoglobin tetramer binding to oxygen molecules. Despite the pattern resemblance, it should be noted that in our fluorescence curves, the change fluorescence intensity was time-dependent, but in those enzymatic models the change of reaction velocity was substrate concentration-dependent, which would lead to different explanations to the reaction kinetics.

Finally, in the experiments of seeding assay, there was also a concern of whether the seed quantity was enough to trigger immediate fibril growth or not. The seeds were quantified based on absolute amount of mole in each samples for the convenience of calculation, but different concentration of peptides might require different amounts of seeds to grow into fibrils in the same rate. Generally, the less the peptide was in the solution, the more seeds were needed to complement the nuclei for significant growth. Thus, though the seeding efficiency might be mutant-dependent, for those mutants

115

showing very slow or no growth of fibrils, corresponding higher amounts of seed should

be used for further tests.

6.4　TEM & ESR spectroscopy (Chapter 5)

In the observation of fibril morphology by TEM, both results of spontaneous and seeded fibril formation exhibited presence of rod-shaped amyloid fibrils. Some of the fibrils were found to be in single stick or bundle, and others were found in shrubs. In addition, it was indicated that the rate of fibril growth might influence the resulting morphology, and we already found some proofs in seeded fibril formation and the fibrils grown in sodium acetate buffer (Figure A.7). Interestingly, though the morphology of the fibrils grown in sodium acetate buffer exhibited shapes of thinner stick, after second trial of spontaneous fibril formation it was found that the kinetics of fibril growth in this buffer was not that slow and unapparent as what Figure 4.1 had shown (data not shown), which requires further repeats of experiments and observation to see what happened in a clearer way.
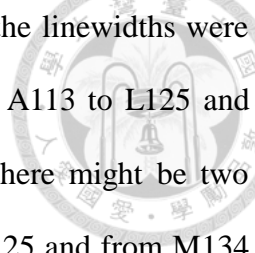
The quality of the TEM images became an issue when quality of images from different samples appeared to be varied. In the images of wild-type seed, the classical negative staining, featuring white fibrils accompanied by dark background, was more obvious than any other peptide sample (Figure 5.2). The biggest difference between seed and other samples was the size of the fibrils, so whether this factor would affect the effect of negative staining was concerned. Results could be compared previous ones by sonicating the mutant fibrils before negative staining and TEM observation.

The width of the both spontaneously formed and seeded fibrils was also roughly examined based on the scale bar given in the image, and mostly the images of 100 nm were used for better precision. It was found that the approximate range of fibrils width falls from 10 to 30 nm, which is quite a wide range. The range also depended on the clearness of the images and the composition of the fibril bundles. If the contours of the

117

fibrils appeared to be clear and the fibrils were in single stick, the width usually falls in the range of 10 to 15 nm. Sometimes the contours were vaguer and the fibrils seemed to assemble in bundles, and the width usually falls in the range of 20 to 30 nm. Usually, the accurate length and width of amyloid fibrils are hard to quantify through TEM images due to too many factors of randomness, so we would still put our main focus in the characteristic dimension of analysis.

In the ESR data, the spectrograms from different mutants were overlay and compared between spontaneous and seeded fibrils. Also, ESR results from the amyloid fibrils formed of full-length hamster protein were compared with our data. Mutants of A113R1, M134R1 and M138R1 exhibited relative sharp shape of curves, while L125R1 and M129R1 showed broader curve compared to our data (Figure A.9). The variance of result between full-length protein and peptide might result from the possible fact that amyloid core might locate differently based on the total length of the monomer, for longer monomers could have more options of amyloid core formation. Further investigation could be done by seeding between spin-labeled peptide and full-length protein from the same hamster prion protein.

In comparison of ESR spectrograms between spontaneously formed and seeded fibrils, it was found that mutants of A113R1 and M138R1 had the biggest changes from spontaneous to seeded, both of which showing increased linewidths. It was suggested that these changes were due to the marginalized location of their mutated sites from the center of the peptide sequence. However, in the presence of seeds, they have templates to assemble and aggregate into tighter structure, leading to broadened ESR spectra. The changes of ESR spectra were not so obvious in other mutants whose mutated sites were more central than A113 and M138.

118

In the ESR result of seeded fibrils, it was found that most of the linewidths were increased except for mutant M129R1. Since the ESR spectra from A113 to L125 and from M134 to M138 were all broad in a row, we assumed that there might be two amyloid cores within the peptide 108-144, ranging from A113 to L125 and from M134 to M138 respectively. The former amyloid core was assumed to be related to the local sequence that was all composed of hydrophobic residues (from 112 to 127 the sequence is MAGAAAAGAVVGGLGG), bring the high hydrophobicity and tendency to aggregation in this region. Between these two cores the residues around M129 stood out as a key region, which might be loose in structure but packed between the two cores. Schematic representations of our proposed model were shown in Figure 6.1 as below to illustrate the possible conformations of hamster peptide amyloid fibrils.

The previous models built by MD simulations in shorter prion peptides elucidated by either solid-state or hydrogen-exchange NMR were all showing structures rich in β-sheet, though with different details such as strand parallelism, side-chain orientation, and presence of kink due to certain residues like proline (Kuwata, Matumoto et al. 2003, Lee, Mou et al. 2008, Walsh, Simonetti et al. 2009, Lin, Chao et al. 2010, Cheng, Tsai et al. 2011). In our models, we suggested that there might be a loop and thus bending between the two proposed amyloid cores, which wasn't mentioned in those previous reported shorter peptides.

(A) Parallel—no bending

(B) Parallel—bending

(C) Anti-parallel—no bending

(D) Anti-parallel—bending
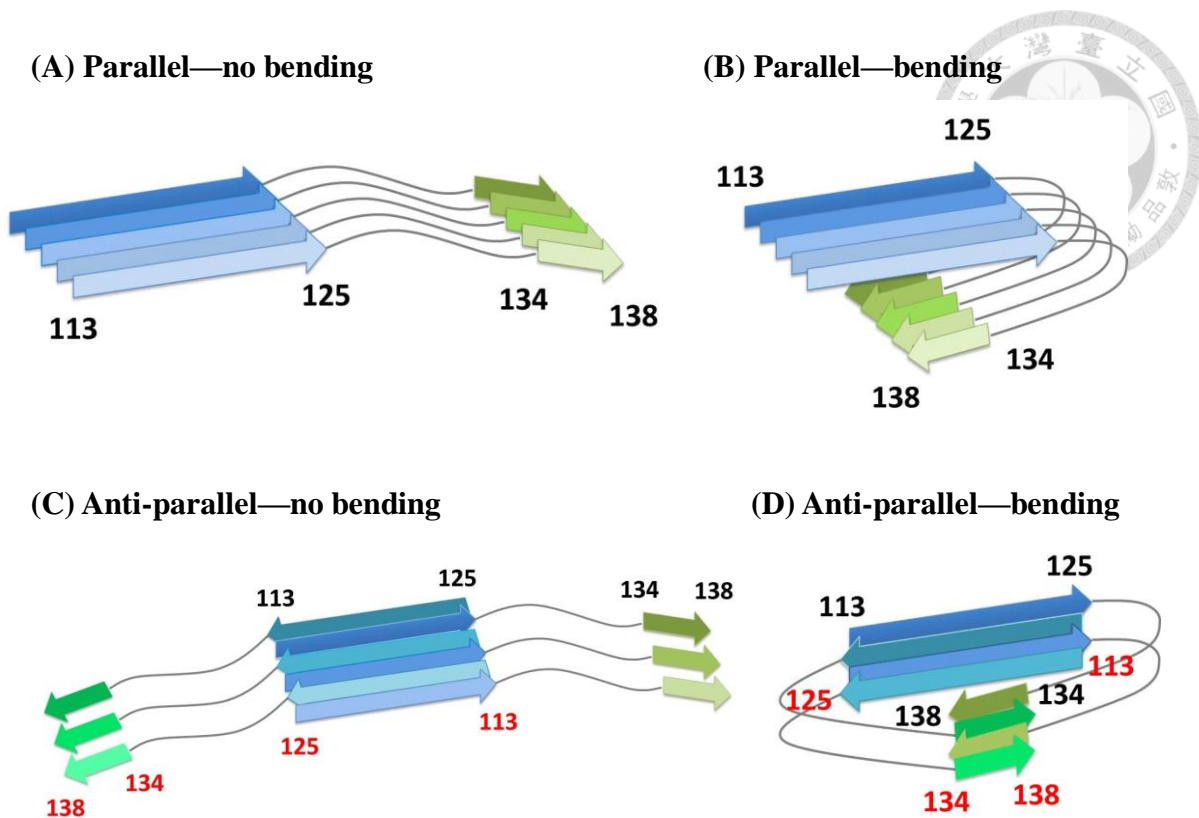
Figure 6.1 Schematic representations of the proposed model based on the ESR results.

In the graphs shown above, four different kinds of structural models were shown to simulate possible conformations when hamster prion peptides 108-144 form fibrils. Models of parallel alignment were shown in (**A**) and (**B**), and anti-parallel alignment in (**C**) and (**D**), which included the possibility of bending respectively. Different strands were labeled with colors of various shades for clearer visualization. Numbers of strands shown here were only for graphic illustration and do not represent the real conditions.

Finally, spin dilution using wild-type peptides were carried out on mutants A113R1 and M134R1, originally aiming to deconvolute the spin-spin distance through fitting. In the results of ThT binding assay, the curve pattern of A113R1 and M134R1 were somewhat different after spin dilution (Figure A.10). The curve of 1:1 dilution in A113R1 was similar to the one of 1:0, and the curve went up faster by the presence of wild-type monomers. However, in the case of M134R1, the curve patterns between 1:1 and 1:0 were not similar since the curve of 1:1 went up but the one of 1:0 stayed still. In

this condition, we could not eliminate the possibility that the increase of curve in 1:1 dilution was due to the fibrils formed of wild-type monomers, and this was also the reason why 1:1 sample of M134R1 were not sent for ESR measurement (Figure A.11). Further structural elucidation would be done by spin dilution on other mutants in appropriate concentration, as well as on samples of spin-labeled double-mutated peptides.
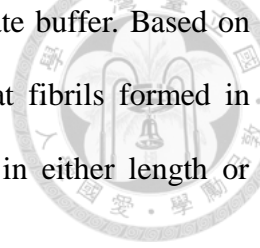
Chapter 7   Conclusions and Future works
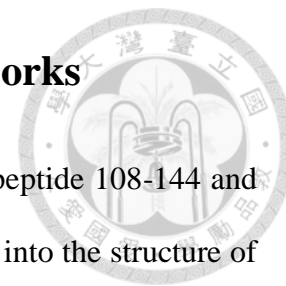
In this study, we had used spin-labeled mutant hamster prion peptide 108-144 and ESR spectroscopy to take the first step of site-specific investigation into the structure of prion amyloid fibrils. In the part of sample preparation, seven mutant prion peptides of different mutated sites as well as wild-type peptide were synthesized by solid-phase peptide synthesis. After that, appropriate gradients were found to be used in purifying the peptides by reverse-phased HPLC. The peptides were then spin-labeled with MTSSL in MOPS buffer condition, and certain mixture of A buffer and B buffer were found to dissolve the white peptide precipitates.

Secondly, the conversion from α-helix-rich natural prion peptide (PrP^C) intoβ-sheet-rich amyloid fibrils (PrP^{Sc}) was performed *in vitro* with appropriate fibril formation buffer. Spontaneous fibril formation was firstly tested by different concentration of peptide monomer through ThT binding assay, and the resulting spectra showed slowly gradual increase of fluorescence intensity that were diverse with the pattern of wild-type. Next, seeding assay was carried out by adding seeds into the fibril formation samples, and most of the mutants exhibited accelerated fibril growth though in different extent. M129R1 was the mutant that exhibited the least extent of fibril growth in both spontaneous and seeded fibril formation, which had implicated the importance of this location in the structure.
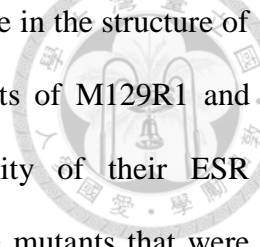
The spin-labeled amyloid fibrils were further examined by TEM for their morphology. Under the scope of TEM, rod-shaped fibrils in bundles or thickets were found in both spontaneous and seeded samples, but fibrils formed form seeding tended to be more fragmented in general. In addition, fibrils formed in different buffer might exhibit various morphologies. For example, the fibrils formed in sodium acetate buffer

showed thinner shape compared to the fibrils from sodium phosphate buffer. Based on the different growth rates in the cases above, it was assumed that fibrils formed in different rate would contribute to slightly different morphologies in either length or thickness.

Finally, the spin-labeled fibrils were analyzed with ESR spectroscopy for their spin-spin interaction, and the possible locations of amyloid core were elucidated. Between the results of spontaneously formed and seeded fibrils, the mutants A113R1 and M138R1 had the largest extent of linewidth broadening. In the spectrograms of spontaneously formed fibrils, the linewidths could be ranked as A118R1 ≈ V121R1 > M134R1 ≈ L125R1 > A113R1 > M129R1 ≈ M138R1, and the curves of seeded fibrils were all relatively broadened except for M129R1. Such big changes were attributed to the fact that the region near M129 might be packed between two amyloid cores, which were around A113-L125 and M134-M138, while remaining loose in structure, and the significance of this residue was confirmed by previous results of ThT binding assay.

The scope of our study was mostly related to Howard's thesis, both of which were based on the previous study focusing on seeding efficiency of different segment in mouse prion protein (Chatterjee, Lee et al. 2013). Our results were partially consistent with Howard's results that the potential amyloid core region we found between A113 and L125 could correspond to the segment of 108-127, which had the ability of mutual seeding with full-length protein. As for the segment between 128-144, though Howard's thesis indicated that there was no seeding capacity, our results showed that there might be a second, shorter amyloid core region near the sequence from 134 to 138. Still, the longer length and higher hydrophobicity of the former amyloid core segment might make it a first choice for forming amyloid structure.

Beyond our study, there are still much to explore and investigate in the structure of prion proteins and peptides in the future. First, the seeding effects of M129R1 and M134R1 should be further checked to establish the credibility of their ESR spectrograms since their seeding effects were not obvious. For the mutants that were hard to grow fibrils, like M129R1 and M134R1, the concentration of salts and environmental temperature could be altered for further tests. Second, more single-labeled mutant peptides carrying different single mutated site are needed to make a clearer mapping of the whole peptide, especially on sites near the possible core regions 113-125 and 134-138. H111C and F141C are presently picked out for further experiments, which reside by the edges of our proposed amyloid cores. In addition, double labeling on a single peptide should be tested to see the spin-spin interaction within the same peptide, exploring if the peptides had bending into certain conformation while aggregating. Pairs of mutants like A113C with L125C and M134C with M138C are presently chosen for further experiments. To investigate deeper in the differences between spontaneously formed and seeded fibrils, other tools like FT-IR should also be put into use other than TEM in order to distinguish the structures between them. Finally, the curves drawn from fluorescence spectra should be repeated in triplication with error bar added, and fluorescence data points can be fitted to the sigmoidal and hyperbolic curve patterns using applicable equations by obtaining kinetic parameters for aggregation (Alvarez-Martinez, Fontes et al. 2011).

References

Aguzzi, A. and M. Polymenidou (2004). "Mammalian prion biology: One century of evolving concepts." Cell **116**(2): 313-327.

Aguzzi, A., C. Sigurdson and M. Heikenwaelder (2008). "Molecular mechanisms of prion pathogenesis." Annual Review of Pathology: Mechanisms of Disease **3**(1): 11-40.

Alper, T., W. A. Cramp, D. A. Haig and M. C. Clarke (1967). "Does the agent of scrapie replicate without nucleic acid ?" Nature **214**: 764.

Alvarez-Martinez, M.-T., P. Fontes, V. Zomosa-Signoret, J.-D. Arnaud, E. Hingant, L. Pujo-Menjouet and J.-P. Liautard (2011). "Dynamics of polymerization shed light on the mechanisms that lead to multiple amyloid structures of the prion protein." Biochimica et Biophysica Acta (BBA) - Proteins and Proteomics **1814**(10): 1305-1317.

Apostol, M. I., J. J. W. Wiltzius, M. R. Sawaya, D. Cascio and D. Eisenberg (2011). "Atomic structures suggest determinants of transmission barriers in mammalian prion disease." Biochemistry **50**(13): 2456-2463.

Baskakov, I. V., C. Aagaard, I. Mehlhorn, H. Wille, D. Groth, M. A. Baldwin, S. B. Prusiner and F. E. Cohen (2000). "Self-assembly of recombinant prion protein of 106 residues." Biochemistry **39**(10): 2792-2804.

Bolton, D., M. McKinley and S. Prusiner (1982). "Identification of a protein that purifies with the scrapie prion." Science **218**(4579): 1309-1311.

Castle, A. R. and A. C. Gill (2017). "Physiological functions of the cellular prion protein." Frontiers in Molecular Biosciences **4**(19).

Caughey, B. W., A. Dong, K. S. Bhat, D. Ernst, S. F. Hayes and W. S. Caughey (1991). "Secondary structure analysis of the scrapie-associated protein PrP 27-30 in water by infrared spectroscopy." Biochemistry **30**(31): 7672-7680.

Chatterjee, B., C.-Y. Lee, C. Lin, E. H. L. Chen, C.-L. Huang, C.-C. Yang and R. P.-Y. Chen (2013). "Amyloid core formed of full-length recombinant mouse prion protein involves sequence 127–143 but not sequence 107–126." PLOS ONE **8**(7): e67967.

127

Cheng, H.-M., Y. C. Huang William, W. T. Tsai Tim, Y. Mou, H. Chao John Chin and C. C. Chan Jerry (2013). "Depletion of water molecules near the end stage of steric zipper formation." Journal of the Chinese Chemical Society **60**(7): 794-800.

Cheng, H.-M., T. W. T. Tsai, W. Y. C. Huang, H.-K. Lee, H.-Y. Lian, F.-C. Chou, Y. Mou and J. C. C. Chan (2011). "Steric zipper formed by hydrophobic peptide fragment of Syrian hamster prion protein." Biochemistry **50**(32): 6815-6823.

Chiti, F. and C. M. Dobson (2006). "Protein Misfolding, Functional Amyloid, and Human Disease." Annual Review of Biochemistry **75**(1): 333-366.

Choi, J.-K., I. Cali, K. Surewicz, Q. Kong, P. Gambetti and W. K. Surewicz (2016). "Amyloid fibrils from the N-terminal prion protein fragment are infectious." Proceedings of the National Academy of Sciences of the United States of America **113**(48): 13851-13856.

Chuang, C.-C., T.-Y. Liao, E. H. L. Chen and R. P.-Y. Chen (2013). "How do amino acid substitutions affect the amyloidogenic properties and seeding efficiency of prion peptides." Amino Acids **45**(4): 785-796.

Cobb, N. J., F. D. Sönnichsen, H. Mchaourab and W. K. Surewicz (2007). "Molecular architecture of human prion protein amyloid: A parallel, in-register β-structure." Proceedings of the National Academy of Sciences of the United States of America **104**(48): 18946-18951.

Cohen, S. I. A., S. Linse, L. M. Luheshi, E. Hellstrand, D. A. White, L. Rajah, D. E. Otzen, M. Vendruscolo, C. M. Dobson and T. P. J. Knowles (2013). "Proliferation of amyloid-β42 aggregates occurs through a secondary nucleation mechanism." Proceedings of the National Academy of Sciences **110**(24): 9758-9763.

Collinge, J. (2001). "Prion diseases of humans and animals: Their causes and molecular basis." Annual Review of Neuroscience **24**(1): 519-550.

Damo, S. M., A. H. Phillips, A. L. Young, S. Li, V. L. Woods and D. E. Wemmer (2010). "Probing the conformation of a prion protein fibril with hydrogen exchange." Journal of Biological Chemistry **285**(42): 32303-32311.

Dearmond, S. J., M. P. McKinley, R. A. Barry, M. B. Braunfeld, J. R. McColloch and S. B. Prusinert (1985). "Identification of prion amyloid filaments in scrapie-infected brain." Cell **41**(1): 221-235.

Dobson, C. M. (2003). "Protein folding and misfolding." Nature **426**: 884.

Donne, D. G., J. H. Viles, D. Groth, I. Mehlhorn, T. L. James, F. E. Cohen, S. B. Prusiner, P. E. Wright and H. J. Dyson (1997). "Structure of the recombinant full-length hamster prion protein PrP(29–231): The N terminus is highly flexible." Proceedings of the National Academy of Sciences of the United States of America **94**(25): 13452-13457.

Eichner, T. and Sheena E. Radford (2011). "A diversity of assembly mechanisms of a generic amyloid fold." Molecular Cell **43**(1): 8-18.

Freire, S., M. H. de Araujo, W. Al-Soufi and M. Novo (2014). "Photophysical study of Thioflavin T as fluorescence marker of amyloid fibrils." Dyes and Pigments **110**: 97-105.

Gajdusek, D. C., C. J. Gibbs jun and M. Alpers (1966). "Experimental transmission of a kuru-like syndrome to chimpanzees." Nature **209**: 794.

Gasset, M., M. A. Baldwin, D. H. Lloyd, J. M. Gabriel, D. M. Holtzman, F. Cohen, R. Fletterick and S. B. Prusiner (1992). "Predicted alpha-helical regions of the prion protein when synthesized as peptides form amyloid." Proceedings of the National Academy of Sciences of the United States of America **89**(22): 10940-10944.

Griffith, J. S. (1967). "Nature of the scrapie agent: self-replication and scrapie." Nature **215**: 1043.

Grigoryants, V. M., A. V. Veselov and C. P. Scholes (2000). "Variable velocity liquid flow EPR applied to submillisecond protein folding." Biophysical Journal **78**(5): 2702-2708.

Groveman, B. R., M. A. Dolan, L. M. Taubner, A. Kraus, R. B. Wickner and B. Caughey (2014). "Parallel in-register intermolecular β-sheet architectures for prion-seeded prion protein (PrP) amyloids." The Journal of Biological Chemistry **289**(35): 24129-24142.

Haire, L. F., S. M. Whyte, N. Vasisht, A. C. Gill, C. Verma, E. J. Dodson, G. G. Dodson and P. M. Bayley (2004). "The crystal atructure of the globular domain of sheep prion protein." Journal of Molecular Biology **336**(5): 1175-1183.

Helmus, J. J., K. Surewicz, P. S. Nadaud, W. K. Surewicz and C. P. Jaroniec (2008). "Molecular conformation and dynamics of the Y145Stop variant of human prion protein in amyloid fibrils." Proceedings of the National Academy of Sciences of the United States of America **105**(17): 6284-6289.

Helmus, J. J., K. Surewicz, W. K. Surewicz and C. P. Jaroniec (2010). "Conformational flexibility of Y145Stop human prion protein amyloid fibrils probed by solid-state nuclear magnetic resonance spectroscopy." Journal of the American Chemical Society **132**(7): 2393-2403.

Henderson, R. (2004). "Realizing the potential of electron cryo-microscopy." Quarterly Reviews of Biophysics **37**: 3-13.

Ironside, J. W. (2012). "Variant Creutzfeldt-Jakob disease: an update." Folia Neuropathologica **50**(1): 50-56.

Jarrett, J. T. and P. T. Lansbury (1993). "Seeding "one-dimensional crystallization" of amyloid: A pathogenic mechanism in Alzheimer's disease and scrapie?" Cell **73**(6): 1055-1058.

Jones, E. M. and W. K. Surewicz (2005). "Fibril conformation as the basis of species- and strain-dependent seeding specificity of mammalian prion amyloids." Cell **121**(1): 63-72.

Khurana, R., C. Coleman, C. Ionescu-Zanetti, S. A. Carter, V. Krishna, R. K. Grover, R. Roy and S. Singh (2005). "Mechanism of thioflavin T binding to amyloid fibrils." Journal of Structural Biology **151**(3): 229-238.

King, D. S., C. G. Fields and G. B. Fields (1990). "A cleavage method which minimizes side reactions following Fmoc solid phase peptide synthesis." International Journal of Peptide and Protein Research **36**(3): 255-266.

Knaus, K. J., M. Morillas, W. Swietnicki, M. Malone, W. K. Surewicz and V. C. Yee (2001). "Crystal structure of the human prion protein reveals a mechanism for oligomerization." Nature Structural Biology **8**: 770.

Kneipp, J., L. M. Miller, M. Joncic, M. Kittel, P. Lasch, M. Beekes and D. Naumann (2003). "In situ identification of protein structural changes in prion-infected tissue." Biochimica et Biophysica Acta (BBA) - Molecular Basis of Disease **1639**(3): 152-158.

Koch, M., P. Vachette and D. I Svergun (2003). "Small-angle scattering: A view on the properties, structures and structural changes of biological macromolecules in solution." Quarterly Reviews of Biophysics **36**: 147-227.

Krebs, M. R. H., E. H. C. Bromley and A. M. Donald (2005). "The binding of thioflavin-T to amyloid fibrils: localisation and implications." Journal of Structural Biology **149**(1): 30-37.

Kundu, B., N. R. Maiti, E. M. Jones, K. A. Surewicz, D. L. Vanik and W. K. Surewicz (2003). "Nucleation-dependent conformational conversion of the Y145Stop variant of human prion protein: Structural clues for prion propagation." Proceedings of the National Academy of Sciences of the United States of America **100**(21): 12069-12074.

Kuwata, K., T. Matumoto, H. Cheng, K. Nagayama, T. L. James and H. Roder (2003). "NMR-detected hydrogen exchange and molecular dynamics simulations provide structural insight into fibril formation of prion protein fragment 106–126." Proceedings of the National Academy of Sciences of the United States of America **100**(25): 14790-14795.

Laurent, M. (1996). "Prion diseases and the 'protein only' hypothesis: a theoretical dynamic study." Biochemical Journal **318**(Part 1): 35-39.

Lee, L. Y. L. and R. P.-Y. Chen (2007). "Quantifying the sequence-dependent species barrier between hamster and mouse prions." Journal of the American Chemical Society **129**(6): 1644-1652.

Lee, S.-W., Y. Mou, S.-Y. Lin, F.-C. Chou, W.-H. Tseng, C.-H. Chen, C.-Y. D. Lu, S. S. F. Yu and J. C. C. Chan (2008). "Steric Zipper of the Amyloid Fibrils Formed by Residues 109–122 of the Syrian Hamster Prion Protein." Journal of Molecular Biology **378**(5): 1142-1154.

Lewis, P. A., M. H. Tattum, S. Jones, D. Bhelt, M. Batchelor, A. R. Clarke, J. Collinge and G. S. Jackson (2006). "Codon 129 polymorphism of the human prion protein influences the kinetics of amyloid formation." Journal of General Virology **87**(8): 2443-2449.

Lin, N.-S., J. C.-H. Chao, H.-M. Cheng, F.-C. Chou, C.-F. Chang, Y.-R. Chen, Y.-J. Chang, S.-J. Huang and J. C. C. Chan (2010). "Molecular structure of amyloid fibrils formed by residues 127 to 147 of the human prion protein." Chemistry – A European Journal **16**(18): 5492-5499.

Lu, X., P. L. Wintrode and W. K. Surewicz (2007). "β-Sheet core of human prion protein amyloid fibrils as determined by hydrogen/deuterium exchange." Proceedings of the National Academy of Sciences of the United States of America **104**(5): 1510-1515.

Mackenzie, G. and R. Will (2017). "Creutzfeldt-Jakob disease: recent developments." F1000Research **6**: 2053.

Makarava, N., G. G. Kovacs, O. Bocharova, R. Savtchenko, I. Alexeeva, H. Budka, R. G. Rohwer and I. V. Baskakov (2010). "Recombinant prion protein induces a new transmissible prion disease in wild-type animals." Acta Neuropathologica **119**(2): 177-187.

Margittai, M. and R. Langen (2004). "Template-assisted filament growth by parallel stacking of tau." Proceedings of the National Academy of Sciences of the United States of America **101**(28): 10278-10283.

McKinley, M. P. and S. B. Prusiner (1986). Biology and structure of scrapie prions. International Review of Neurobiology. J. R. Smythies and R. J. Bradley, Academic Press. **28:** 1-57.

Millhauser, G. L. (2007). "Copper and the prion protein: methods, structures, function, and disease." Annual Review of Physical Chemistry **58**(1): 299-320.

Muramoto, T., M. Scott, F. E. Cohen and S. B. Prusiner (1996). "Recombinant scrapie-like prion protein of 106 amino acids is soluble." Proceedings of the National Academy of Sciences of the United States of America **93**(26): 15457-15462.

Naiki, H., T. Okoshi, D. Ozawa, I. Yamaguchi and K. Hasegawa (2016). "Molecular pathogenesis of human amyloidosis: Lessons from β2-microglobulin-related amyloidosis." Pathology International **66**(4): 193-201.

Nick, P. C., V. Felix, F. Lanette, G. Gerald and G. Theronica (1995). "How to measure and predict the molar absorption coefficient of a protein." Protein Science **4**(11): 2411-2423.

Oesch, B., D. Westaway, M. Wälchli, M. P. McKinley, S. B. H. Kent, R. Aebersold, R. A. Barry, P. Tempst, D. B. Teplow, L. E. Hood, S. B. Prusiner and C. Weissmann (1985). "A cellular gene encodes scrapie PrP 27-30 protein." Cell **40**(4): 735-746.

Orrú, C. D., J. Yuan, B. S. Appleby, B. Li, Y. Li, D. Winner, Z. Wang, Y.-A. Zhan, M. Rodgers, J. Rarick, R. E. Wyza, T. Joshi, G.-X. Wang, M. L. Cohen, S. Zhang, B. R. Groveman, R. B. Petersen, J. W. Ironside, M. E. Quiñones-Mateu, J. G. Safar, Q. Kong, B. Caughey and W.-Q. Zou (2017). "Prion seeding activity and infectivity in skin samples from patients with sporadic Creutzfeldt-Jakob disease." Science Translational Medicine **9**(417): pii: eaam7785.

Pan, K. M., M. Baldwin, J. Nguyen, M. Gasset, A. Serban, D. Groth, I. Mehlhorn, Z. Huang, R. J. Fletterick and F. E. Cohen (1993). "Conversion of alpha-helices into beta-sheets features in the formation of the scrapie prion proteins." Proceedings of the National Academy of Sciences of the United States of America **90**(23): 10962-10966.

Pastore, A. and A. Zagari (2007). "A structural overview of the vertebrate prion proteins." Prion **1**(3): 185-197.

Prusiner, S. B. (1982). "Novel proteinaceous infectious particles cause scrapie." Science **216**(4542): 136-144.

Prusiner, S. B. (1991). "Molecular biology of prion diseases." Science **252**(5012): 1515-1522.

Prusiner, S. B. (1998). "Prions." Proceedings of the National Academy of Sciences of the United States of America **95**(23): 13363-13383.

Prusiner, S. B., M. P. McKinley, K. A. Bowman, D. C. Bolton, P. E. Bendheim, D. F. Groth and G. G. Glenner (1983). "Scrapie prions aggregate to form amyloid-like birefringent rods." Cell **35**(2, Part 1): 349-358.

Puoti, G., A. Bizzi, G. Forloni, J. G. Safar, F. Tagliavini and P. Gambetti (2012). "Sporadic human prion diseases: molecular insights and diagnosis." The Lancet Neurology **11**(7): 618-628.

Riek, R. and D. S. Eisenberg (2016). "The activities of amyloids from a structural perspective." Nature **539**: 227.

Riek, R., S. Hornemann, G. Wider, M. Billeter, R. Glockshuber and K. Wüthrich (1996). "NMR structure of the mouse prion protein domain PrP(121–231)." Nature **382**: 180.

Rudd, P. M., T. Endo, C. Colominas, D. Groth, S. F. Wheeler, D. J. Harvey, M. R. Wormald, H. Serban, S. B. Prusiner, A. Kobata and R. A. Dwek (1999). "Glycosylation differences between the normal and pathogenic prion protein isoforms." Proceedings of the National Academy of Sciences of the United States of America **96**(23): 13044-13049.

Rudd, P. M., M. R. Wormald, D. R. Wing, S. B. Prusiner and R. A. Dwek (2001). "Prion glycoprotein: Structure, dynamics, and roles for the sugars." Biochemistry **40**(13): 3759-3766.

Sawyer, Elizabeth B., D. Claessen, Sally L. Gras and S. Perrett (2012). "Exploiting amyloid: how and why bacteria use cross-β fibrils." Biochemical Society Transactions **40**(4): 728-734.

Sipe, J. D., M. D. Benson, J. N. Buxbaum, S.-i. Ikeda, G. Merlini, M. J. M. Saraiva and P. Westermark (2014). "Nomenclature 2014: Amyloid fibril proteins and clinical classification of the amyloidosis." Amyloid **21**(4): 221-224.

Sipe, J. D. and A. S. Cohen (2000). "Review: History of the amyloid fibril." Journal of Structural Biology **130**(2): 88-98.

Stopar, D., J. Štrancar, R. B. Spruijt and M. A. Hemminga (2005). "Exploring the local conformational space of a membrane protein by site-directed spin labeling." Journal of Chemical Information and Modeling **45**(6): 1621-1627.

Török, M., S. Milton, R. Kayed, P. Wu, T. McIntire, C. G. Glabe and R. Langen (2002). "Structural and dynamic features of Alzheimer's Aβ peptide in amyloid fibrils studied by site-directed spin labeling." Journal of Biological Chemistry **277**(43): 40810-40815.

Tagliavini, F., F. Prelli, L. Verga, G. Giaccone, R. Sarma, P. Gorevic, B. Ghetti, F. Passerini, E. Ghibaudi and G. Forloni (1993). "Synthetic peptides homologous to prion protein residues 106-147 form amyloid-like fibrils in vitro." Proceedings of the National Academy of Sciences of the United States of America **90**(20): 9678-9682.

Theint, T., P. S. Nadaud, D. Aucoin, J. J. Helmus, S. P. Pondaven, K. Surewicz, W. K. Surewicz and C. P. Jaroniec (2017). "Species-dependent structural polymorphism of Y145Stop prion protein amyloid revealed by solid-state NMR spectroscopy." Nature Communications **8**(1): 753.

Turk, E., D. B. Teplow, L. E. Hood and S. B. Prusiner (1988). "Purification and properties of the cellular and scrapie hamster prion proteins." European Journal of Biochemistry **176**(1): 21-30.

Tycko, R., R. Savtchenko, V. G. Ostapchenko, N. Makarava and I. V. Baskakov (2010). "The α-Helical C-terminal domain of full-length recombinant PrP converts to an in-register parallel β-sheet structure in PrP fibrils: evidence from solid state nuclear magnetic resonance." Biochemistry **49**(44): 9488-9497.

Vanik, D. L., K. A. Surewicz and W. K. Surewicz (2004). "Molecular basis of barriers for interspecies transmissibility of mammalian prions." Molecular Cell **14**(1): 139-145.

Vázquez-Fernández, E., M. R. Vos, P. Afanasyev, L. Cebey, A. M. Sevillano, E. Vidal, I. Rosa, L. Renault, A. Ramos, P. J. Peters, J. J. Fernández, M. van Heel, H. S. Young, J. R. Requena and H. Wille (2016). "The structural architecture of an infectious mammalian prion using electron cryomicroscopy." PLOS Pathogens **12**(9): e1005835.

Walsh, P., K. Simonetti and S. Sharpe (2009). "Core structure of amyloid fibrils formed by residues 106-126 of the human prion protein." Structure (London, England : 1993) **17**(3): 417-426.

Wang, F., X. Wang, C.-G. Yuan and J. Ma (2010). "Generating a prion with bacterially expressed recombinant prion protein." Science **327**(5969): 1132-1135.

Wang, Y. and K. Hall Carol (2018). "Seeding and cross-seeding fibrillation of N-terminal prion protein peptides PrP(120–144)." Protein Science **27**(7): 1304-1313.

Wang, Y., Q. Shao and C. K. Hall (2016). "N-terminal prion protein peptides (PrP(120–144)) form parallel in-register β-sheets via multiple nucleation-dependent pathways." Journal of Biological Chemistry **291**(42): 22093-22105.

Weissmann, C. (2004). "The state of the prion." Nature Reviews Microbiology **2**: 861.

Wopfner, F., G. Weidenhöfer, R. Schneider, A. von Brunn, S. Gilch, T. F. Schwarz, T. Werner and H. M. Schätzl (1999). "Analysis of 27 mammalian and 9 avian PrPs reveals high conservation of flexible regions of the prion protein." Journal of Molecular Biology **289**(5): 1163-1178.

Wuthrich, K. and R. Riek (2001). "Three-dimensional structures of prion proteins." Advances in Protein Chemistry **57**: 55-82.

Xue, W.-F., S. W. Homans and S. E. Radford (2008). "Systematic analysis of nucleation-dependent polymerization reveals new insights into the mechanism of amyloid self-assembly." Proceedings of the National Academy of Sciences of the United States of America **105**(26): 8926-8931.

Yamaguchi, K.-i. and K. Kuwata (2017). "Formation and properties of amyloid fibrils of prion protein." Biophysical Reviews **10**: 517-525.

Yamaguchi, K.-i., T. Matsumoto and K. Kuwata (2008). "Critical region for amyloid fibril formation of mouse prion protein: unusual amyloidogenic properties of the helix 2 peptide." Biochemistry **47**(50): 13242-13251.

Yang, C., W.-L. Lo, Y.-H. Kuo, J. C. Sang, C.-Y. Lee, Y.-W. Chiang and R. P.-Y. Chen (2015). "Revealing structural changes of prion protein during conversion from α-helical monomer to β-oligomers by means of ESR and nanochannel encapsulation." ACS Chemical Biology **10**(2): 493-501.

Appendixes

Chapter 3   Results (I): Sample Preparation

(A) WT
(Theoretical molecular mass: 3705.676 Da)
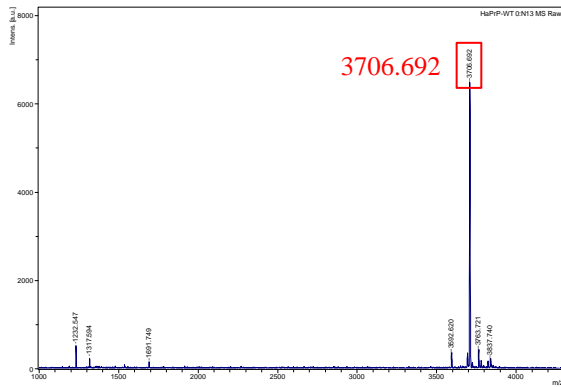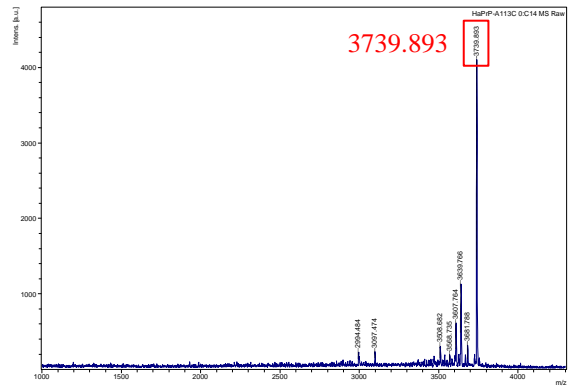
(B) A113C
(Theoretical molecular mass: 3737.648 Da)

(C) A118C
(Theoretical molecular mass: 3737.648 Da)
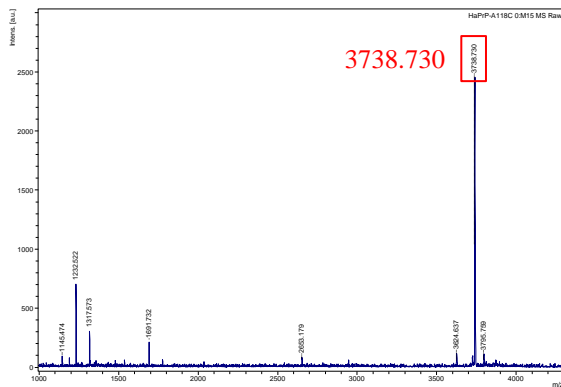
(D) V121C
(Theoretical molecular mass: 3709.616 Da)
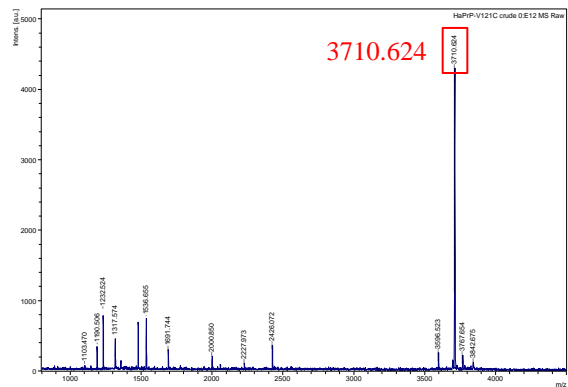
(E) L125C   (Theoretical molecular mass: 3695.601 Da)
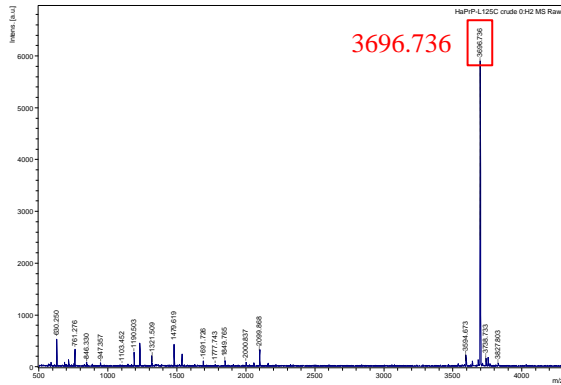
Figure A.1 MS spectra of crude HaPrP peptides obtained by MALDI-TOF/MS.
The actual molecular mass of the peptides were quite matched with their theoretical mass, with 1 Dalton more than the theoretical average mass. The spectra of M129C and M138C crude are shown in Figure 3.2. The sample of M134C crude wasn't sent for MS analysis and thus not available here.

Chapter 4   Results (II): Amyloid Fibril Formation

(A) A113R1

**(B) A113R1**

138
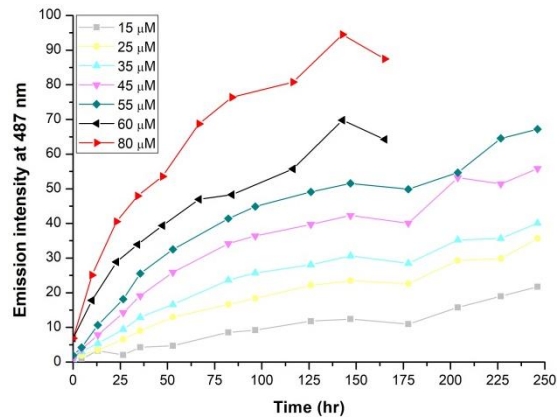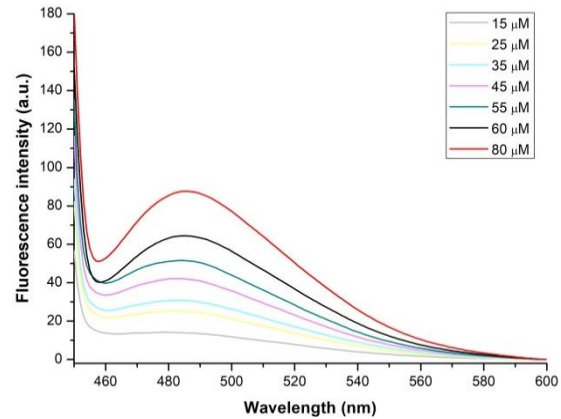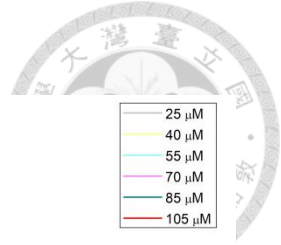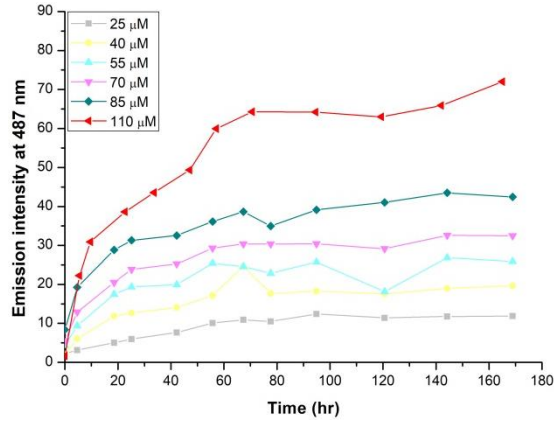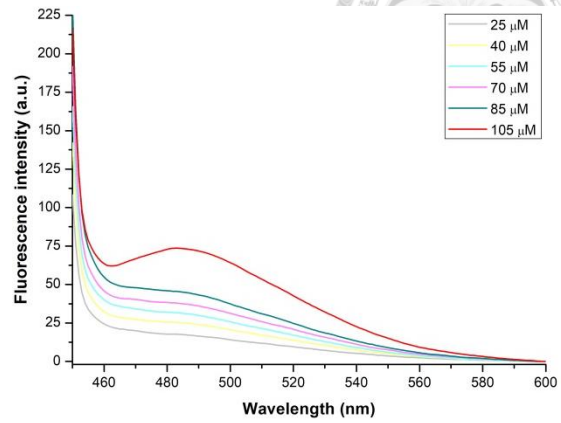
(C) L125R1

(D) L125R1

(E) M129R1
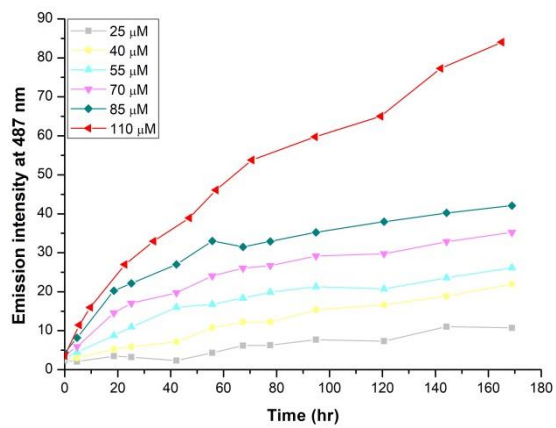
(F) M129R1

(G) M138R1

(H) M138R1

139
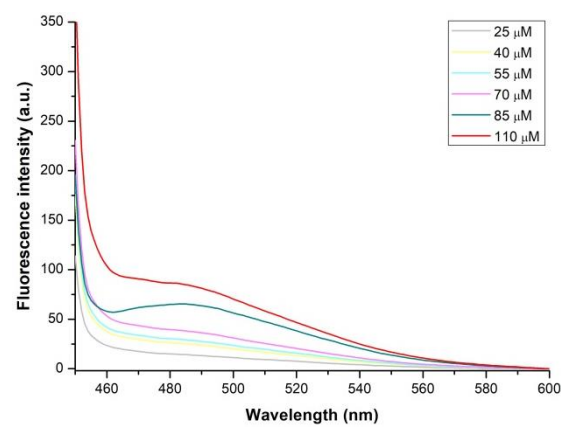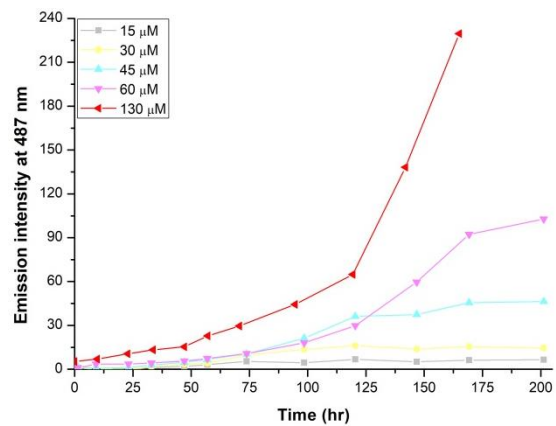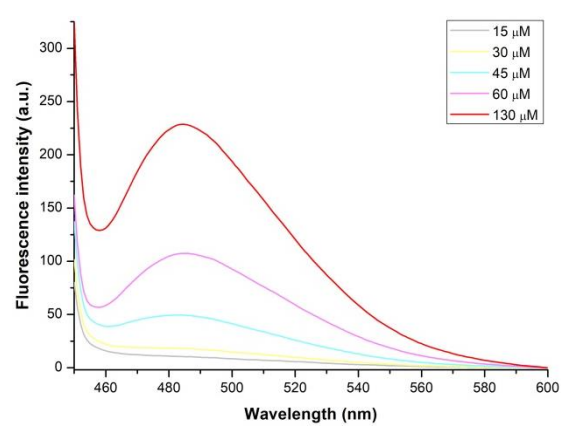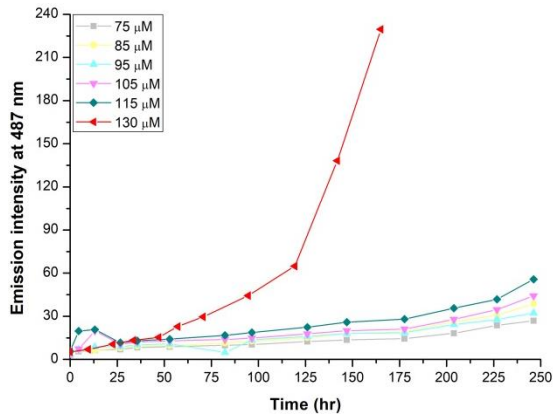
(I) M138R1_2

(J) M138R1_2
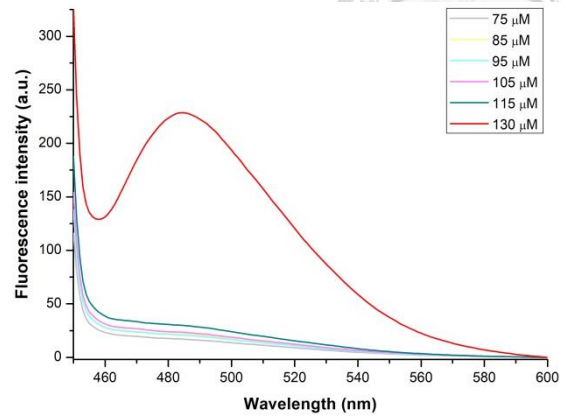
Figure A.2 Higher concentration tests of spontaneous fibril formation of HaPrP(108-144) peptides.

The peptides of **(A)** A113R1, **(C)** L125R1, **(E)** M129R1, **(G)** M138R1, and **(I)** M138R1_2 were tested for the optimal concentration of spontaneous fibril formation, and they were all calibrated by the control of water mixed with fibril formation buffer. The values of emission intensity at 487 nm between different values of concentration of the all samples were drafted together for comparison. The fluorescence spectra obtained from the last data points were drafted together between different concentration as **(B)** A113R1, **(D)** L125R1, **(F)** M129R1, **(H)** M138R1, and **(J)** M138R1_2. The spectra of M138R1 and M138R1_2 were obtained from data measured at different time, with the latter showing values of fluorescence intensity less than the expected. The values of fluorescence intensity at 600 nm were all adjusted to 0. The mutants A118R1, V121R1, and M134R1 were not tested for higher concentration.

(A)

(B)

(C)

(D)

(E)

(F)
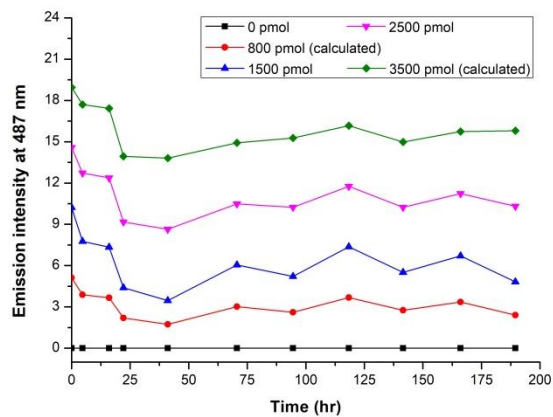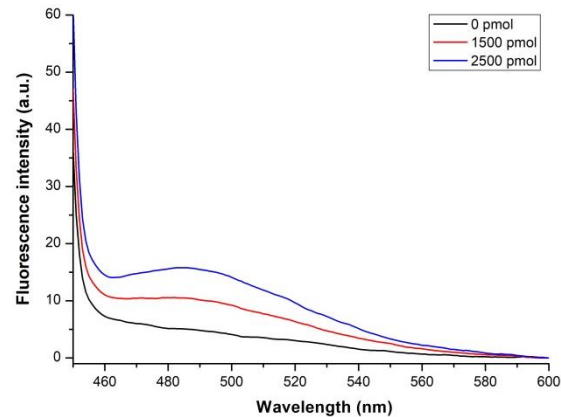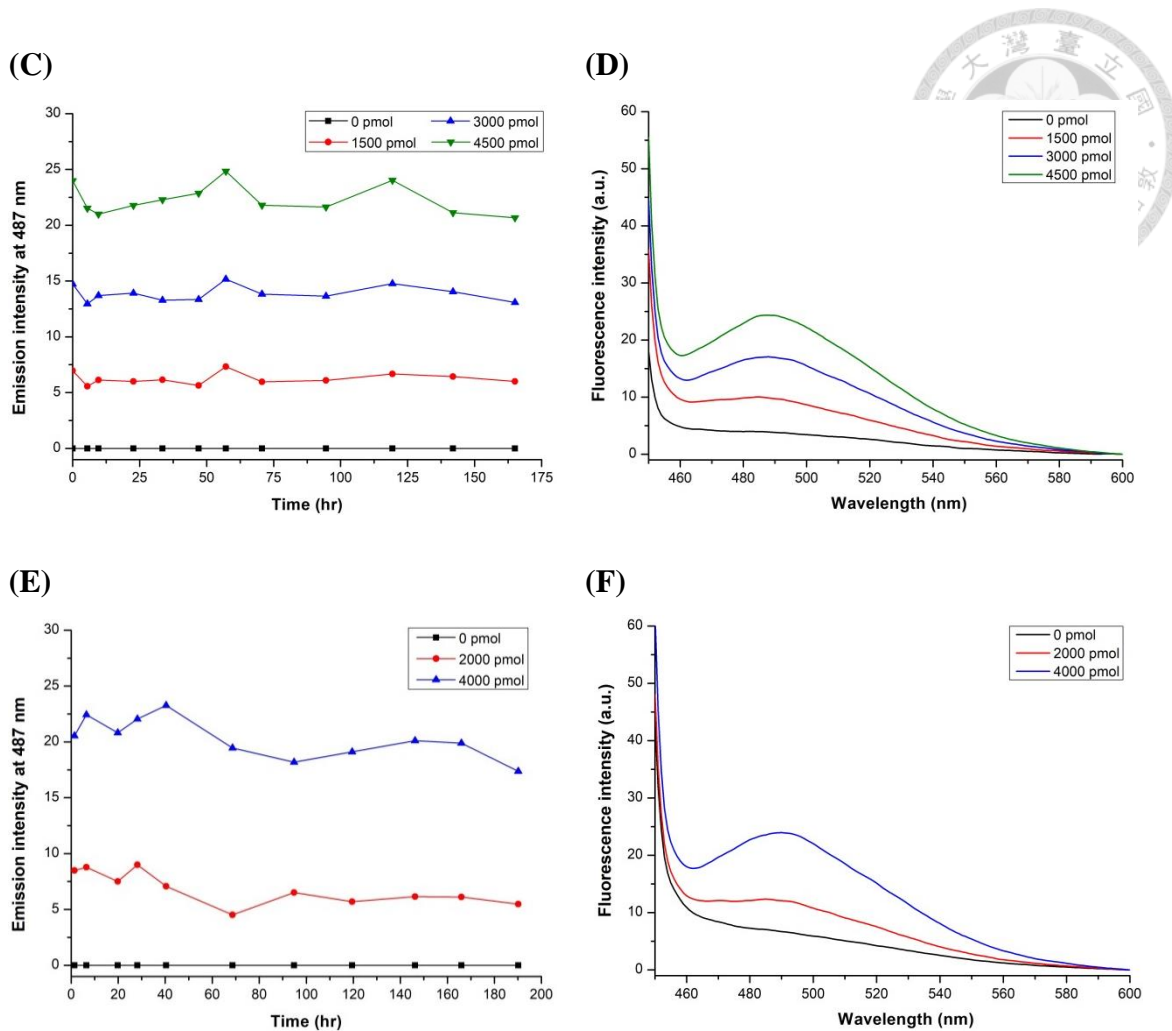
Figure A.3 Tests of values of fluorescence intensity on control and seed solution.

The values of fluorescence intensity on control (ddH$_2$O + FFB) and seed solution were tested before seeded fibril formation based on different amounts of seeds, with the values all calibrated by the control. The values of emission intensity at 487 nm between these two samples were drafted together for comparison as **(A)**, **(C)**, and **(E)**. The fluorescence spectra obtained from the last data point were drafted together between two samples as **(B)**, **(D)**, and **(F)**. The values of fluorescence intensity at 600 nm were all adjusted to 0. Some of the values of intensity from (A) were not measured and were calculated by either interpolation or extrapolation for calibration, and spectra of those items were not available.

141

(A)

(B)
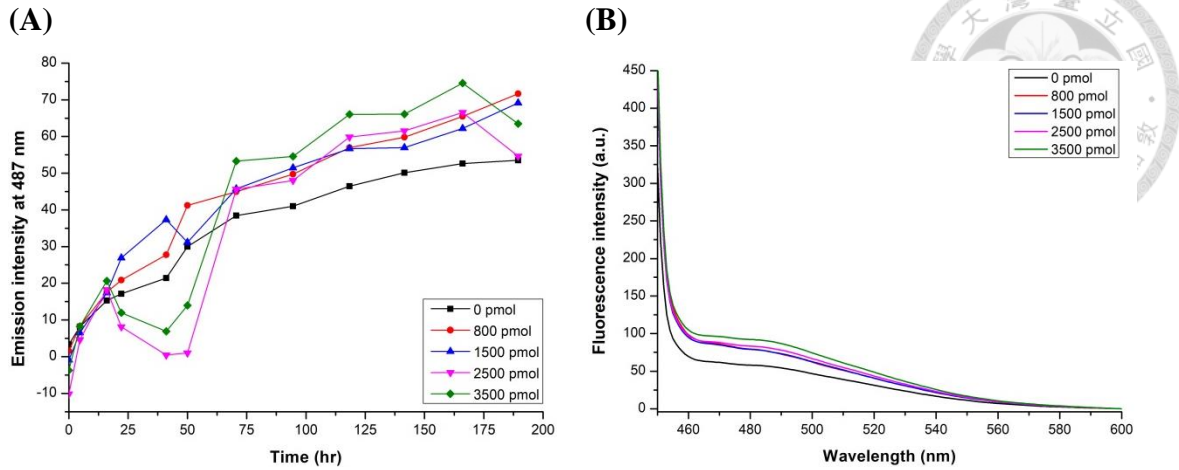
Figure A.4 Seeded fibril formation of HaPrP(108-144)M129R1 peptide.

The seeding assay of M129R1 was tested using various amounts of seeds for fibril formation, and the intensity had been calibrated by the control of either water/FFB or seed solution. The values of emission intensity at 487 nm between were drafted together for comparison as **(A)**. The fluorescence spectra obtained from the last data point were drafted together between different quantities of seeds as **(B)**. The values of fluorescence intensity at 600 nm were all adjusted to 0. The emission spectra were measured from 450 to 600 nm with the excitation at 442 nm, and the slit widths were set to be 5 nm and 10 nm respectively.

Chapter 5   Results (III): TEM & ESR Spectroscopy

(A) WT

**(B) A113R1**

142
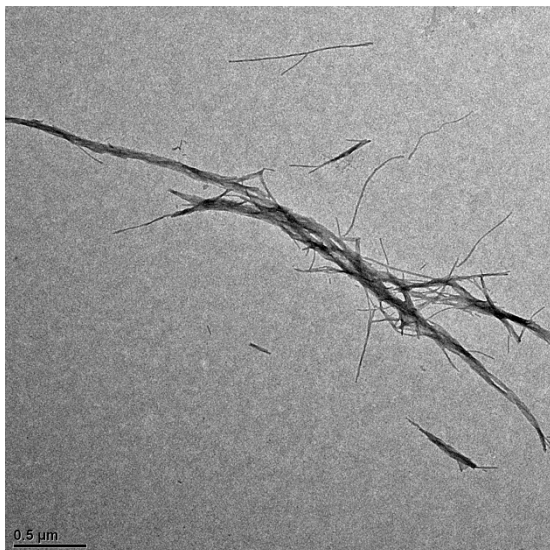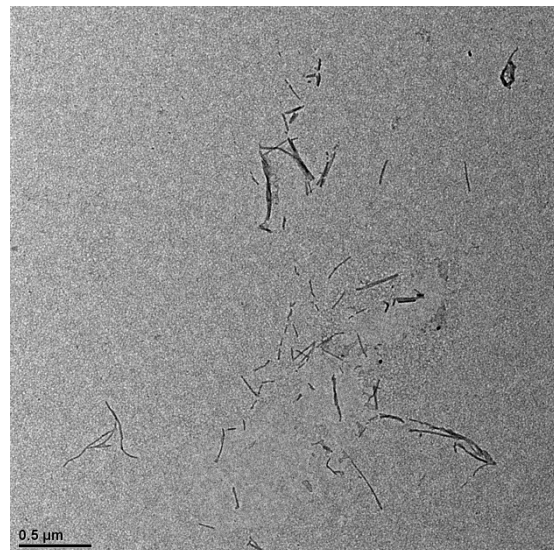
(C) A118R1
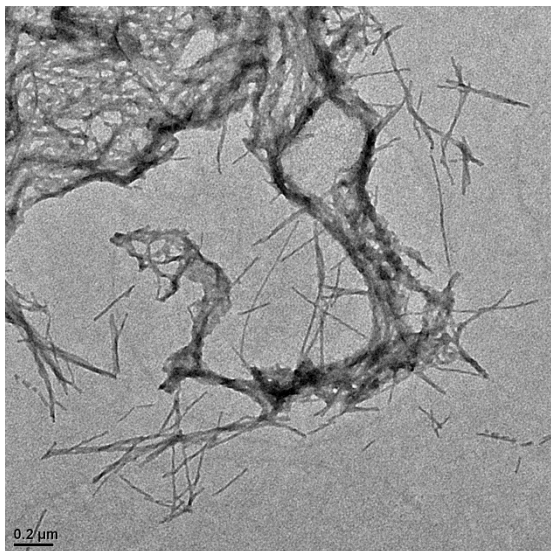
(D) V121R1

**(E) L125R1**

(F) M129R1

143
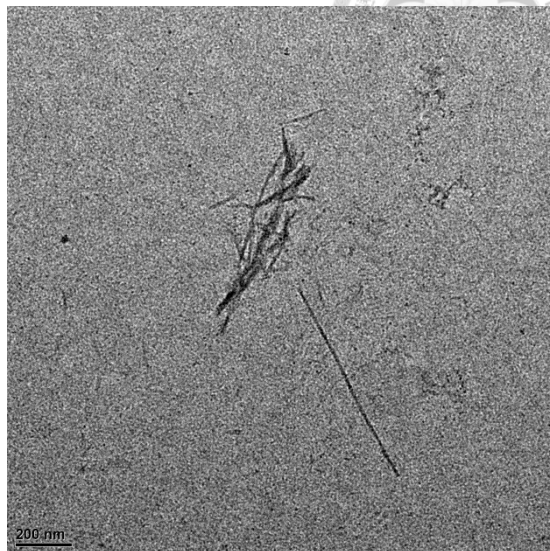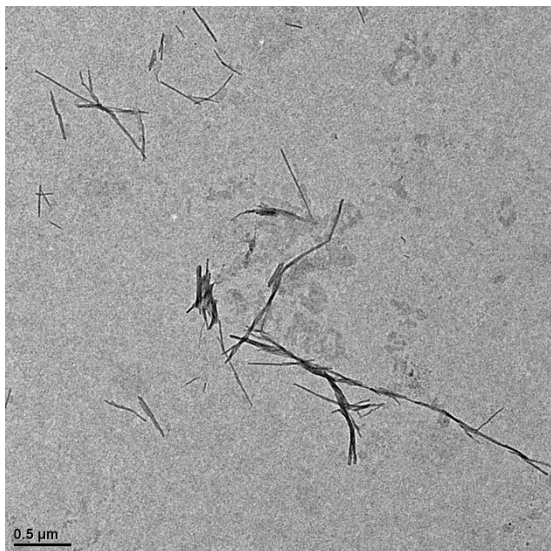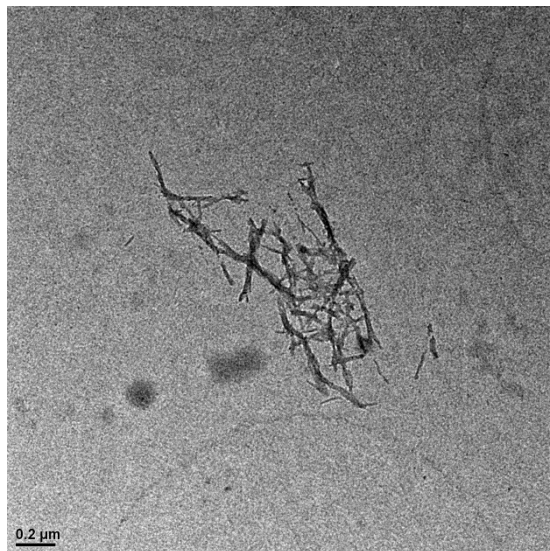
(G) M134R1
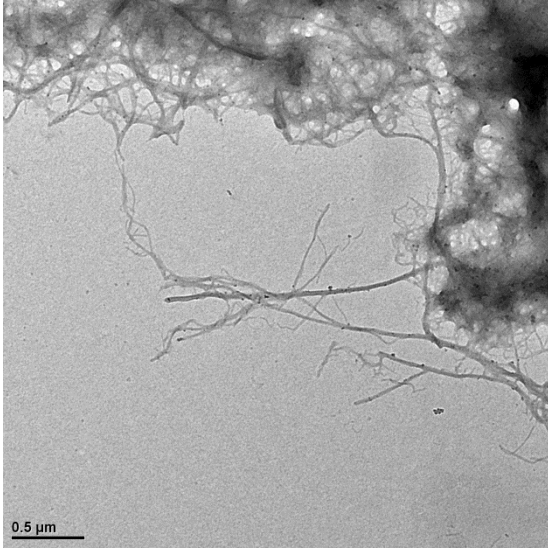
(H) M138R1
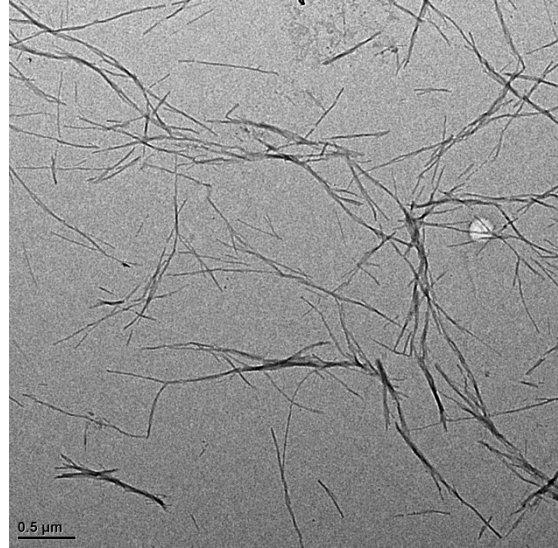
Figure A.5 TEM images of spontaneously formed HaPrP(108-144) amyloid fibrils in larger scales.

All of the samples were incubated at 37℃ quiescently and stored in 4˚C refrigerator after the incubation period ended. The samples were all negatively stained by 2 % (w/v) uranyl acetate. The values of concentration of the samples used for TEM observation are listed below:

WT: 100 μM, A113R1: 80 μM, A118R1: 90 μM, V121R1: 90 μM, L125R1: 105 μM, M129R1: 85 μM, M134R1: 80 μM, M138R1: 60 μM*2

(A) WT seeds

(B) WT seeds

144
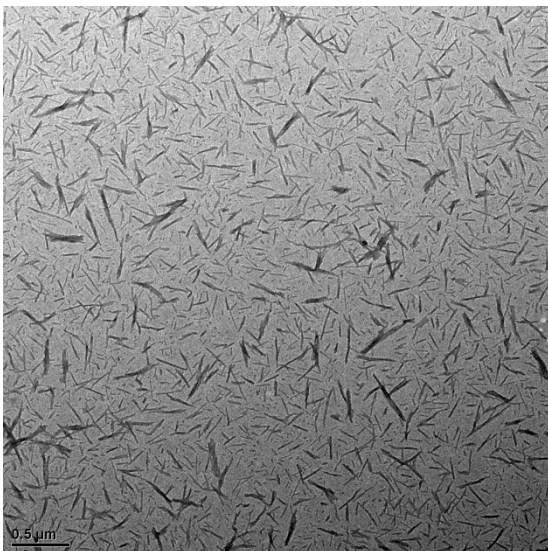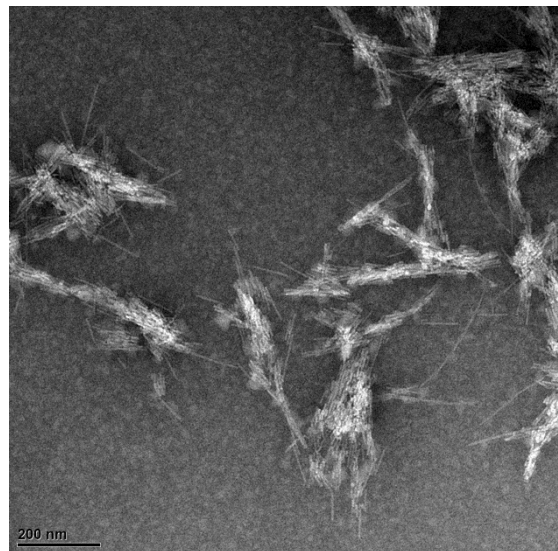
(C) WT
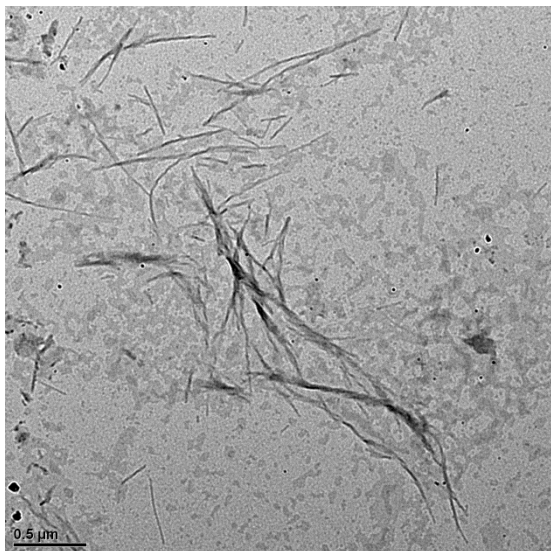
(D) A113R1
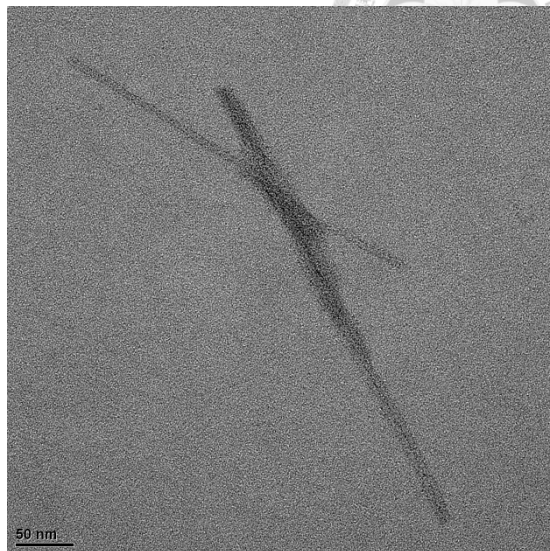
(E) A118R1

(F) V121R1

(G) L125R1

0.5 μm

(H) M129R1

0.2 μm

(I) M134R1

1 μm

(J) M138R1

0.5 μm
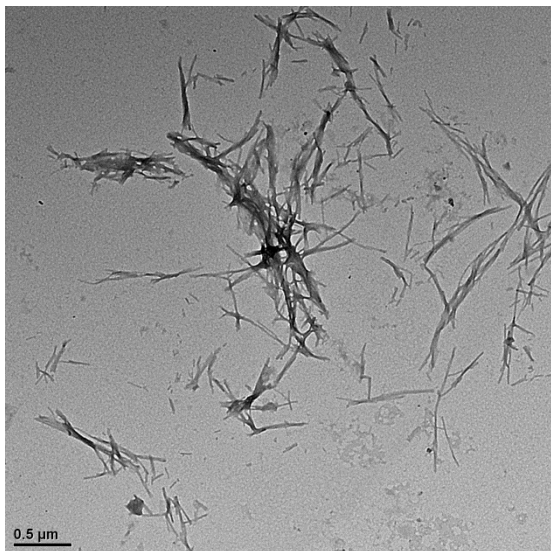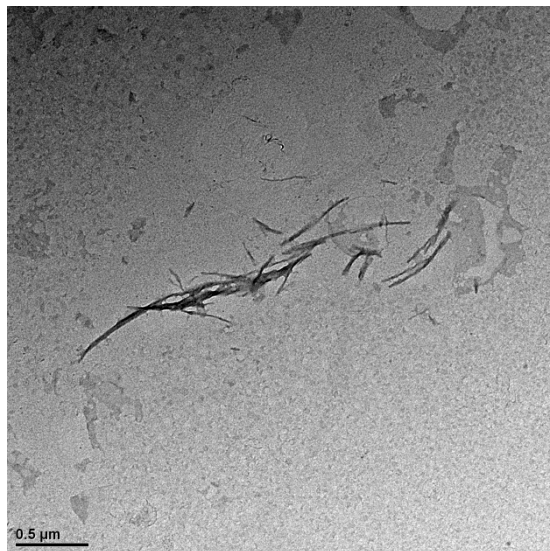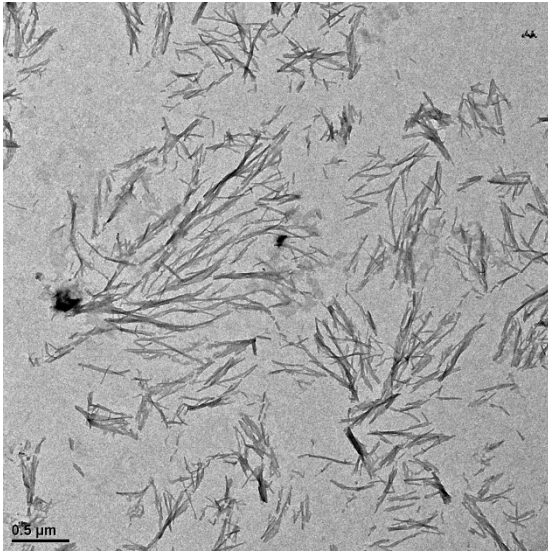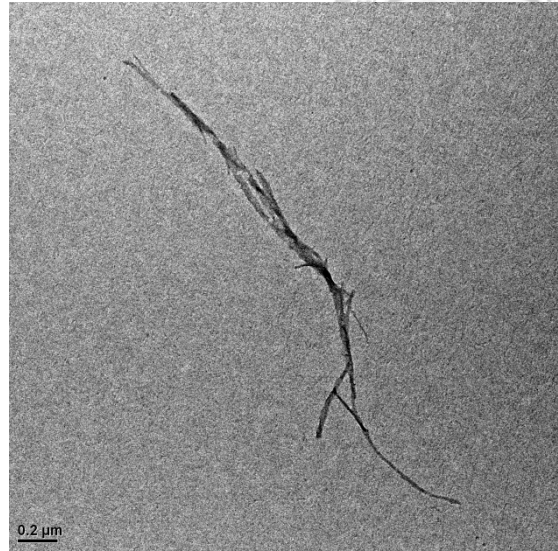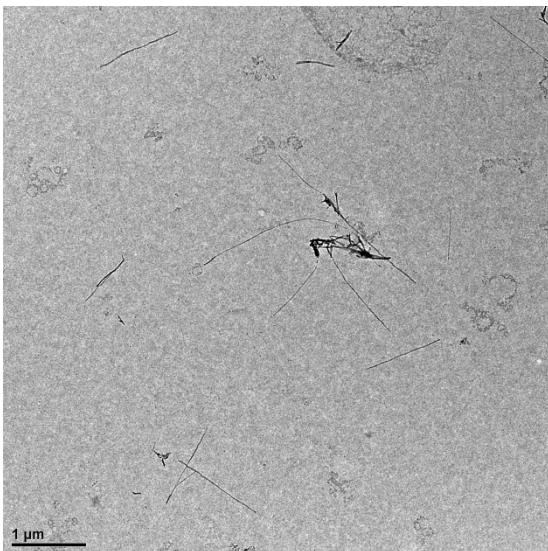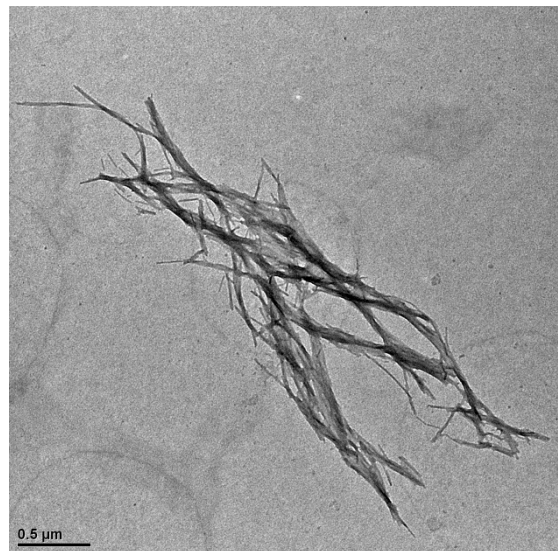
Figure A.6 TEM images of HaPrP(108-144) seeds and amyloid fibrils formed by seeding in different scales.

The samples were all negatively stained by 2 % (w/v) uranyl acetate except for **(B)** WT seeds being stained by 2 % (w/v) phosphotungstic acid. The seeds in **(A)** were freshly prepared while the seeds in **(B)** had been stored in 4°C for weeks. The values of concentration of the samples used for TEM observation are listed below:

WT seeds: 96.4 μM; WT: 10 μM, 20 μL with 5 repeats; A113R1: 15 μM; A118R1: 10 μM, 20 μL with 5 repeats; V121R1: 15 μM, 20 μL with 3 repeats; L125R1: 105 μM; M129R1: 85 μM; M138R1: 130 μM. The fibrils of M134R1 were collected from its ESR sample.

146
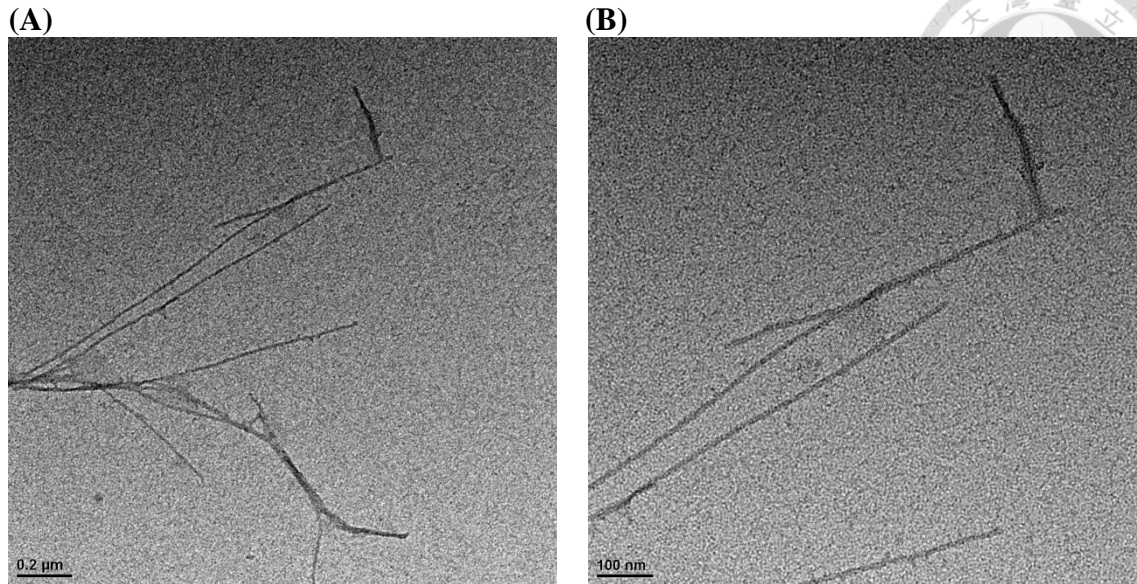
Figure A.7 TEM images of HaPrP(108-144)WT amyloid fibrils formed in buffer of sodium acetate.

The samples were negatively stained by 2 % (w/v) uranyl acetate. The concentration of the two samples was 75 μM.

Chapter 6   Discussion

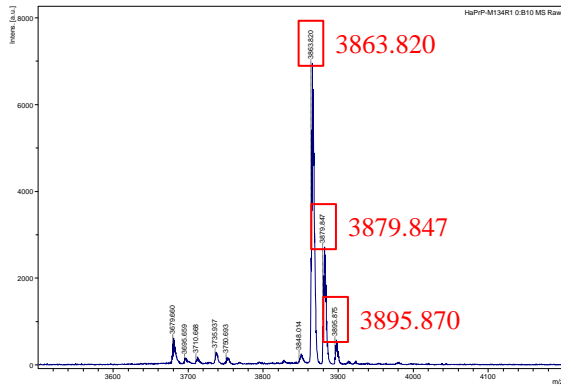**(A) A113C**
(Theoretical molecular mass: 3737.648 Da)
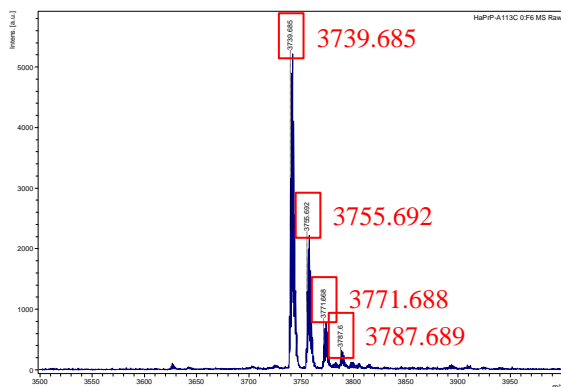
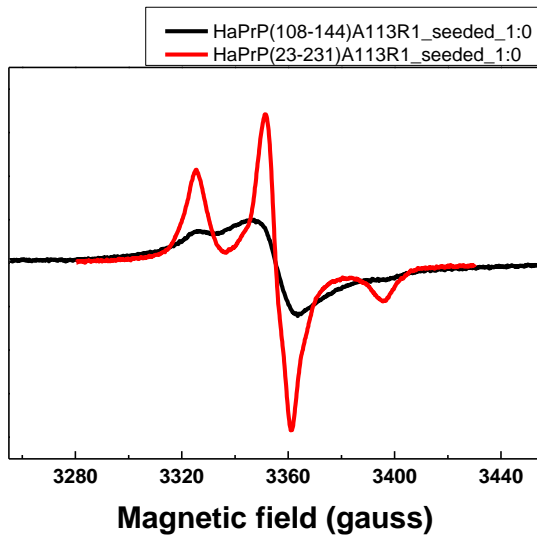**(B) M129R1**
(Theoretical molecular mass: 3861.838 Da)

147
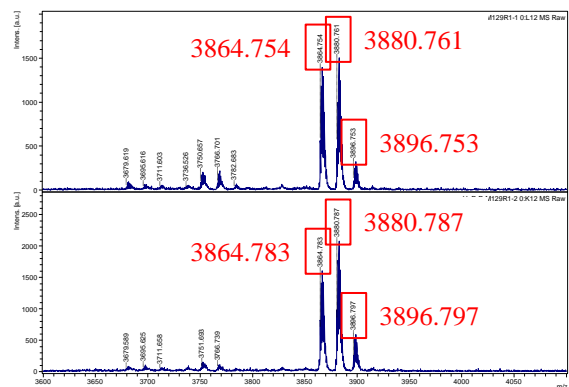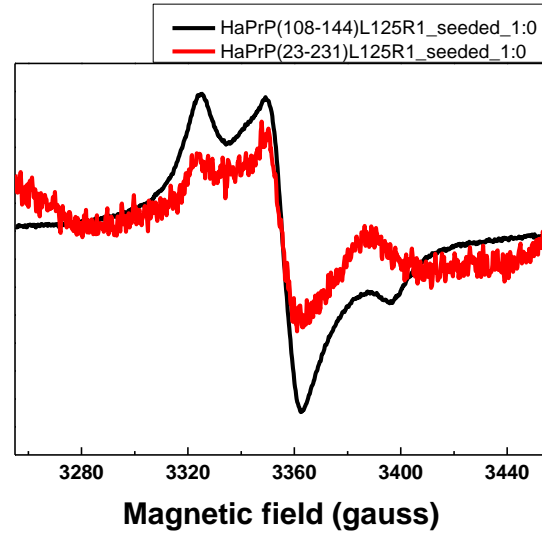
(C) M134R1
(Theoretical molecular mass: 3861.838 Da)

Figure A.8 MS spectra of spin-labeled HaPrP(108-144) mutant peptides showing oxidation.

The actual molecular mass of the peptides were quite matched with their theoretical mass, excepting that there were presence of oxidized peptides showing mass interval of 16 Dalton.
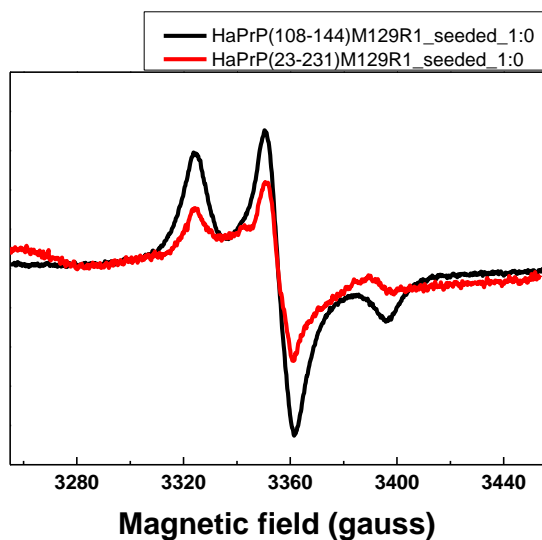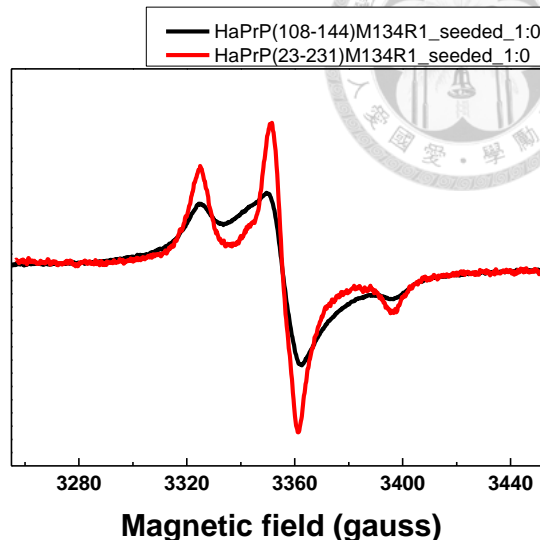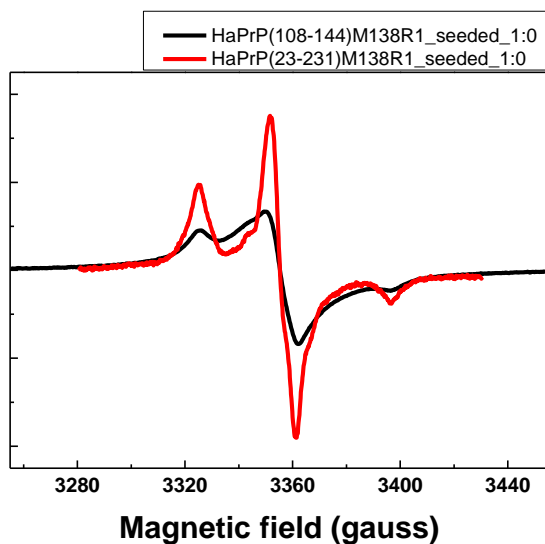
(A) A113R1

(B) L125R1

148

**(C) M129R1**

(D) M134R1

(E) M138R1

Figure A.9 ESR spectrograms of HaPrP(108-144) peptides and HaPrP full-length proteins by seeding assay.

Spectrograms at each single mutant site were superimposed and compared between seeded peptides and full-length protein. X-band continuous wave (cw)-ESR was measured at an operating frequency of ~9.42 GHz at the temperature of 200K. The sweep width of the measurement was 200 G, ranging from 3250 to 3450 Gauss. The data of HaPrP full-length protein and the spectrograms shown here were completed and graphed by Dr. Yung-Han Chen in our lab. Spectrograms of mutant A118R1 and V121R1 by seeding from full-length protein are not available yet.
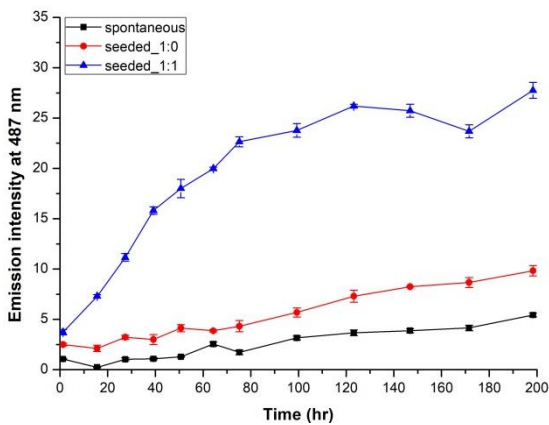
(A) A113R1_15 μM
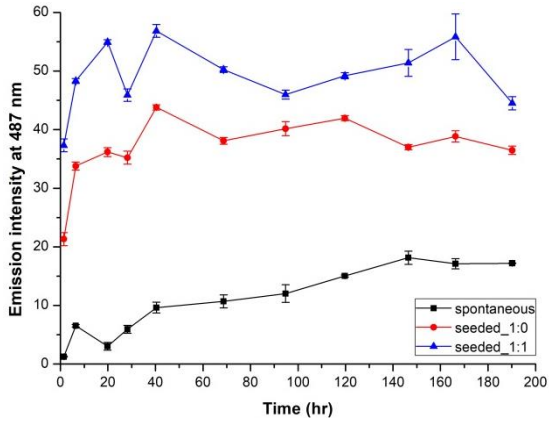
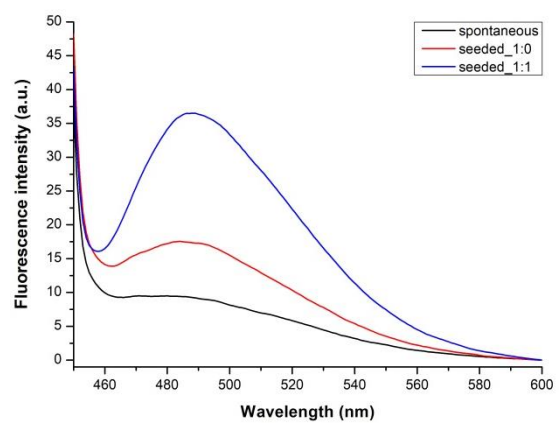**(B) A113R1_15 μM**
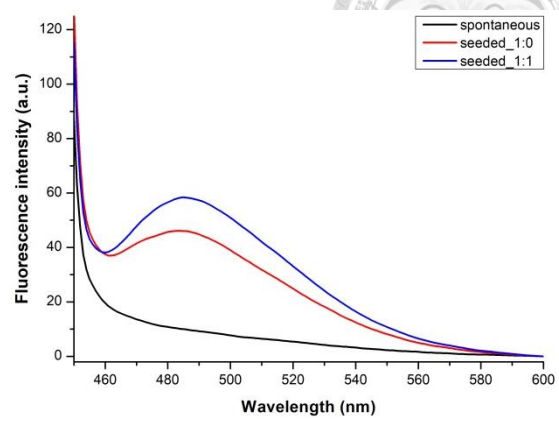
(C) M134R1_10 μM

(D) M134R1_10 μM

Figure A.10 Seeded fibril formation of HaPrP(108-144) A113R1 and M134R1 mutants including spontaneously formed, 1:0 (undiluted) and 1:1 spin-diluted fibrils.

The mutants of A113R1 and M134R1 were tested with for different dilution factor of seeded fibril formation, and the intensity had all been calibrated by the control of either water/FFB or seed solution. The values of emission intensity at 487 nm between were drafted together for comparison as **(A)** A113R1 and **(C)** M134R1. The fluorescence spectra obtained from the last data point were drafted together between different samples as **(B)** and **(D)**. The values of fluorescence intensity at 600 nm were all adjusted to 0. The emission spectra were measured from 450 to 600 nm with the excitation at 442 nm, and the slit widths were set to be 5 nm and 10 nm respectively.

150
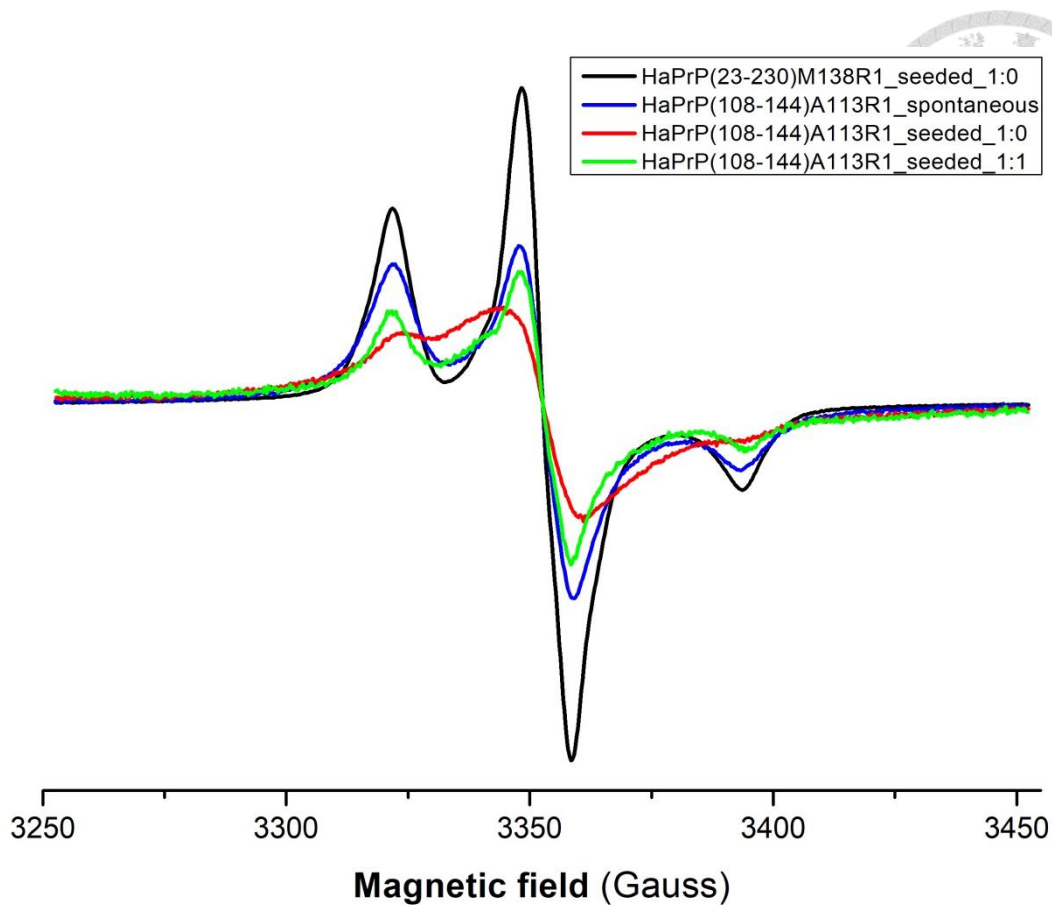
Figure A.11 ESR spectrograms of HaPrP(108-144)A113R1 from spontaneously formed, 1:0 (undiluted) and 1:1 spin-diluted fibrils.

X-band continuous wave (cw)-ESR was measured at an operating frequency of ~9.42 GHz at the temperature of 200K. The sweep width of the measurement was 200 G, ranging from 3250 to 3450 Gauss.

151